InAs Quantum Wires Grown on Vicinal Substrates

Growth, Characterization and Simulation of InAs Quantum Wires on Vicinal Substrates

By
Andrew Scullion, B. Sc.

A Thesis Submitted to
the Department of Materials Science and Engineering
in Partial Fulfillment of the Requirements
for the Degree Master of Materials Science

McMaster University MASTER OF SCIENCE (2013) Hamilton, Ontario

(Department of Materials Science and Engineering)

TITLE: Growth, Characterization and Simulation of InAs Quantum Wires on Vicinal Substrates

AUTHOR: Andrew Scullion, B. Sc. (Carleton University)

SUPERVISORS: Gianluigi A. Botton and David A. Thompson

PAGES: xii, 119

Abstract

The heteroepitaxial growth of InAs self-assembled quantum wires on vicinal substrates is investigated. InGaAlAs lattice-matched to InP was first deposited onto an InP(001) substrate with and without a 0.9° off-cut toward the (110) direction, followed by the deposition of a strained layer of InAs. Dense InAs quantum wires were successfully grown on both nominally flat and vicinal substrates in order to observe the effect of the presence of atomic steps. The off-cut angle was chosen based on the wire spacing on a flat substrate to serve as a template for their nucleation and improve their size distribution for use as 1.55 μm wavelength lasers required by the telecommunications industry. The results have shown a modest but statistically significant improvement in the width of their size distribution. In addition, a kinetic Monte Carlo simulation including full strain calculations was developed to further understand the nucleation process. The model developed here disproves the idea that InAs quantum wires are aligned towards the $(\bar{1}10)$ direction due to diffusion anisotropy. The simulation of the formation of quantum wires similar to those observed experimentally has been achieved and the Stranski-Krastanow growth mode is demonstrated.

Acknowledgments

I would like to firstly thank my supervisors, Gianluigi Botton and David Thompson for their support, encouragement and guidance throughout my Master's Degree, and Jeff Hoyt for accepting to take part in my committee.

I would also like to thank Fred Pearson, Andreas Korinek and Matthieu Bugnet for microscopy training, Travis Casagrande for microscopy assistance, Shahrzad Hosseini, Wenhe Gong, Julia Huang and Andy Duft for help with sample preparation, Sherri Hadian and Shahram Tavakoli for helpful discussions, David Rossouw for exchanging interesting ideas and of course all my colleagues for their support.

Contents

List of Figures

List of Tables

List of Abbreviations

ADF	**A**nnular **D**ark **F**ield
AFM	**A**tomic **F**orce **M**icroscopy
CTEM	**C**onventional **T**ransmission **E**lectron **M**icroscopy
CVD	**C**hemical **V**apor **D**eposition
DF	**D**ark **F**ield
DFT	**D**ensity **F**unctional **T**heory
ECS	**E**quilibrium **C**rystal **S**hape
EELS	**E**lectron **E**nergy **L**oss **S**pectroscopy
FCC	**F**ace-**C**entered **C**ubic
FFT	**F**ast **F**ourier **T**ransform
HAADF	**H**igh **A**ngle **A**nnular **D**ark **F**ield
HRSTEM	**H**igh **R**esolution **S**canning **T**ransmission **E**lectron **M**icroscopy
HRTEM	**H**igh **R**esolution **T**ransmission **E**lectron **M**icroscopy
kMC	**k**inetic **M**onte **C**arlo
MBE	**M**olecular **B**eam **E**pitaxy
MD	**M**olecular **D**ynamics
MOCVD	**M**etal**o**rganic **C**hemical **V**apor **D**eposition
PBC	**P**eriodic **B**oundary **C**onditions
PCA	**P**rincipal **C**omponent **A**nalysis
RHEED	**R**eflection **H**igh **E**nergy **E**lectron **D**iffraction
SK	**S**transki-**K**rastanow

SOS	**S**olid **o**n **S**olid
STEM	**S**canning **T**ransmission **E**lectron **M**icroscopy
STM	**S**canning **T**unneling **M**icroscopy
TEM	**T**ransmission **E**lectron **M**icroscopy
TMP	**T**urbo **M**olecular **P**ump
UHV	**U**ltra **H**igh **V**acuum

Chapter 1

Introduction

1.1 Overview

The electronic band gap is typically an intrinsic property of a semiconductor which separates two continuous bands of allowable electron energy states called the valence band and the conduction band. This separation allows for the functioning of devices such as transistors, solar cells, diodes and lasers. It is important however to be able to modify the properties of semiconductors for different applications. The use of III-V semiconductors allows us to control the lattice constant and band gap by producing alloys with varied proportions of group III elements such as Al, Ga and In, and group V elements such as P, As and Sb. However, this has only a relatively small effect on the density of states outside the band gap.

Quantum well structures provide more control over the band gap which is useful for controlling the absorption spectrum of solar cells and the emission wavelength of diodes and solid state lasers. Additionally, quantum confinement provides us with the ability to modify the density of states of devices in a favorable way. 2-dimensional quantum wells[1] are now fairly easy to produce through the sequential deposition of lattice-matched semiconductor layers using standard chemical or

[1]The convention used here is as follows: 2D (layers or wells), 1D (wires) and 0D (dots) quantum potential wells provide confinement in 1, 2 and 3 dimensions.

physical deposition techniques. Although even with atomically sharp interfaces the quality of lasers made using such structures is limited by the stepwise density of states due to the quantum confinement in only one dimension. This problem can be resolved by fabricating structures with confinement in more dimensions such as quantum wires and quantum dots.

The desirable size of these structures is on the order of 10 nm and, due to the limitations of electron beam lithography in terms of spatial resolution as well as scalability, the production of structures through self-assembly is a promising method but needs to be better understood for its reliable use in industry. In the case of semiconductor epitaxy, self-assembled structures can be produced via a strain relief mechanism known as the Stranski-Kranstanow growth mode whereby 3-dimensional islands form during the deposition of a material on a lattice-mismatched substrate. Given that the bandgap of the deposited layer is smaller than (and within) that of the substrate, isotropic islands form quantum dots and elongated islands form quantum wires as they provide quantum confinement.

Due to a combination of bandgaps and lattice mismatch, the InAs/InP system is well suited to the production of quantum wire or quantum dot lasers with a wavelength around 1.55 μm which is important for fiber optic telecommunication. This wavelength corresponds to a minimum in the absorption spectrum of SiO_2[1]. Although these quantum structures can be grown fairly reliably, the linewidth of the lasers they produce is greatly limited by their uneven size distribution or heterogeneity. In the case of quantum wires, even though each individual wire may produce a narrow spectrum, the spectrum produced by all the wires together may be broad if they all have different sizes. The spectrum is essentially convolved by their size distribution.

It has been shown in some studies that the size distribution of quantum wires can be improved by growing them on vicinal substrates but others show no improvement. Furthermore, the off-cut angle of the substrates in these studies is somewhat arbitrary. In this work, the effect of growing InAs quantum wires on vicinal substrates is investigated. InP(001) substrates with an off-cut angle of 0.9° toward the (110) direction covered by a lattice-matched InGaAlAs alloy for quantum confinement were used. The angle of the off-cut was chosen to match the

spacing of InAs quantum wires grown on nominally flat substrates with the intention of assisting their nucleation. The effect of the off-cut, the growth temperature and the Al content of the confinement layer was investigated. Furthermore, a kinetic Monte Carlo model of adatom diffusion including full strain calculations was developed in order to gain further insight into the nature of self-assembled heterostructures.

1.2 Fundamentals of Quantum Structures

Heterostructures are geometrical arrangements of different semiconductor materials. Those in which a small bandgap material is surrounded by a larger bandgap material are quantum heterostructures sometimes referred to as quantum wells[2]. Low energy electrons within the conduction band of these wells are trapped and their spatial confinement allows them to only occupy particular energy levels above the conduction band edge. This phenomenon is described by the solution of Schrödinger's time independent equation (1.1) [2]. In this equation, $\hbar$ is the reduced Planck constant, m_e^* is the effective mass of the electron, ∇^2 is the Laplace operator, ψ is the time independent wavefunction, V is the potential energy the electron is subjected to and E is its total energy.

$$-\frac{\hbar^2}{2m_e^*}\nabla^2\psi + V\psi = E\psi \tag{1.1}$$

For a one-dimensional infinite potential well of width a as defined in equation (1.2), the allowable energy states are given by expression (1.3) for positive integer values of n and for a three-dimensional well the energy levels are given by equation (1.4). V_c represents the energy of the conduction band edge.

[2]The term *quantum well* can be a bit ambiguous since any quantum structure has a potential well although the term is typically used to indicate a 2D quantum layer or film.

$$V(x) = \begin{cases} V_c & 0 < x < a \\ \infty & \text{otherwise} \end{cases} \tag{1.2}$$

$$E_n = V_c + \frac{\hbar^2 n^2 \pi^2}{2m_e^* a^2} \tag{1.3}$$

$$E_{n_x,n_y,n_z} = V_c + \frac{\hbar^2 \pi^2}{2m_e^*}\left(\frac{n_x^2}{a_x^2} + \frac{n_y^2}{a_y^2} + \frac{n_z^2}{a_z^2}\right) \tag{1.4}$$

If the well is small in all three dimensions as in the case of a quantum dot, that is, a_x, a_y and a_z are small, the density of states consists of very sharp peaks. If one of these dimensions is large, let's say a_x for a quantum wire along the x-direction, then the spacing between energy levels for different values of n_x is small and the density of states is approximately continuous. This one-dimensional structure will have a density of states with peaks which follow $E^{-1/2}$. If two of the dimensions are large, the density will have a staircase shape and finally for a bulk material the density of states is proportional to $E^{1/2}$. These functions are illustrated in figure 1.1.

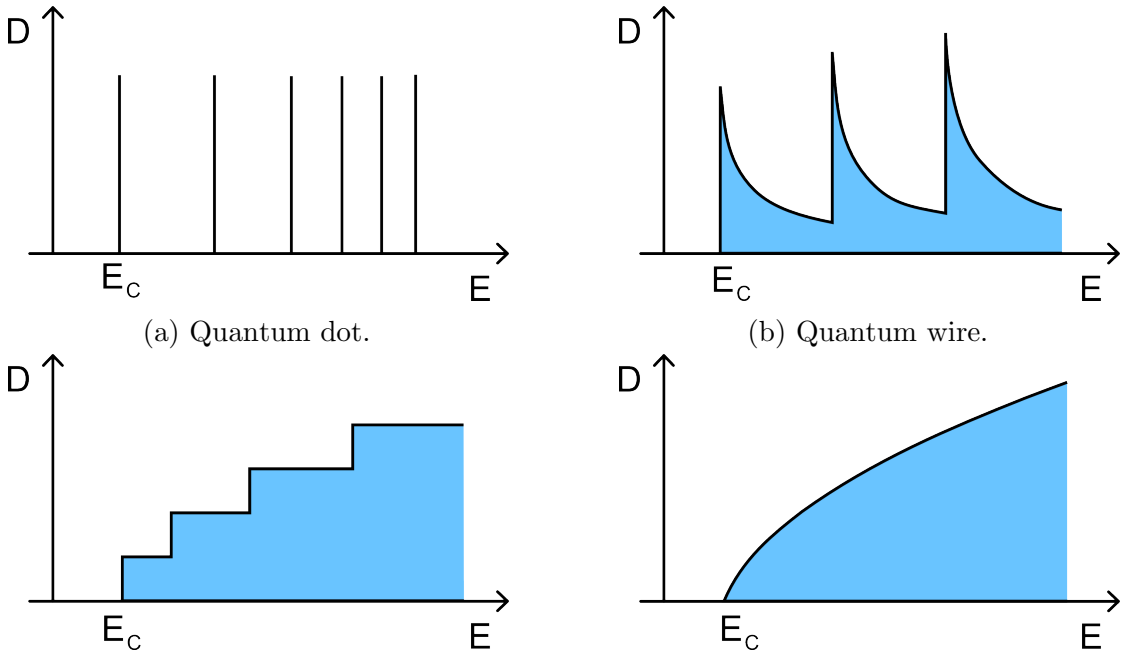

(a) Quantum dot.

(b) Quantum wire.

(c) Quantum well.

(d) Bulk.

Figure 1.1: Density of states for confinement in different dimensions.

The density of states in the valence band is similar but inverted[3] and scaled vertically due to a different electron effective mass. Because the spectral linewidth of a light emitting device such as a solid state laser is directly dependent on the convolution of the density of states of the conduction and valence band, under ideal conditions quantum dots are the most desirable structure. However this is only the case if it is possible to produce dots of uniform size, that is, with a narrow size distribution. This has proven to be a difficult task using self-assembled growth techniques [3]. Although quantum wires provide less quantum confinement and therefore a broader density of states, the ability to control their size distribution seems more accessible using vicinal substrates [4] and for this reason they are the topic of interest for this thesis. Furthermore, despite a modest improvement of the density of states of quantum wires over a quantum well compared to that of quantum dots, laser devices using wires have shown an improvement in their threshold current density and the insensitivity of their output wavelength to temperature [5].

1.3 Fundamentals of Molecular Beam Epitaxy

Epitaxy refers to the deposition of an ordered material layer onto a substrate. In the field of semiconductors, there exist many different methods of depositing thin films of material such as metalorganic chemical vapor deposition (MOCVD), sputtering and molecular beam epitaxy (MBE) which each have their own advantages and drawbacks. Chemical vapor deposition consists of exposing a heated substrate to a reactive gas which decomposes into another gas and the atom being deposited. For example, a metalorganic compound such as trimethylgallium ($(CH_3)_3Ga$) can be "cracked" on the substrate to deposit Ga while releasing methane gas (CH_4) and a compound such as arsine (AsH_3) can react to deposit As while releasing H_2. This technique is well suited to commercial applications since it allows simultaneous deposition on many substrates by filling a vacuum chamber with such gases. Sputtering is a physical vapor deposition (PVD) technique which relies on producing a plasma above a target material such as metallic gallium, causing ions

[3]The density of states is roughly flipped about middle of the band gap so that it increases with lower energy for a bulk material.

to bombard its surface and eject Ga atoms. This target is aligned geometrically with the substrate where the Ga atoms are deposited. The chamber in which this takes place can be filled with a gas such as N_2 in order to form GaN for example. Unlike CVD, this method requires a line of sight between the substrate and the source but can be a more economical way of performing thin film deposition.

MBE is a deposition technique where the elements of interest are deposited using quite literally a molecular or atomic beam. For the deposition of metals (Al, Ga, In, etc.), the substrate is exposed to a (typically molten) metallic source heated inside a crucible called an effusion cell as illustrated in figure 1.2. The metal evaporates and the escaping vapor travels straight towards the substrate and condenses onto it as indicated by the rightmost arrow. Group V species (P, As, Sb) are deposited in the form of a molecular beam by cracking a gas such as arsine (AsH_3) in a cracker cell which is also in line with the substrate as indicated by the other arrow. Unlike vapor at normal pressure which travels through convection, the pressure inside an MBE chamber is such that it undergoes molecular flow.

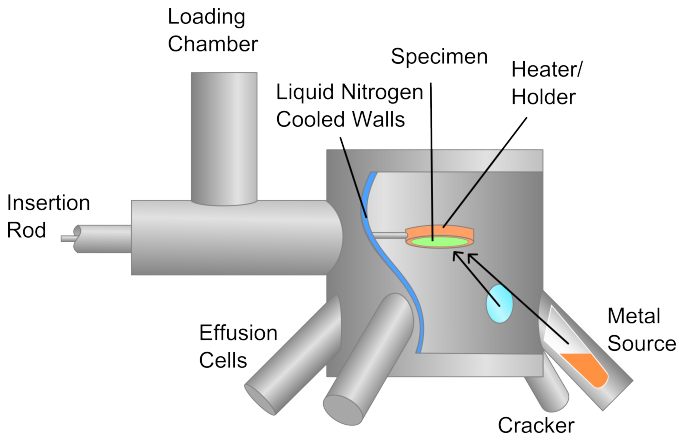

Figure 1.2: An MBE chamber.

We can easily estimate the vacuum required for molecular flow which occurs when the mean free free path of evaporating atoms is greater than the distance between their source and the substrate. Assuming that gas atoms act as hard spheres with a radius equal to the Bohr radius a_0, their cross section[4] is given by $\sigma = \pi(2a_0)^2$. For there to be less than one collision over distance of $L = 1$ m, the pressure needs to be less than roughly 0.1 Pa as demonstrated in equation (1.7)

[4]The radius used for σ is $2a_0$ because this is the maximum distance between two atoms for there to be a collision.

using the ideal gas law.

$$PV = Nk_BT \tag{1.5}$$

$$P = \frac{Nk_BT}{V} = \frac{Nk_BT}{\sigma L} \tag{1.6}$$

$$= \frac{1 \text{ atom} \cdot 1.38 \cdot 10^{-23} \cdot 300}{3.5 \cdot 10^{-20} \cdot 1} \approx 0.1\text{Pa} \tag{1.7}$$

Although a particularly high vacuum is not required for the operation of MBE, an ultra-high vacuum (UHV $\sim 10^{-9}$ Pa) is used in order to provide excellent thin film purity by removing any unwanted contaminants because the properties of semiconductors is extremely sensitive to small concentrations of impurities. On top of this, the walls of the chamber are cooled with liquid nitorgen to help collect any contaminants through condensation. The other important components of an MBE chamber are the loading chamber, the insertion rod, the vacuum system and the specimen holder. The loading chamber is where the substrate is inserted into the apparatus. It is separated from the main chamber by a valve and is pumped down to high vacuum before the sample is placed in the main MBE chamber in order to greatly reduce contamination. The insertion rod is in a closed system and is displaced magnetically outside by the operator. The vacuum system consists of a turbo molecular pump (TMP) backed by a roughing pump in addition to the cooled chamber walls which greatly improve the vacuum at very low pressures. The sample holder heats the substrate to the desired temperature and a pyrometer in conjunction with a thermocouple behind the sample are used in order to measure and monitor the temperature during growth.

The important advantages of MBE over other thin film deposition methods is that it provides excellent control over the amount of material deposited and produces very pure thin films which is excellent for research. The deposition rate of group V elements is directly controlled by the flow rate of the hydride gas such as arsine[5] and the deposition rate of metals is determined by their partial pressure inside their respective effusion cells which increases with temperature. Unlike in CVD where a gas can take some time to fill and evacuate the deposition chamber, using MBE, the beam can be blocked and unblocked by a shutter to quickly stop

[5]The flow must of course be calibrated for the geometry of the chamber.

and start the deposition process. This allows for sub-monolayer control over the amount of deposited material. Although MBE is (currently) difficult to scale up for commercial purposes, it was chosen for the scientific investigations in this thesis due to its great precision.

The growth of III-V semiconductors is performed under conditions where the equilibrium phase is a mixture of the desired stoichiometric compound (such as GaAs) and a gaseous form of the group V element[6] [6]. This means that the deposition rate of the group V element is greater than that of the group III element and any excess of the former beyond the amount required to produce the stoichiometric compound simply evaporates. This is referred to as the group V overpressure and a value of interest is the V/III ratio which must be maintained above 1 under normal growth conditions. Otherwise, a lower ratio leads to the formation of metallic beads which is usually undesirable.

Additionally, the surface reconstruction, that is the arrangement of atoms on the substrate surface during growth using MBE, depends on the V/III ratio as well as other growth conditions such as temperature and the nature of the III-V compound. Under the conditions used in this work, the expected surface reconstruction on a (001) surface is the (2×4) structure based on the surface phase diagram in [7] or more precisely the $\beta 2$ (2×4) based on Moll's work [8, 9]. This has an influence on the surface energy of different crystal facets and plays an important role in the model developed in chapter 3.

1.4 Transmission Electron Microscopy

When dealing with structures as small as quantum wires or nearly any thin film, precision devices such as the transmission electron microscope (TEM) are required for any structural characterization. The two principal imaging modes used here to characterize cross-sectional samples are dark field (DF) imaging which can provide good composition contrast and annular dark field (ADF) high resolution scanning

[6] However, one can argue that MBE growth is not performed under thermodynamic equilibrium

transmission electron microscopy (HRSTEM) which provides atomically resolved micrographs[7] also with compositional contrast. These are the primary methods used since the most important distinguishing feature of the wires with respect to the surrounding material is their composition and composition distribution. Features such as dislocations or changes in crystal structure are simply not present and contrast in atomically resolved spectral images using electron energy loss spectroscopy (EELS) is difficult to obtain for III-V semiconductors because of the broad shape of the core-loss peaks of their constituents.

A dark field image is obtained in conventional TEM (CTEM) by placing an aperture in the objective plane of the microscope just below the sample where its diffraction pattern is first produced as illustrated in figure 1.3. The image on the fluorescent screen or the CCD camera is then only formed by the electrons diffracted in the chosen direction corresponding to the diffraction spot selected using the aperture. This allows the observation of various contrast mechanisms which depend on the crystal structure of the specimen. To a good approximation for a thin sample, the image intensity is determined by the absolute square of the structure factor $|F(hkl)|^2$. This factor is proportional to the amplitude of the electron wave at a particular scattering angle related to the (hkl) plane in question and is directly proportional to the Fourier transform of a unit cell in the direction of this plane. Equations (1.8) through (1.11) show how the structure factor is obtained for a crystal with an unit cell electron density function $\rho(\vec{r})$.

$$F(hkl) \propto \mathcal{F}[\rho(\vec{r})]_{hkl} \tag{1.8}$$

$$= \mathcal{F}[\sum_{j}^{N} \rho_j(\vec{r}) * \delta(\vec{r} - \vec{r}_j)]_{hkl} \tag{1.9}$$

$$= \sum_{j}^{N} f_j(\theta) \exp(i2\pi \vec{k}_{hkl} \cdot \vec{r}_j) \tag{1.10}$$

$$= \sum_{j}^{N} f_j(\theta) \exp(i2\pi(hx_j + ky_j + lz_j)) \tag{1.11}$$

Here $\mathcal{F}$ denotes a (3-dimensional) Fourier transform, j is the index of the N

[7]The terms "micrograph" and "image" are used interchangeably throughout this work.

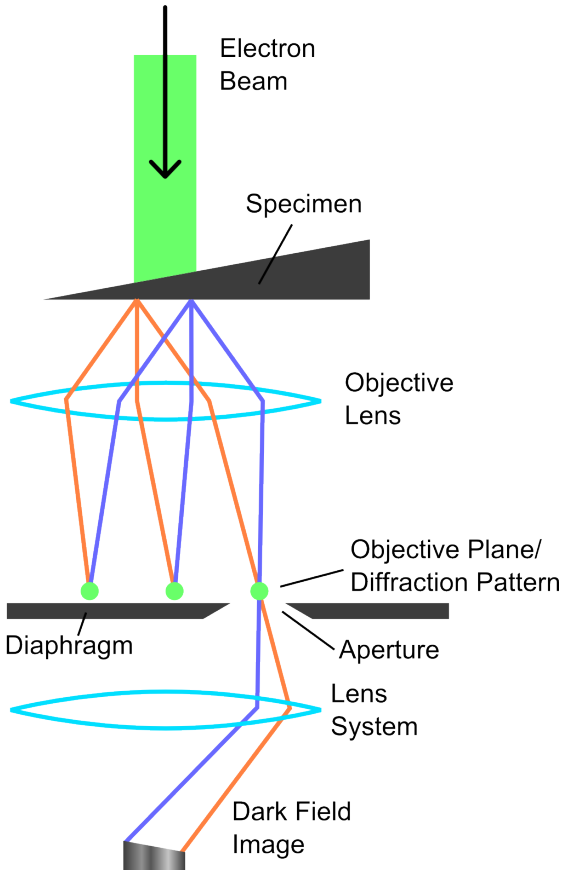

Figure 1.3: Microscope configuration for conventional dark field imaging.

atoms in the unit cell, ρ_j is the electron density function of an individual atom, $\delta(\vec{r}-\vec{r}_j)$ is a Dirac delta function centered at the atomic position $\vec{r}_j$ and $f_j(\theta)$ is the atomic form factor of the j^{th} atom. The diffracted angle θ is given[8] by $\theta = \lambda/d$ where d is the spacing of the (hkl) plane or $d = a/\sqrt{h^2+k^2+l^2}$ in the case of a cubic lattice with a lattice constant a and λ is the wavelength of the electron beam.

The III-V semiconductors in this work all have a zinc blende crystal structure which is similar to that of diamond except that half the atoms are group III atoms and the other half are group V atoms. Figure 1.4 shows the unit cell of a GaAs crystal as well as the view along the (110) and the $(\bar{1}10)$ directions or zone axes. Another way of defining this structure is using a face-centered cubic lattice with two atoms at each lattice point, that is, lattice points at 000, $\frac{1}{2}\frac{1}{2}0$, $\frac{1}{2}0\frac{1}{2}$, $0\frac{1}{2}\frac{1}{2}$, and at each point there is a group III atom at 000 and a group V atom at $\frac{1}{4}\frac{1}{4}\frac{1}{4}$. As a result the structure factor for the (002) spot is given by $F(002) = 4\cdot(f_{III}(\theta) - f_V(\theta))$

[8]Using the small angle approximation since λ is usually much smaller than d.

where $f_x(\theta)$ is the atomic form factor of the group x atom for the appropriate diffracted angle θ.

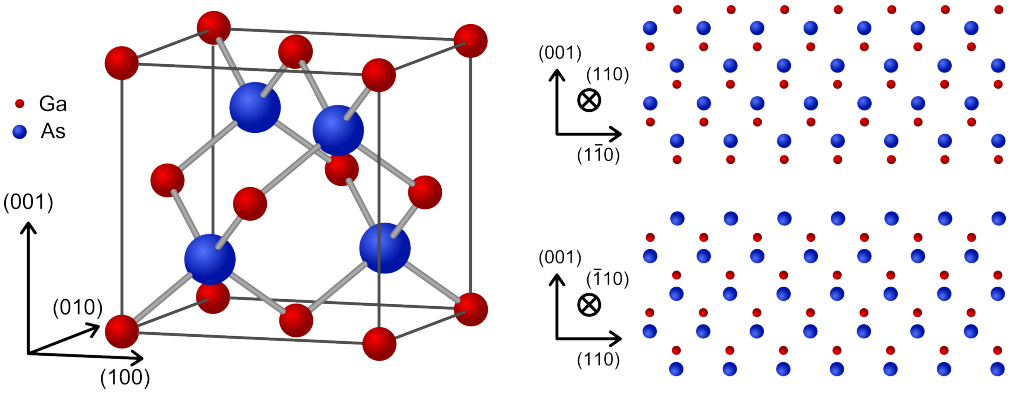

Figure 1.4: Zinc blende crystal structure.

What is important about this result is that the structure factor for the (002) reflection is proportional to the difference between the atomic form factor of the group III and group V atoms. This produces strong compositional contrast between the materials used in this work. By using the approximation that the atomic form factor for an element is its atomic number, we can estimate the relative intensity (structure factor squared) of the different compounds in our samples. The four main materials in our samples are InP, InAs, $In_{0.53}Ga_{0.37}Al_{0.10}As$ and $In_{0.53}Ga_{0.27}Al_{0.20}As$, and they should produce an intensity of 1, 0.222, 0.029 and 0.013 relative to InP, respectively. This means that in a (002) dark field image the InAs quantum wires appear bright within a dark InGaAlAs boundary layer above a bright InP substrate as shown in chapter 2.

Annular dark field STEM is similar to this imaging method in that only the diffracted electrons are used to produce the image. However it involves scanning the sample using a focused electron beam called a probe. As illustrated in figure 1.5, an electron beam is focused onto a particular part of the sample and a portion of the diffracted beam is collected on an annular detector at the back focal plane which is shaped like a disk with a large hole in its center. The portion that is measured is determined by the size of the detector and the camera length[9] which can be adjusted given it is placed after the projector lenses. The theory behind

[9]The camera length is just a distance that describes the magnification of the diffraction pattern.

this imaging technique is that heavier atoms[10] deflect electrons more strongly than lighter atoms and so the amount of electrons collected by the annular detector increases with the atomic number (Z) and the thickness of the sample. This leads to what is referred to as mass-thickness contrast where the measured intensity is roughly proportional to the square of the total mass (product of atomic mass and thickness of the sample) exposed to the electron beam. An image of the sample is rendered by rastering the beam over an area in a discrete manner where for each beam position, the integrated intensity over the detector is measured.

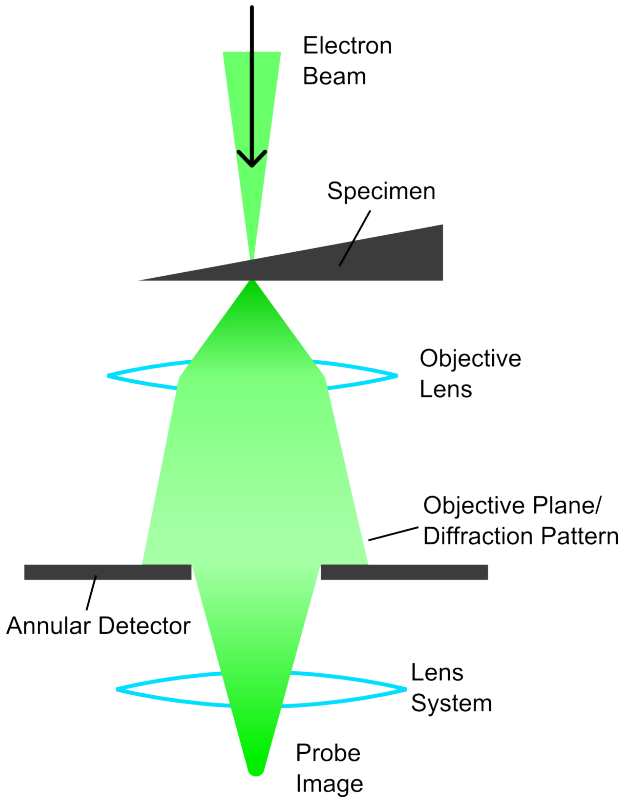

Figure 1.5: Microscope configuration for annular dark field imaging.

Furthermore, with the help of aberration corrected microscopes, it is possible to focus the beam to a probe which is smaller than the distance between the atoms of interest. Given that the specimen is properly oriented along a zone axis, it is possible to resolve individual atomic columns. Unlike high resolution TEM which suffers from variable contrast which strongly depends on focal conditions[10], ADF STEM provides a reasonably reliable and intuitive contrast mechanism, despite

[10]What is actually important is the charge of the nucleus but its weight is referred to for convenience.

effects such as channeling and beam spreading.

Channeling is a phenomenon where electrons become focused around atomic columns as they travel through a crystal. The problem is that the density of electrons can also oscillate between different columns as they traverse the sample and this means that the intensity observed on the annular detector does not only come from the column that the probe is on but others as well, depending on the nature of the sample. Beam spreading is also important and is closely related to channeling. Basically, due to the uncertainty principle, a large convergence angle determined by the condenser lenses and condenser aperture (large uncertainty in momentum) is required in order to form a very small probe (small uncertainty in position) and such a beam will spread rapidly, effectively resulting in a narrow depth of field. This implies that even though the probe may be very small at the top of the sample (in focus) it may be quite broad as it leaves the sample even without considering diffraction. Despite these potential drawbacks, with a thin enough sample it is possible to achieve atomic resolution and measure properties such as composition, strain and so on.

Chapter 2

Quantum Wire Growth

2.1 Overview

When depositing a heteroepitaxial thin film, three main growth modes are possible depending on the intrinsic properties of the deposited material and the substrate[3, 6]. Typically in an unstrained system where the two materials are lattice-matched, the Frank-van-der-Merve growth mode occurs where the thin film is deposited layer by layer. In this case, it is energetically favorable for the deposited material to form a flat epitaxial layer. If the materials are not lattice-matched, the accumulation of strain energy can lead to the two other modes. If the interfacial or bonding energy between the two materials is weak, the Volmer-Weber growth mode occurs in which the deposited material quickly agglomerates on the surface to form 3-dimensional islands. If the bonding energy is strong enough however, the Stranski-Krastanow (SK) mode dominates. In this mode, the deposited material initially forms a thin layer called a "wetting layer" and past a critical thickness, 3-dimensional islands begin to form. This growth mode is the most common for strained semiconductor heteroepitaxy and is illustrated in figure 2.1.

The critical thickness in this work refers to the amount of material measured in monolayers that is deposited before the formation of 3-dimensional islands begins.

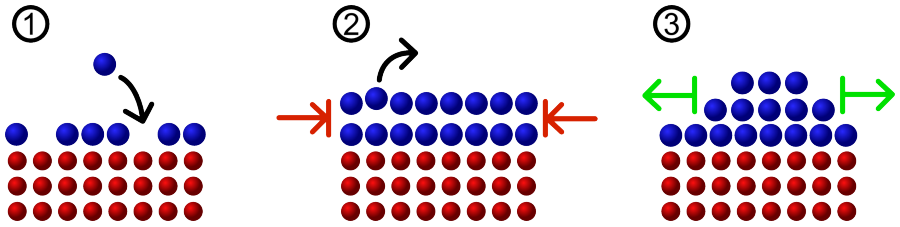

Figure 2.1: Evolution of Stranski-Krastanow growth: 1. The initial material is deposited and forms a wetting layer. 2. Strain energy accumulates. 3. Strain is relieved through relaxation in 3D islands.

It does not refer to the thickness before the formation of dislocations. Its value is affected by the amount of strain or lattice mismatch between the material being deposited and the substrate, as well as other parameters such as deposition rate and temperature. In the case where the lattice mismatch is greater, the thin film is more strongly driven to form islands to relieve strain and the critical thickness decreases. A faster deposition rate leads to a greater critical thickness but for an unintuitive reason[11]. For a lower deposition rate, more diffusion occurs between the deposited material and the substrate material, creating a more dilute but thicker film. Although the fact that it is more dilute reduces the effective lattice-mismatch of the thin film, the layer's thickness has a greater effect on the appearance of islands and reduces what is sometimes called the "effective" critical thickness[1]. Note that no bulk diffusion is required for this process but rather surface diffusion is sufficient.

The average size of these islands is mainly determined by the bonding energy of the deposited material, the lattice mismatch between it and the substrate, and the stiffness of the material since islands form to relieve strain energy at the expense of broken bonds. This means that stronger bonds lead to the formation of larger islands and a higher Young's modulus leads to smaller islands. This intuitive effect is demonstrated in chapter 3. Of course, other growth parameters such as deposition rate and temperature can affect their size as well but what is perhaps most important about this relationship is that it indicates an intrinsic or "natural" island size for self-assembled structures. As for the preference of wire growth along the $(\bar{1}10)$ direction over dot growth, this is caused by either effective anisotropic

[1]The effective critical thickness is the critical thickness based on the amount of material deposited, not the actual thickness of the deposited film due to diffusion.

bonding at the surface due to the surface reconstruction based on our findings or by a "trapping" mechanism discussed in [12]. We demonstrate in section 3.6.1 that the seemingly intuitive argument involving faster surface diffusion along the $(\bar{1}10)$ direction [13] is not the cause of the formation of wires.

2.2 Growth Conditions

Based on previous investigations of InAs quantum wire growth by a former Ph.D. student, Dr. Kai Cui [14], self-assembled wires are best grown by depositing 3.5 to 5.6 monolayers (ML) of InAs at 520 °C at a deposition rate of 0.4 ML/s. These parameters were therefore used as a guide for our own growths. Eight growth experiments were conducted following the general growth profile illustrated in figures 2.2 and 2.3 using the on site MBE chamber.

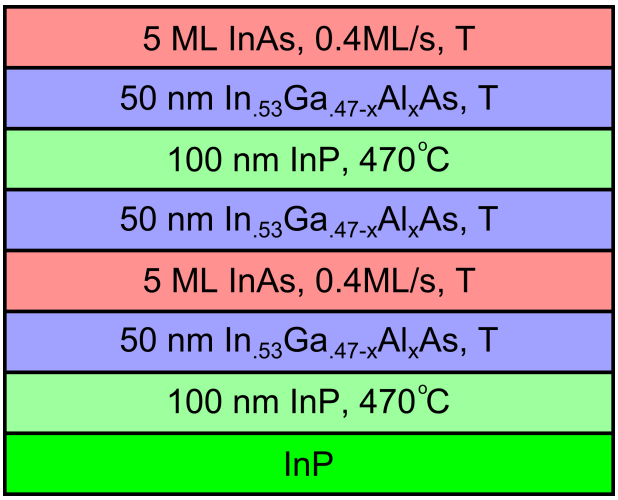

Figure 2.2: Quantum wire growth parameters common to all experiments where T is the temperature indicated in table 2.1. Additionally the V/III ratio was 4.

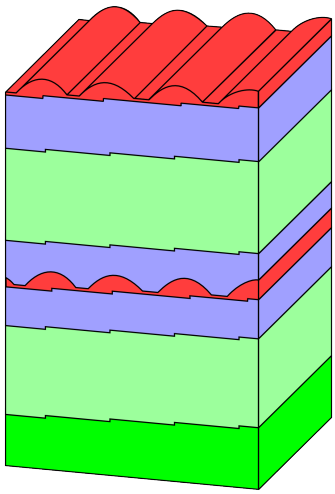

Figure 2.3: 3-Dimensional rendering of the growth including surface steps. (not to scale)

The experimental procedure consists of first cleaving the 2" InP wafers into quarters. This is done by making a small scratch on the face of the wafer in the middle of the large flat using a scriber. Figure 2.4 illustrates a wafer as it is received by the manufacturer with a large flat and a small flat which are polished off by the manufacturer in order to indicate the orientation of the substrate. Once the

scratch has been made, pressure is carefully applied to the wafer until it cleaves along the $(\overline{1}\overline{1}0)$ direction. This is repeated along the perpendicular direction for both halves of the wafer and the quarters are cleaned using a nitrogen duster.

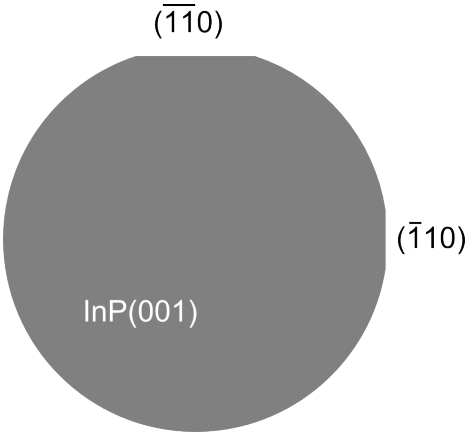

Figure 2.4: InP wafer (actual size).

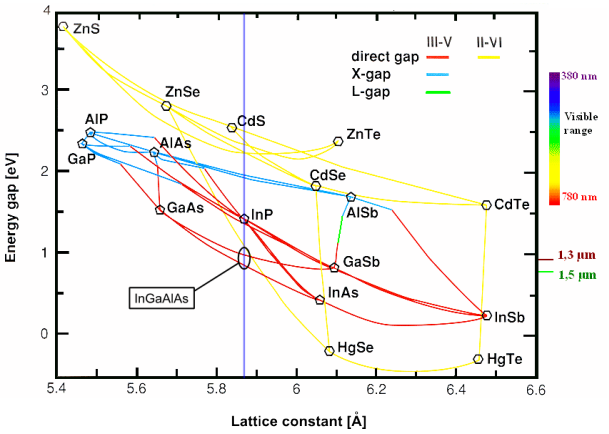

Figure 2.5: Bandgap vs. lattice constant for various semiconductors[15].

The quarter wafer is then placed in a holder and inserted into the loading chamber of the MBE system. After evacuating this chamber, it is inserted into the center of the main chamber where it is cleaned using a hydrogen plasma while heated at 470 °C. An InP buffer layer is then deposited in order to ensure a pure deposition surface by exposing the substrate to the molten In source and cracked phosphine. The temperature of the metals and the pressure of the gases for a desired deposition rate are all calibrated beforehand by growing test thin films and performing X-ray diffraction measurements. A phosphorous overpressure[2] is maintained while the substrate is heated to the desired temperature.

The phosphorous is then evacuated from the chamber and the quaternary alloy (InGaAlAs) is deposited at a rate of 1 ML/s by exposing the substrate to the three metals and cracked arsine gas. The composition of this alloy is chosen to be lattice-matched to InP based on the diagram in figure 2.5. This layer is referred to as the barrier layer and is used to confine the carriers (both electron and holes) within the InAs quantum wires. Although a lattice-matched material could be made using only InGaAs, the aluminum content provides additional control over the bandgap and band alignment. In fact, some aluminum is required to achieve

[2]The term "overpressure" is used to denote a pressure greater than that required to maintain group V atoms on the surface of the sample and to control the surface reconstruction.

proper confinement of holes. Based on the parameters given in [16], the valence band offset (VBO)[3] of $In_{0.53}Ga_{0.47}As$ is -0.594 eV which is nearly the same as that of InAs which is quoted as -0.59 eV. In contrast, the valence band offset of $In_{0.53}Ga_{0.37}Al_{0.10}As$ and $In_{0.53}Ga_{0.27}Al_{0.20}As$ is -0.74 eV and -0.79 eV. These bandgaps are illustrated in figure 2.6. Also, the fact that AlAs and GaAs have a very similar lattice constant can be practical since Ga and Al can be interchanged to vary the bandgap without affecting the lattice constant nor the quantity of In required. Regarding quantum structures, aluminum has a stronger bonding strength which can also affect the formation of the self-assembled wires.

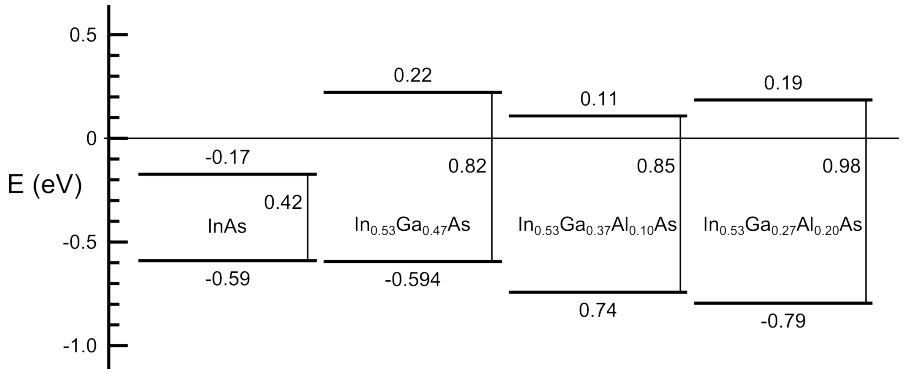

Figure 2.6: Band gap alignment of InGaAs and InGaAlAs compared to that of InAs.

Following the quaternary alloy, InAs is deposited to form the quantum wires. This was done by periodically opening and closing the shutter in front of the In effusion cell to achieve the desired average deposition rate. In all experiments, 5 ML of InAs were deposited over a period of 12.5 s for a deposition rate of 0.4 ML/s. The V/III ratio used in these experiments, that is, the flux of the group V atoms (As) over that of the group III atoms (In) was 4. This ratio is important for controlling the surface reconstruction as well as the surface energy during epitaxial growth using MBE. The wires are then covered by another barrier layer for confinement and as indicated in figure 2.2, the procedure is repeated under the same conditions but this time without covering the quantum wires. This capping layer is included for characterization of the surface wires using either scanning electron microscopy (SEM) or atomic force microscopy (AFM).

[3]The valence band offset defined in [16] is the valence band edge energy relative to that of InSb.

The parameters specified above were maintained for all growths and the parameters that were varied are listed in table 2.1. Eight growth experiments were performed by changing: the temperature during the growth of both the quaternary alloy and the InAs, the aluminum content of the quaternary alloy and whether the substrate was nominally flat or off-cut.

Sample	Growth #	Temperature	% Al	off-cut
				±0.1
A	1391	520	10	0.0
B	1392	520	10	0.9
C	1393	520	20	0.0
D	1394	520	20	0.9
E	1447	535	10	0.0
F	1448	535	10	0.9
G	1449	535	20	0.0
H	1450	535	20	0.9

Table 2.1: Variable growth parameters for all 8 experiments. The growth number is included as a reference.

The growth temperature affects the surface diffusivity of the adatoms. At higher temperatures, adatoms have more thermal energy which allows them to move more frequently on a surface. Basically, they are able to "hop" along the surface more often per unit time. For a constant deposition rate, this can give them a better opportunity to find lower energy adsorption sites before either being buried by other incoming atoms or bonding to other adatoms to form islands. The aluminum content, as mentioned above, modifies the band gap and provides stronger bonding sites than gallium. Finally, each experiment was conducted on either a nominally flat or a vicinal (off-cut) substrate.

The idea behind growth on off-cut substrates is to provide surface atomic steps as uniform nucleation sites for the quantum wires and each experiment is repeated on a nominally flat substrate for comparison. As illustrated in figure 2.3, our intention was for one wire to nucleate at each surface step. In the case of InAs grown directly on InP, it has been shown that some wires form directly at the surface steps [17] and some work has shown an improvement in the size distribution of quantum wires grown on vicinal substrates [4] but using an arbitrary off-cut angle. For our experiments, we chose an off-cut angle of 0.9° as indicated in table

2.1 based on two observations. Firstly, the average spacing of the wires from one of Dr. Cui's growths was measured by preparing a TEM wedge from one of his old wafers. The separation of the wires was between 18 and 20 nm. Secondly, based on observations from Salem's work [4], the wires on the off-cut substrate were narrower on average than on flat substrates. The off-cut angle in our experiments was then chosen such that the length of the atomic steps or terraces is $L = 18$ nm, the lower end of our spacing measurements. If nucleation properly occurs at the steps, this would hopefully favor the natural wire spacing observed on flat substrates and lead to the growth of more uniform self-assembled quantum wires.

Finding the appropriate angle is a matter of simple geometry. Because of the group V overpressure, the surface of the substrate is always covered by group V atoms such as As and growth is exclusively limited by the group III atoms such as In. For this reason, unlike for silicon or germanium, (100) off-cut substrates have diatomic steps[4] instead of monatomic steps as illustrated in figure 2.7. The step height for InP is therefore half its lattice constant ($h = 2.93$ Å[18]) and the required off-cut angle is given by $atan(h/L) = atan(0.293/18) = 0.93°$.

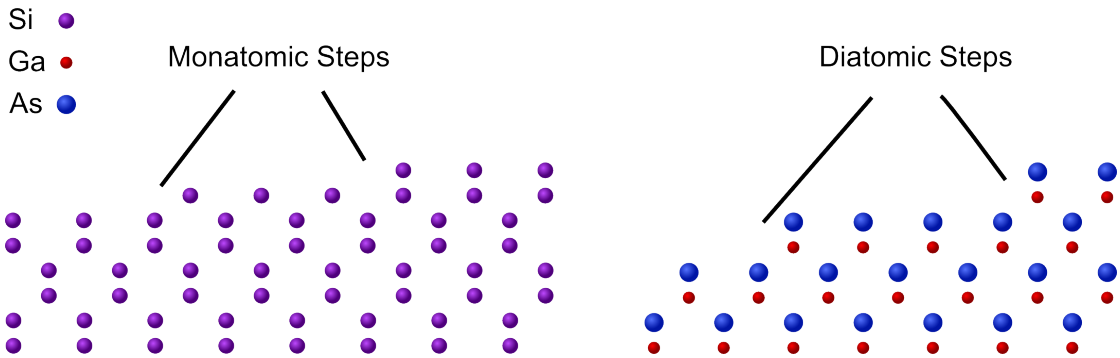

Figure 2.7: Group IV semiconductors have monatomic step whereas III-V semiconductors have diatomic steps under MBE growth conditions.

As for the direction of the off-cut, the polished surface was angled towards the (110) direction as to provide surface steps along $(\bar{1}10)$ which is the orientation of the quantum wires. Finally, the nominal InP (100) substrates were provided by the MBE operator and the vicinal substrates were obtained from Wafer Technology Ltd. in the U.K. with an off-cut angle of $0.9 \pm 0.1°$.

[4]The diatomic steps are referred to as just atomic steps for simplicity.

2.3 Sample Preparation

After growth in the MBE chamber, the wafer quarters must be cleaved, polished and ion milled into proper TEM samples. The whole procedure is illustrated in figure 2.8.

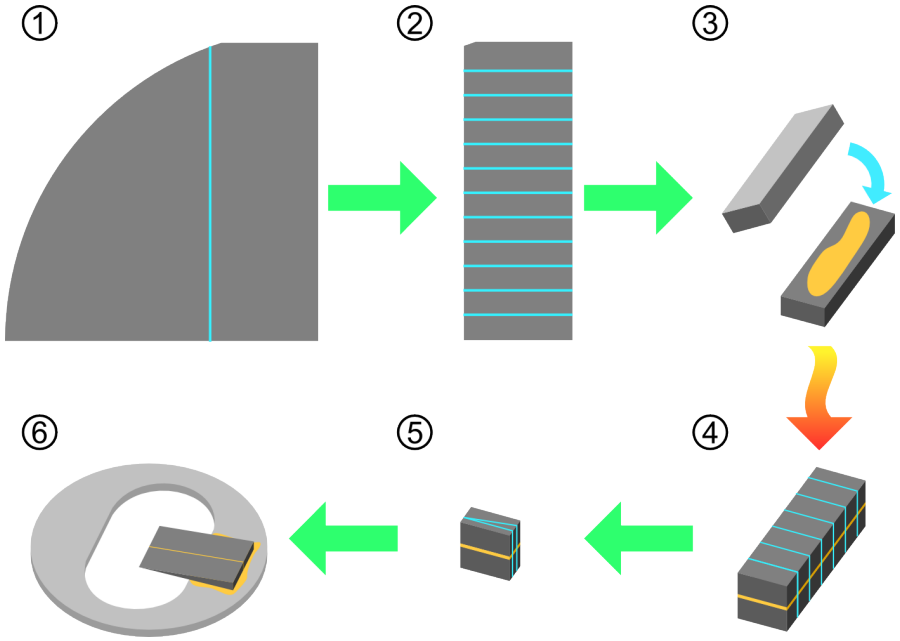

Figure 2.8: The various steps of TEM sample preparation. Blue lines indicate cleaving, cutting or polishing and epoxy is shown as yellow.

The process begins by cleaving a quarter wafer into smaller pieces using a scriber-mounted optical microscope. This is done by first placing the glossy side of the quarter (the side which has wires) on the blue side of residue free sample preparation plastic and aligning the whole under the scriber of the microscope. A straight line is scratched onto the rough side of the wafer as indicated by step 1 in figure 2.8 and the wafer is cleaved by covering it with the clear plastic layer and carefully applying pressure on both sides of the line over a sharp edge such as the edge of a microscope slide. The width of this piece is roughly 8 mm although the exact dimensions are not important. Next, this long piece is cut into 1.6 mm wide strips using a similar procedure as shown in step 2. The width of these strips is important since it will influence the final length of the wedge sample which must be placed on the 3 mm molybdenum ring and the tip of the wedge should ideally be in the center of the ring. The value 1.6 is chosen as it is just a bit more than

the radius of the ring and some of the material at the tip of the wedge will be lost during its preparation.

Next, two of these 8 mm by 1.6 mm strips are glued together using a freshly mixed 10 to 1 epoxy mixture (Epoxy Technology 353ND Kit part A & B), tightly clamped using alligator clips and heated for about 10 minutes for the epoxy to set. To verify that the glue has been sufficiently heated, an extra drop of epoxy can be placed on one of the aligator clips and it should turn dark red when it is set. The resulting glued strip is cut into ∼1.2 mm thick bars using a diamond wire saw. These bars are now ready to be polished into wedges using the Allied High Tech Products MultiPrep^{TM} System.

The first side of the bar is polished flat by gluing it onto the appropriate small metal holder using a polymer (Crystalbond^{TM} 509 Thermo polymer) and for the first side only, it is possible to polish two samples at once. The diamond lapping films that are typically used for the polishing process are the 30 μm film (green)[5], the 9 μm film (blue), the 3 μm film (pink), the 1 μm film (purple) and finally the 0.5 μm film (white). To be on the safe side, it is recommended for each lapping film to grind away 5 times the previous grit size. That is, 150 μm ($5 \cdot 30$) using the 9 μm film, 45 μm ($5 \cdot 9$) using the 3 μm and so on, although this is just a general guideline. The loading pressure that is used for InP is usually around 100 g, that is, the "1" mark on the device. Each polishing step is executed using a lint free tissue to wipe off the lapping film and under running water except for the last step (0.5 μm) where a mixture of approximately 80% ethanol, 10% isopropanol and 10% ethane-1,2-diol (ethelene glycol) is used as a lubricant. The final thickness after this step should be around 700 μm. After the final polish, the quality of the polished side is inspected using an optical microscope to verify that no pits have formed. The lubricating alcohol mixture is of great help at this point. If need be, the polishing process using the 0.5 μm lapping film is repeated until the result is satisfactory.

Once the first side is complete, the bar is removed from the metal holder by heating it. While it is being heated, a Pyrex holder is polished flat using the 30

[5]The 30 μm film is optional and depending on the initial thickness of the bar, using the 9 μm film from the start may be more convenient.

μm film followed by the 3 μm film. The polished side of the specimen is glued onto the Pyrex using the polymer and this part can be quite tricky. The specimen must be pressed onto Pyrex hard enough to be even with it. If there is more glue on one side than the other, it will be difficult to make a proper straight wedge. For this reason, it is also important to make sure that the polymer is hot and fluid. Care must be taken however in applying pressure onto the sample as not to scratch it on the holder. Applying too much pressure can also leave too little glue to hold the sample in place when polishing it. A small lip of the sample should be hanging roughly 0.2 mm past the edge of the Pyrex. Then a similar polishing procedure is followed as above. After using the 9 μm film, the sample should be around 200 μm thick and at this point a 2° tilt is applied to the holder by advancing the tripod screw closest to the user by 1 mm. After using the 3 μm film for just a few seconds, the wedge begins to form and at this point it is possible to see if the sample needs to be tilted about its long axis. If the newly polished area is not rectangular, that is, the edge of the sample is not parallel to the line between the two different polished regions, the rightmost screw can be adjusted in increments of about 0.05 mm to correct for this.

Once a thickness of 50 μm is achieved using the 3 μm film (at the thin end), the 1 μm film is used. In this step, the sample is polished until the overhanging lip of material breaks off from it and the protruding edge of the Pyrex holder begins to be polished. As before, the 0.5 μm lapping film is then employed along with the alcohol mixture until the sample is defect free near the glue line. Between two and four thickness fringes should be visible at this point and the wedge can be removed by placing the holder in a dish lined with filter paper and filled with acetone. The holder should be placed in the same orientation as in the polisher (with the sample "hanging" from the bottom). Once it has fallen away from the Pyrex, it can be gently cleaned by removing the acetone and flushing with ethanol several times. Finally, the sample is glued onto the molybdenum ring using a very small amount of 10 to 1 epoxy. It is then left to cure overnight.

It is possible for the sample to be TEM ready at this point but typically ion milling is required due to minor damage incurred during the cleaning process. This was done using the Gatan precision ion polishing system (PIPS^{TM}) which

uses an Ar^+ beam and the holder must be liquid nitrogen cooled to prevent the formation of In droplets due to the evaporation of phosophorous from the InP[6]. The "double" beam modulator was used in order to prevent damage to the holder and the rotation speed was set to 3 rpm. The accelerating voltage was set to 3 keV and the incidence angle was set to $\pm 6°$.

Since the main purpose of ion milling is only to "repair" the wedge, less than 5 minutes is usually all the time required. A noteworthy characteristic of the wedge is that it is rippled after removal from the Pyrex mount and the undulations in the wedge are quickly and noticeably removed during the ion milling process. Other damage features such as small chips are usually "ironed out" given that they are small enough. Generally, however, less milling time is better since the quaternary alloy is milled away more slowly than the substrate material and this produces an undesirable bend around the region of interest.

Finally, additional milling using the Fischione NanoMill was performed on some samples (liquid N_2 cooled) using a 500 keV Ar^+ beam and for HRTEM, they were plasma cleaned for about 15 minutes with an O_2 and H_2 plasma using a Gatan Solarus^{TM} (Model 950) Advanced Plasma Cleaning System to remove contamination.

2.4 Size Distribution Assessment Using SEM

One of the major disadvantages of cross-sectional TEM is that the investigated area is much smaller than the sample of interest, in our case, an InP wafer quarter. Due to the size and distribution of the quantum wires on the surface of wafer, it is very difficult to get an accurate idea of their size distribution using TEM. A cross-sectional specimen only allows us to observe a thin profile of a few dozen wires and gives us little information about their 3-dimensional shape. As mentioned in section 2.2, the top layer of quantum wires was deposited specifically for this purpose and using scanning electron microscopy (SEM), this section characterizes the shape of

[6]It is worth mentioning that the quantum wire region may remain protected from the In droplets by the InGaAlAs layers.

the quantum wires produced under the aforementioned growth conditions.

The way an SEM works is similar to STEM in that an electron beam is rastered over the specimen and for each position, a detector collects electrons to produce the intensity of a corresponding pixel in order to form an image. A secondary electron detector in an SEM is used to collect relatively low energy electrons ejected from the specimen near the impact area of the electron beam. Figure 2.9 illustrates secondary electrons escaping the sample from four different areas and a secondary electron detector in the top right corner[7].

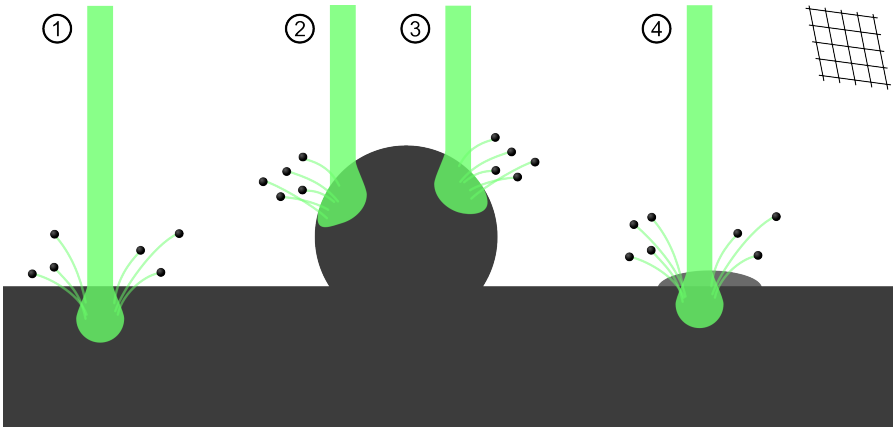

Figure 2.9: An electron beam ejecting secondary electrons in an SEM at four different locations. The grid at the top right represents the secondary electron detector.

The bulb-shaped volume at the bottom of the four beams represents the interaction volume which is the volume from which secondary electrons are ejected and the size of these regions depends on the energy of the incoming electron beam (incident energy). This volume affects the actual resolution of the microscope as it effectively smears out the "response" of the sample. This mechanism also leads to topographical contrast based on the incident angle of the beam and shadowing.

The first beam in figure 2.9 impinges on a flat part of the sample which is perpendicular to its direction. The secondary electrons in this case will be ejected isotropically and the charge collected by the detector, and therefore the intensity in the micrograph, will be the same regardless of the location of the detector unless

[7]The secondary electron detector is actually behind the illustrated metal grid which is positively charged to accelerate and attract these electrons.

there is an object between this area and the detector such as the round particle illustrated here. This leads to a shadowing effect where crevices seem darker than large flat areas. The second beam hits a particle on the sample at a steep angle and this allows for more secondary electrons to escape the interaction volume (sideways). However, since the detector is on the opposite side of the particle, a similar shadowing effect occurs here and the resulting measured intensity is low. On the right side of the particle, the third beam again ejects many secondary electrons and this time many of them can be detected which leads to a bright area. All these shadowing effects result in an image which appears to be lit from the direction of the detector which reveals good topographical contrast and images which are intuitive to interpret.

In the case of our quantum wires, beam 4 illustrates how the brightness is not much different from one side of the wire to the other due to their small size as well as the shallowness of the edges which leads to little shadowing. More electrons escape from the sides of the wires when the beam is on them than between them, though and this provides contrast. Some anisotropy has been observed in some images and this is pointed out below. Since this effect is small however, secondary electron SEM images of our quantum wires are nearly 2-dimensional height profiles which are great for image analysis.

2.4.1 SEM Observations

Figures 2.10a through 2.11d are secondary electron SEM images of samples A through H taken with the FEI Magellan 400 XHR in secondary electron mode using the through-lens detector. The magnification in each of these images is 200kx and this was chosen based on the amount of detail that was possible to resolve, a reasonable acquisition time and a convenient number of pixels per wire for image analysis. In all images, the scanning direction was aligned such that the $(\bar{1}10)$ direction is vertical. This is not only a personal choice but also helped the drift correction software properly track the sample as the images were acquired. This correction usually consists of taking multiple images by scanning quickly,

translating them in order to find the best match[8] and adding them up. This technique is useful for performing long acquisitions without suffering from blurring due to any movement of the sample. This process accounts for the dark edges around some of the images, notably in figure 2.10c.

Figure 2.10a is less sharp than the other 7 images due to residual astigmatism but still allows us to visually distinguish the wires both horizontally as well as their tips or ends. If we begin by comparing the first four images, we can see that the wires all have similar characteristics. They are all generally aligned along the same direction which is expected since they appear due to anisotropy between the (110) and the ($\bar{1}$10) directions, although some wire segments are tilted by up to 20°. All four substrates have what appear to be a few larger isotropic islands or quantum dots either isolated from or as part of wires. At these locations it is possible to observe that the bottom edge of the dots is slightly brighter than the top edge which reveals a small amount of anisotropy due to the location of the secondary electron detector, even though a through-lens detector is used. These dots are not to be confused with the bright spots in figure 2.10a which appear to be some form of contamination upon closer inspection. We can also see that some wires are joined by Y-shaped intersections and sometimes even reconnect, forming elongated loops. As for the size distribution, which is after all the main aspect of interest, there is no clear visual improvement of samples B and D, which were grown on vicinal substrates, over samples A and C. This is in contrast to the apparent improvement observed in [4]. The wires do seem to be a bit more densely packed in C and D compared to A and B as there are fewer exposed areas and this could be explained by the increase in aluminum content which increases the bonding strength of the substrate. However, given the amount of variability in the next four samples (E through H), such conclusions may be unwarranted.

Figures 2.11a through 2.11d show much more variability. First of all, samples E, G and H show many large exposed regions as well as a large number of dots which was unexpected. The difference between samples E and F is the most impressive but cannot be simply attributed to the off-cut angle of the latter, especially considering the lack of distinction between samples G and H. Based on

[8]This can be done by finding the location of the global maximum of a 2D cross-correlation between two images.

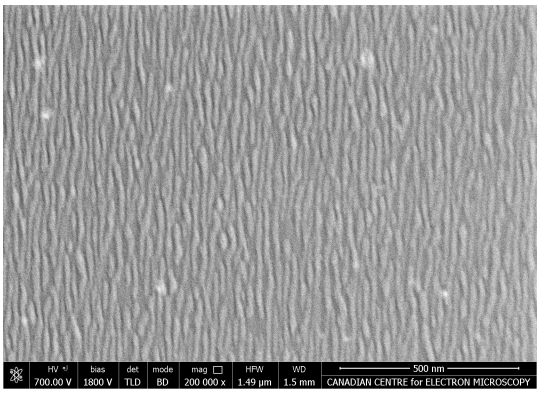

(a) Sample A.

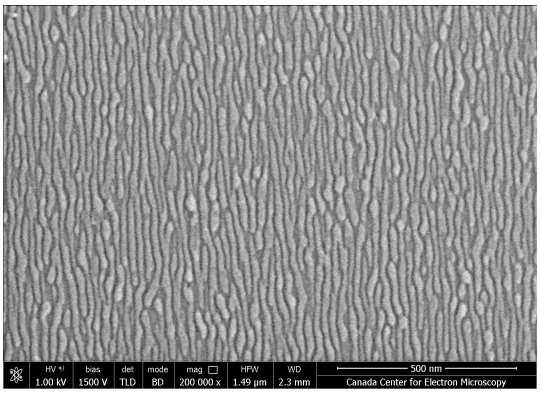

(b) Sample B.

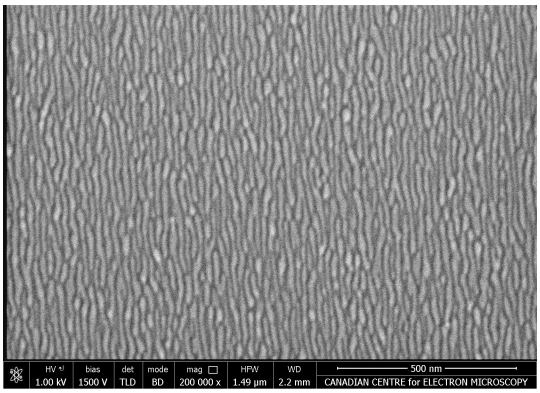

(c) Sample C.

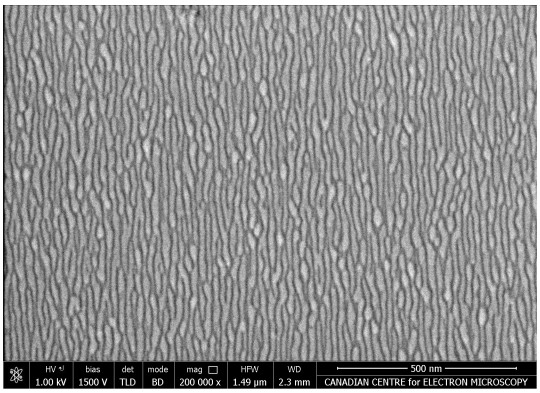

(d) Sample D.

Figure 2.10: SEM micrographs of the surface quantum wires at 200kx magnification. These are the samples grown at 520°C. Samples A and C were grown on a flat substrate whereas B and D were grown on vicinal substrates. The aluminum content in A and B is 10% and that in C and D is 20%.

experiments by other research groups, this coalescence may have occured during the annealing[9] process[19]. In their work, longer annealing periods lead to the migration of the wire material toward large round islands or dots. The likely culprit in our case is therefore an unintended difference in annealing conditions between the different samples. The annealing time after the deposition of the buried wires is well controlled since the quaternary alloy is deposited a precise amount of time after the InAs deposition phase. There is much more discrepancy however in the time that passes between the end of the deposition of the top layer of InAs and when the substrate is cooled down to room temperature to be removed from the chamber. Furthermore, considering that most of the dots observed here are either vertically aligned with bare regions or connected to what seem to be shallower

[9]Annealing in this case is the process of keeping the substrate hot without depositing any new group III material once the deposition is over.

(fainter) wires, it is a reasonable hypothesis that the InAs has diffused from these regions toward the dots. The fact that this occurred during the hotter (535°C) growths rather than the colder ones (520°C) supports this theory since diffusion occurs more readily at higher temperatures.

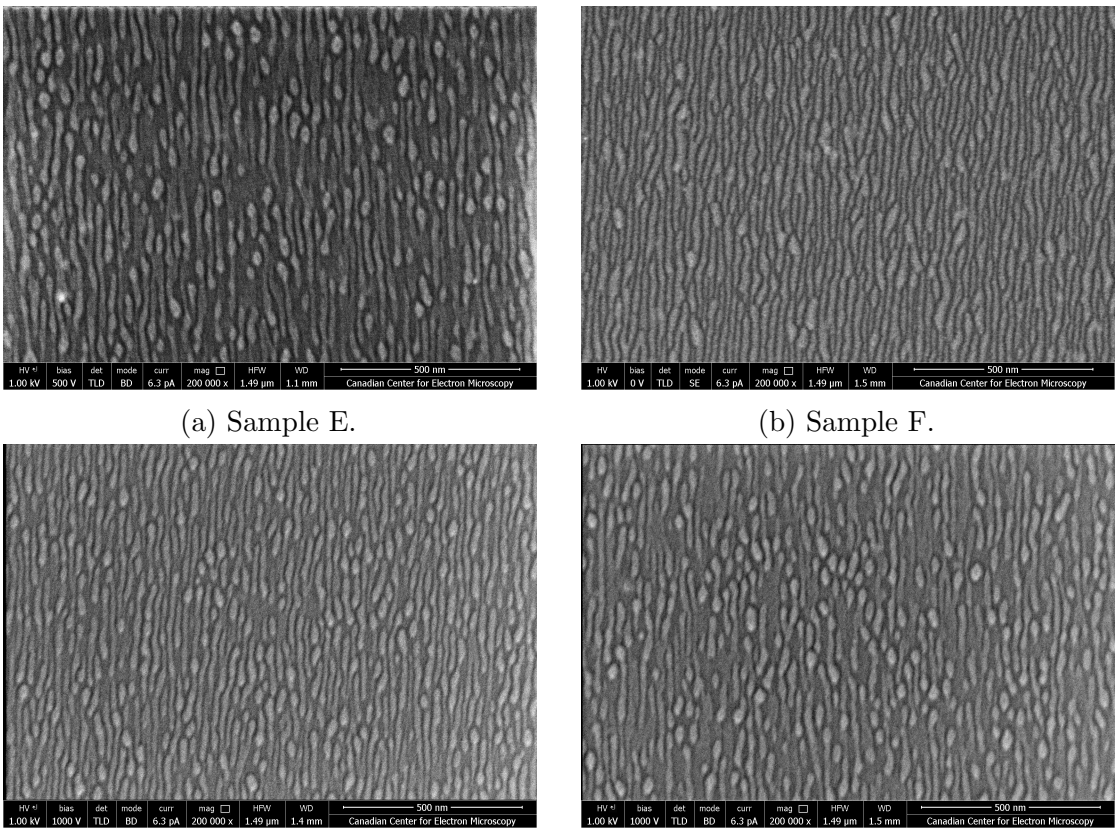

(a) Sample E.

(b) Sample F.

(c) Sample G.

(d) Sample H.

Figure 2.11: SEM micrographs of the surface quantum wires at 200kx magnification. These are the samples grown at 535°C. Samples E and G were grown on a flat substrate whereas F and H were grown on vicinal substrates. The aluminum content in E and F is 10% and that in G and H is 20%.

From the perspective of the bonding model developed in section 3.4 and from the fact that the predicted surface energy[8] for the $\gamma_{\bar{1}11}$ is expected to decrease sharply with an increase in the As chemical potential [10] μ_{As}, the In bonds are expected to be more isotropic once the deposition of In ceases. It is then reasonable to expect the InAs to form more isotropic structures such as quantum dots. Additionally, based on the TEM images presented in figures 2.16, 2.19, 2.17 and 2.20 of section

[10]The chemical potential μ_{As} increases with either an increase of As overpressure or and interruption of the group III pressure which causes $\gamma_{\bar{1}11}$ to decrease.

2.5, the configuration of the buried wires and surface wires in sample F seem to match well whereas those in sample E do not. Figure 2.19 shows a heterogeneous undulated surface with flatter sections which may very well correspond to the bare regions of figure 2.11a.

2.4.2 Wire Size Distribution

Despite the problematic SEM results for samples E, H and to some extent sample G, all 8 images in figures 2.10 and 2.11 were analyzed in order to obtain the size distribution, or more precisely the spacing distribution, of the grown quantum wires. For this purpose, a script was written in MATLAB to automatically locate the position of the wires and measure their spacing. The script performs this task in a series of steps. The first objective as with many other image analysis tasks is to produce a binary (black and white) image where the wires are highlighted. With an ideal SEM image, this could be done using simple image segmentation where the pixels of the image are categorized as above or below a trehshold value. Due to noise this is not possible but this problem is resolved through the application of a few Fourier filters.

Since we are looking for local brightness variation on the length scale of the width of the wires and do not care about the overall brightness of large areas, we begin by applying a 2D low frequency high-pass filter of the form $I' = I - g(\sigma = 50) * I$ where I and I' are the image[11] before and after the filter, $g(\sigma)$ is a 2D normalized Gaussian function with a standard deviation of σ and $*$ is the symbol used for convolution[12]. The numerical values here are in pixels and only serve as a general reference to convey a better understanding of the relative magnitude of the various filters. Next, the mean value of the image is subtracted from every pixel to assure that a threshold of 0 will affect all images in a similar way. A low pass filter is then applied to the image to blur out the graininess and only keep the important spatial frequencies of the wires. The image then becomes $I' = g(5) * I$ and as an example, the result of these transformations is illustrated in figure 2.12 which is

[11]The image can be interpreted as a 2-dimensional function.

[12]The convolution is evaluated in reciprocal space to take advantage of the efficiency of the fast Fourier transform (FFT).

the Fourier filtered version of figure 2.10b. Once this is done, a treshold of 0 is applied and the result is shown in 2.13.

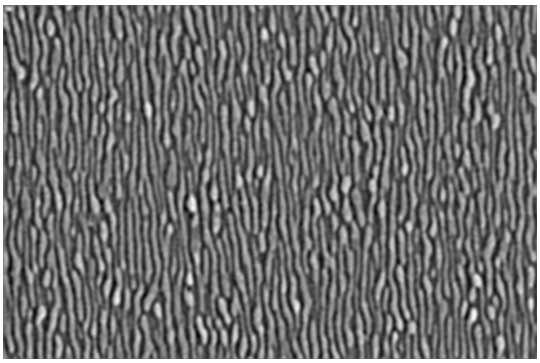

Figure 2.12: Bandpass filtered version of figure 2.10b for locating wires.

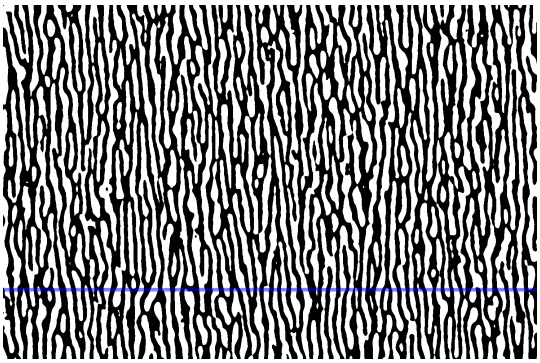

Figure 2.13: Binary image highlighting the wires from figure 2.10b. The blue horizontal line is a 10-pixel high band over which wire separations are measured.

Using MATLAB's image processing toolbox, the different wires can be separated, counted and other properties such as their area and location can be determined. However, due to the shape of the wires and how some have branches, analyzing the regions of the binary image is not straightforward. For this reason, the image was broken into 10-pixel high horizontal strips as part of our analysis as indicated by the blue band in figure 2.13. Furthermore, since the thickness of the detected wires can depend strongly on the filters that are used, the chosen threshold and the general quality of the image, the separation between the middle of the wires within these thin bands was measured instead. This proves to be a much more reliable measurement as it does not depend on the width of the individual white regions in figure 2.13 but rather their center within horizontal strips. However, one problem with this method is that where there are vertical gaps between wires (past the tips), the separation between the wires on both sides of this gap is measured and this is an overestimate of the actual wire spacing. Fortunately, this turns out to be a fairly small contribution as indicated by the tail of the following plots.

Figures 2.14 and 2.15 show the spacing distribution of all 8 samples based on the SEM images above. The graphs include the mean and standard deviation[13] for each of the curves and these represent the average spacing and its variability.

[13]Note that this is the standard deviation (width) of the distribution, not that of the mean.

The curves in figure 2.14 are all fairly similar and two important observations can be made. The first is that the wires grown on the substrates with the higher aluminum content are on average narrower which is unexpected since aluminum provides stronger bonds which intuitively would lead to larger wires based on the balance between strain energy and bonding energy.

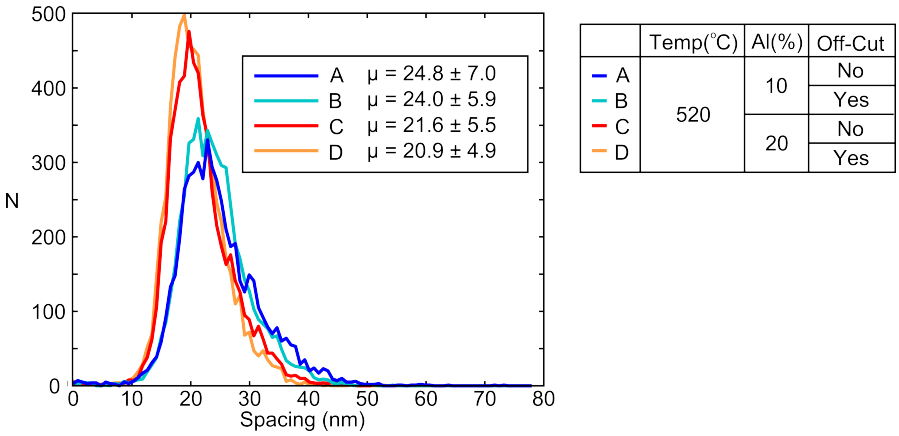

Figure 2.14: Spacing distribution of the wires from samples A through D.

The second important observation is that the size distribution of the wires grown on the off-cut substrates is narrower than on the nominally flat substrates as shown by the standard deviation for samples B and D compared to A and C. This is in agreement with other work[4] done on substrates with a 2° off-cut, although the difference in our case is not as substantial. Determining whether this difference is significant is tricky however. The expression for the error on the width of a Gaussian distribution[14] is given in equation (2.1) [20]. In this expression, σ_σ is the error on the width and σ is the measured value of the width or the standard deviation. The difficult part of our analysis is to determine the value of n which is the number of *independent* measurements. Technically the number of spacing measurements made in our image analysis is on the order of 4000 to 6000 but this is arbitrary since it depends on the chosen height (10 pixels) of the horizontal strips. This value could be chosen differently and affect the number of measured wire spacings, and each window is definitely not independent of its neighboring windows. It is also clear that the total number of wires would greatly underestimate the number of independent measurements since the spacing and width of a wire varies significantly along its length.

[14]This is in fact the standard deviation of the standard deviation.

$$\sigma_\sigma = \frac{\sigma}{\sqrt{2(n-1)}} \tag{2.1}$$

A reasonable value for n can be obtained by dividing the total area of the analyzed images by a reasonable upper limit of the spacing distribution, squared. That is, since most of the area under the curves in figure 2.14 is below about 30 nm, we can use as an upper limit of a total number of independent measurements, $n = w \cdot h/30^2$ where w and h are the width and height of the image in nm. This gives us roughly $n \approx 1600$ and the error on the probability distribution width is therefore $\sigma_\sigma = \sigma/\sqrt{2 \cdot 1600}$. which is on the order of 0.12 nm for the values of σ above. This means that the improvements of $7.0 - 5.9 = 1.1$ nm and $5.5 - 4.9 = 0.6$ nm are significant and based on the measured statistics of the wire spacing distribution, the growth on off-cut substrates has significantly improved the size distribution of self-assembled quantum wires. Although significant, the improvement is still modest and less than the desired outcome of this experiment.

The case is obviously different for samples E through H, however. Due to the large amount of coalescence and bare regions in figures 2.11a, 2.11d and somewhat in 2.11c, no important conclusions can be made regarding the spacing distribution of the wires. Figure 2.15 shows the probability distribution of the wire spacing plotted on the same scale as the plot for samples A through D for visual comparison. We can see a distinct broadening of the H and E curves with respect to the two others as a result of the coalescence as well as an increase in the average spacing, both due to what is believed to be an annealing process.

2.5 TEM Characterization

Cross-sectional TEM allows us to characterize the buried wires which, after all, are the more important ones. Using the (002) spot, dark field images can be obtained which reveal strong compositional contrast as indicated by the equations in section 1.4. Figures 2.16 and 2.17 show dark field images of samples E and F obtained

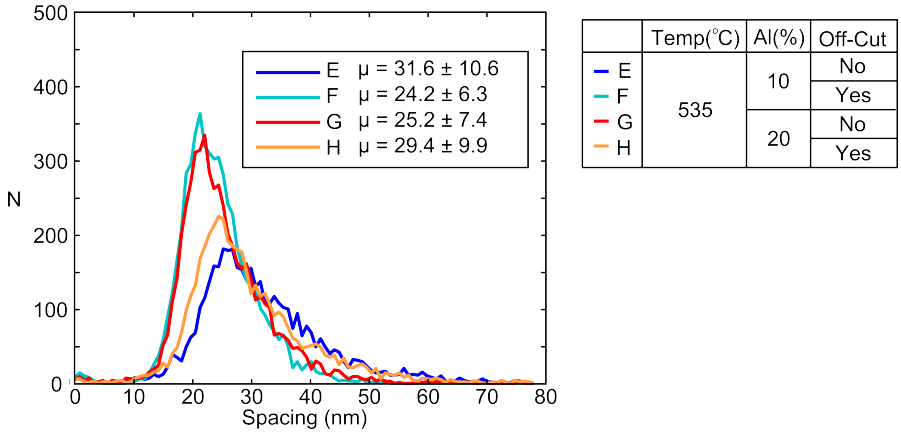

Figure 2.15: Spacing distribution of the wires from samples E through H.

using a Philips CM12 transmission electron microscope. The bright outer regions are InP, the dark band is the two $In_{0.53}Ga_{0.37}Al_{0.10}As$ boundary layers and the bright "dashes" in the center are the cross-sections of quantum wires which run parallel to the viewing direction $(\bar{1}10)$. The change in brightness between the top and the bottom InP layers is mainly due to a slight bend in the samples from the ion milling process. Preferential milling occurs near the edge of the sample near the glue line and effectively erodes it. These intensity variations are a bit more obvious in the lower magnification image of sample F in figure 2.18. In this image the contrast is enhanced[15] to more clearly show all the different deposited layers as well as the vacuum above the sample. Glue is present above the top layer in some samples while not in others depending on sample preparation and in this case it is not.

In all these dark field images we can see that the spacing between the wires is fairly regular although there is clearly some variability. It is important to keep in mind that because we are nearly looking down atomic columns along the direction of the wires, there may be more than one wire within the thickness of the sample at a given 2D position in these images. This is most apparent in figure 2.23 in the next section but may also explain the dark region near the center of the wide wire in the top right corner of figure 2.17. Another important feature to notice in these dark field images is the presence of bright streaks above the quantum wires. Based on the contrast mechanism of dark field imaging using the (002) spot, these

[15] A gamma correction of $\gamma = 1/2$ was applied where the output image intensity is given by $I_{\mathrm{Out}} = I_{\mathrm{In}}^{\gamma}$.

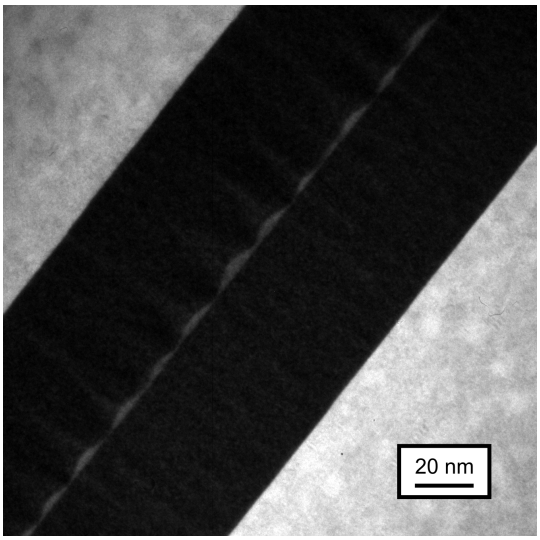

Figure 2.16: Cross-sectional dark field image of sample E using the (002) diffraction spot. This sample was grown on a flat substrate and showed strong wire coalescence on the surface.

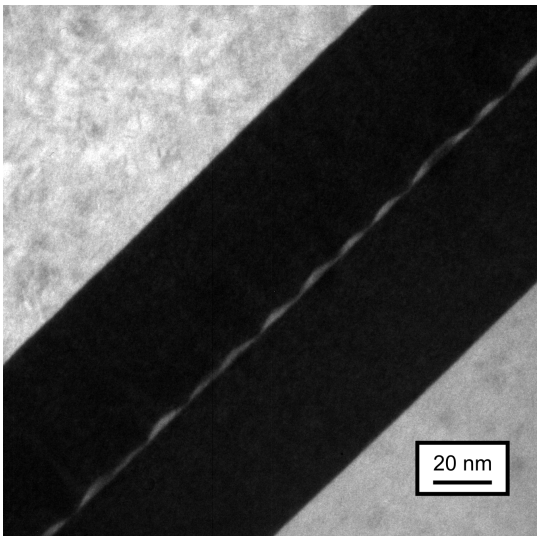

Figure 2.17: Cross-sectional dark field image of sample F using the (002) diffraction spot. This sample was grown on an off-cut substrate and show little to no coalescence on the surface.

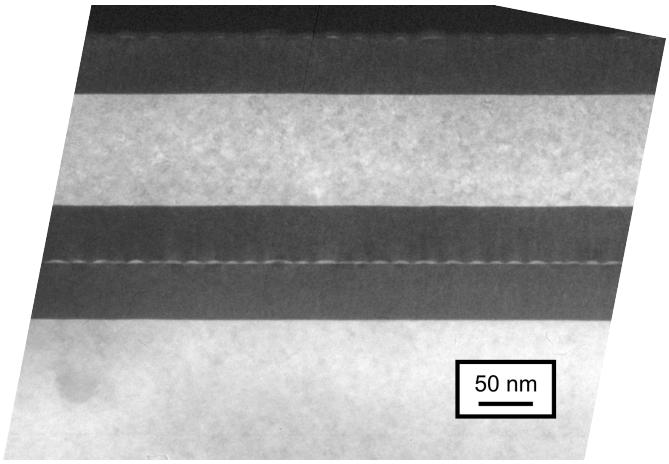

Figure 2.18: A gamma corrected lower magnification (002) dark field image of sample F.(Off-cut, no surface coalescence)

brighter strips indicate a higher concentration of In and other work has confirmed such higher concentrations of In using EELS [21]. These help in the alignment of multilayer (stacked) quantum wires by producing a deposition surface with spatial strain modulations and such modulations are predicted to provide preferential nucleation centers for the lattice-mismatched material [22].

Figures 2.19 and 2.20 show bright field images of the surface of samples E and F

under near zone axis condition which basically just provides strong mass-thickness contrast. Two surfaces are visible in the first image since the glue line was thin enough but not for the second. Some residual glue is present on both samples and appears as light gray. The darker gray layer on all the surfaces is an amorphous layers which was damaged during the ion milling process and the other dark regions are of course the substrates (InGaAlAs and InP). What is important to notice about these images as mentioned in the previous section is that the wires on the surface of sample E are irregular and some flat regions can be seen whereas the surface of sample F has much more regularly shaped wires in correspondence with the SEM results in section 2.4. The fact that this important heterogeneity is observed among the surface wires but not among the buried wires in sample E further supports the idea that the coalescence was likely caused by annealing since the buried wires would have been covered before any significant coalescence could have taken place relative to the surface wires.

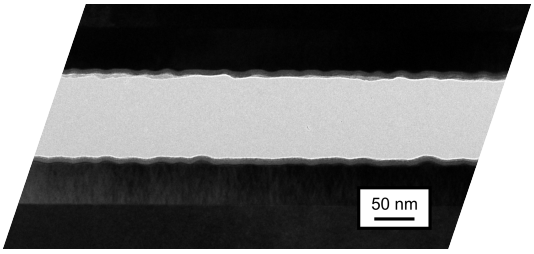

Figure 2.19: Cross-sectional bright field image of sample E near the $(\bar{1}10)$ zone axis. (Flat, strong surface coalescence)

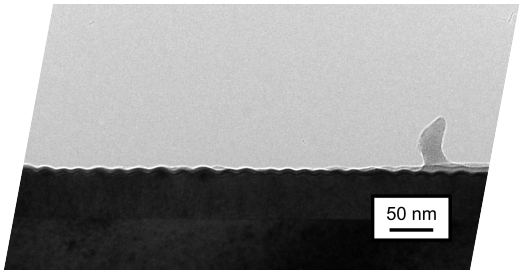

Figure 2.20: Cross-sectional bright field image of sample F near the $(\bar{1}10)$ zone axis. (Off-cut, no surface coalescence)

2.6 HRSTEM Characterization

In order to verify whether the atomic steps[16] act as nucleation centers as intended, high resolution scanning transmission electron microscopy (HRSTEM) was performed on wire samples grown on both nominally flat substrates and off-cut substrates. As mentioned in section 1.4, annular dark field (ADF) images produced using an aberration corrected microscope provides atomic resolution with reasonably intuitive mass-thickness contrast which is ideal for studying (buried) quantum

[16]Recall these are actually diatomic steps.

wires since the main difference between the wire material and its surroundings is its composition. Figures 2.21 and 2.22 show ADF-HRSTEM images of samples E and F which were manually stitched together to cover a large field of view. The images were obtained using an FEI Titan 80-300 STEM and both figures present a single long image which is separated into three parts in order to fit on the page with a reasonable resolution. The arrows indicate where the images are duplicated.

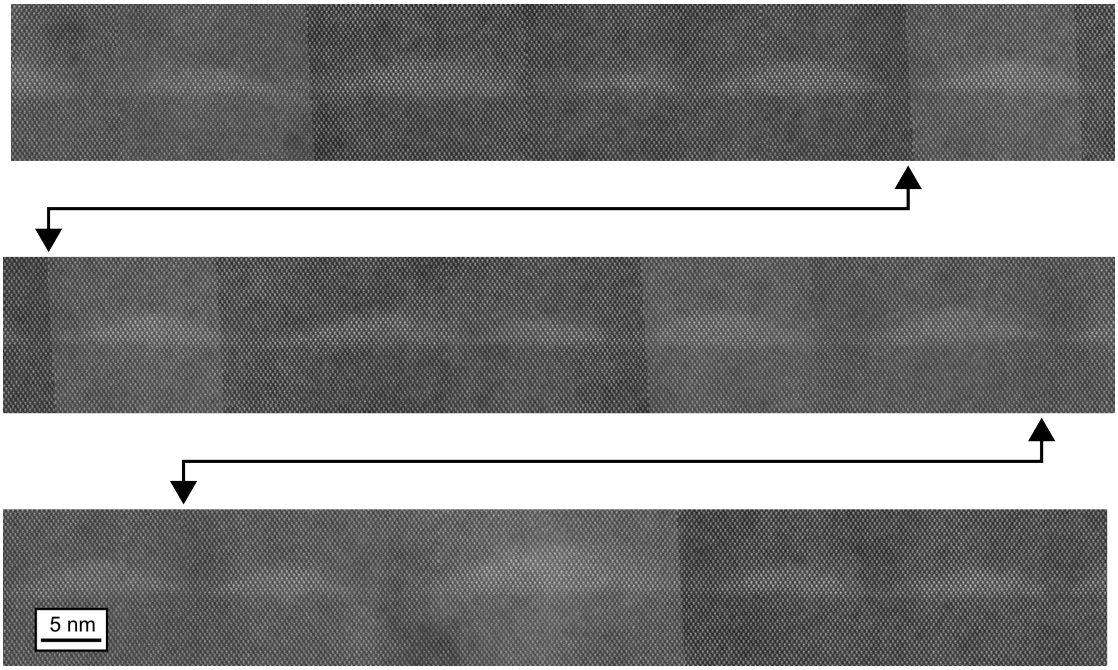

Figure 2.21: ADF-HRSTEM images of sample E stitched together to form a continuous array of wires displayed over three rows. The arrows indicate the duplicated regions. The bottom of the image is aligned with an atomic plane, showing that the substrate was flat.

The first image was stitched together by only translating the 13 images acquired to produce it. Due mainly to drift and possibly to the rotation of the sample between frames[17], there are slight discontinuities clearly visible at the seams between them. The change in overall brightness can be attributed to either the bending of the sample or discrepancies in the adjustment of focus and astigmatism. To some extent it could be attributed to carbon contamination of the sample which is a common problem in high resolution electron microscopy using high current densities although after plasma cleaning, this was not too much of an issue during the acquisition of these micrographs. Unlike in figure 2.21, the image in figure 2.22

[17]The sample was rotated to remain on zone axis and to compensate for the bending of the wedge.

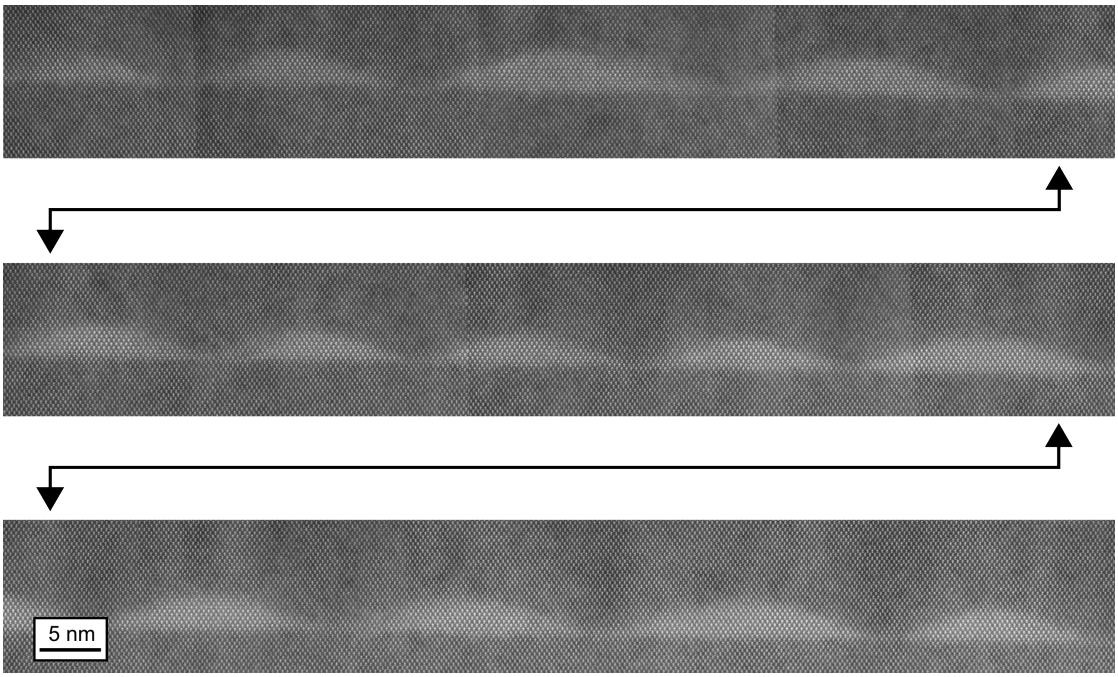

Figure 2.22: ADF-HRSTEM images of sample F stretched, skewed and stitched together to form a continuous array of wires displayed over three rows. The arrows indicate the duplicated regions. The bottom of the image is aligned with an atomic plane, showing the shallow off-cut angle.

was stitched after slightly rotating, stretching and skewing the 12 original images in order to compensate for drift. The greatest amount of stretching applied to any of the original images is around 5%.

The bottom of these panoramic images has been aligned with a single atomic plane (001) in order to reveal the difference between sample E which is grown on a nominally flat substrate and sample F which was grown on a 0.9° off-cut substrate. The wires in the first image are flat whereas the angle measured on the second image is roughly 1.0° as expected. This tilt can be observed by comparing the distance between the bottom of the image and the wire in the top left and bottom right corner of figure 2.22. This means that there are clearly atomic steps distributed somewhere along this long micrograph although finding their exact location has proven difficult. Work by Molina *et al.* [17] has shown that it is possible to find the location of an InP surface step with respect to the location of an InAs wire. Given that the step is straight enough over the thickness of the TEM specimen (along the $(\bar{1}10)$ direction), the contrast between P and As may be strong enough

to determine the exact location of the step given their atomic number difference of $33 - 15 = 18$. In our case however, the contrast that is sought after is between a column of $In_{0.53}Ga_{0.37}Al_{0.10}$ and a column of pure In with an average atomic number difference of only $49 - (49 \cdot 0.53 + 31 \cdot 0.37 + 13 \cdot 0.10) = 49 - 38.7 = 10.3$ since we are looking to distinguish the group III atoms[18].

In a first attempt to identify the location of steps relative to that of the quantum wires, line profiles over atomic planes at the base of the wires in various images were examined in order to distinguish bright columns from darker ones but with no success. Next, principal component analysis (PCA) was applied to each dumbbell in the HRSTEM micrographs by writing another short MATLAB script and the analysis of one image taken from sample F is shown in figures 2.23 through 2.25. PCA applied to images consists of breaking them down from linear combinations of individual pixel intensities into linear combinations of statistical trends of pixel intensities such as shapes, for example. From a linear algebra perspective, it consists of changing the basis or the multi-dimensional unit vectors by solving for the eigenvectors of the problem. What is important to understand for its application here is that it finds statistical trends such as the average intensity profile of the dumbbells and variations between dumbbells in different areas of the image.

Figure 2.23 shows an example of an analyzed image[19]. It is a particularly interesting image since we can see the overlap of two wires on the left side indicated by three distinct regions of different brightness: the dark boundary layer, a large wire-shaped region of intermediate intensity and a bright region at the bottom right of the larger wire. After applying PCA using the MATLAB function `princomp`, the magnitude of the first principle component for each dumbbell is illustrated in figure 2.24. Each circle is located above the center of a detected atomic dumbbell and its brightness represents the magnitude of the first principle component. In order to divide the dumbbells into separate populations, the k-means clustering algorithm was applied using `kmeans` which basically finds linear combinations

[18]This is by no means a thorough comparison of the expected contrast but indicates that the difference should be more subtle.

[19]The wire on the left side of this image is the same as the second wire in the middle row of figure 2.22.

of the principle components which most clearly categorize the distribution of magnitudes. This typically rearranges the principle components into components which are more physically relevant. After applying this clustering, the two distinct populations of dumbbells are presented in figure 2.25 where (one would hope) the white circles indicate In rich columns and the black circles indicate In deficient columns. However, after thorough analysis and parameter adjustments, the location of the atomic steps remains ambiguous and was not possible to be identified relative to the position of the wires.

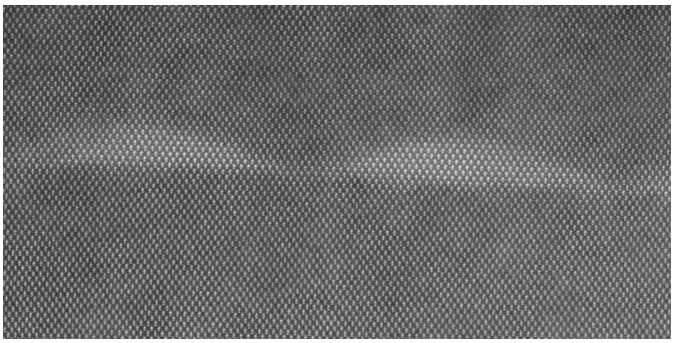

Figure 2.23: HRSTEM cross-sectional image of two quantum wires from sample F. (Off-cut)

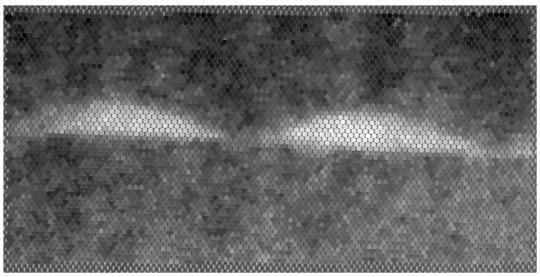

Figure 2.24: Principal component analysis of figure 2.23 showing the magnitude (contribution) of the first principal component of each dumbbell.

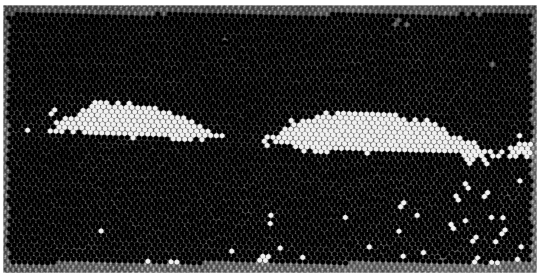

Figure 2.25: Segregation of In rich (white) and In deficient (black) dumbbells using PCA and k-means clustering. No clear step is found.

Chapter 3

Kinetic Monte Carlo

3.1 Overview

The self-assembled quantum wire growth experiments described and analyzed above along with other experiments performed previously [14] give us an idea of the overall effect of growth parameters such as temperature and off-cut angle and are essential to improving growth of quantum structures. However, they give little insight as to how such structures actually form on an atomic level. Due to the high temperature ($> 500°$C) and high vacuum ($\sim 10^{-9}$ Pa) conditions, group V overpressure and rapid growth (~ 1 ML/s) during molecular beam epitaxy (MBE), it is difficult to make any precise measurements during growth to get a good understanding of the formation of the nanoscale structures of interest. Reflection high energy electron diffraction (RHEED) is a technique that can be used to resolve the periodicity of the surface reconstruction which is basically the crystal structure of the surface, different from that of the bulk. Such a measurement gives poor spatial resolution however and is more useful for understanding the overall condition of the substrate surface. Scanning tunneling microscopy (STM) has been performed inside an MBE chamber to study GaAs and InAs [23] with high resolution but this technique requires quenching[1] and therefore requires an interruption in the growth. Despite

[1] Quenching involves cooling a sample rapidly enough as to preserve the structure it had at the high temperature of interest.

not being able to provide a very continuous evolution of epitaxial growth, STM is the technique which likely provides the most detailed view of what happens on the surface during epitaxy.

However, in order to truly get an understanding of how the self-assembly of quantum structures occurs and how growth parameters affect epitaxy on an atomistic scale, we have resorted to computer simulations. The simulation of atomic interactions is a very broad topic and various methods and models have been developed. Density functional theory (DFT) is generally used to calculate the energy of various atomic configuration and the transition energy between different configurations through solving electronic densities (see [8, 24] for examples). Molecular dynamics (MD) is another method which relies on classical dynamics (Newtonian) to calculate the displacement of atoms which usually interact through modeled potentials and van der Waals forces. Both of these computational methods are very detailed but limited to simulating very short time scales (roughly the nanosecond regime) and a fairly modest number of atoms which encompass events such as adatom hopping. For simulating larger length and time scales of thin film epitaxy on the order of seconds, kinetic Monte Carlo (kMC) is a great technique which makes reasonable assumptions about atomic displacements.

The Monte Carlo method is a very general method of predicting the outcome of nearly any stochastic system, that is, a system whose outcome relies on many random events of reasonably well known probabilities. It is somewhat of a brute force method used to simulate such random events rather than calculating an analytic solution of the outcome, usually because a system of interest is very complex. The method was thought of and first put to extensive use by Stanislaw Ulam along with his colleagues near the end of the Second World War [25]. The idea came about while he was ill and playing solitaire. Wanting to know the likelyhood of winning a game of solitaire, he first looked for an analytic solution which would involving finding the outcome of all $8 \cdot 10^{67}$ possibilities. This however proved to be a difficult task and he thought of another way of at least approximating the likelihood of winning which was to play multiple games (shuffling the cards in between of course) and simply to count how many times he won. The principle of using random inputs is the basis of the Monte Carlo method.

The method was then used to predict the outcome of nuclear interaction events. Using a known statistical cross section from neutron scattering experiments and theoretical calculations, the group of scientists at the Los Alamos research laboratory simulated nuclear reactions inside a fissionable material. This consisted of simulating the production of neutrons with a random location, velocity and direction within a volume, and tracking it as it traverses material with a known interaction probability. By simulating the interactions of a large number of particles (neutrons in this example) it is possible to get an understanding of the expected particle flux, energy deposition distribution or nearly any other quantity of interest and the Monte Carlo method is a practical way of performing such calculations for complex problems. The same simulation is simply performed over and over using different random numbers to select which events occur and all the results can be averaged to give a meaningful and statistically significant outcome without having to deal with the complexities of predicting all possible outcomes. For this reason the technique is currently being used in particle physics for predicting the interactions between particles and often complex geometries. With today's fast and accessible computers, the Monte Carlo method is an amazingly convenient tool which can be applied to a wide variety of different problems, such as a game of cards.

Kinetic Monte Carlo specifically deals with the evolution of a single system driven by random events rather than the repeated simulation of the same system to measure multiple possible outcomes. In the context of epitaxy, we can simulate the deposition of adatoms and their diffusion on the substrate surface fairly simply by assuming that they make discrete jumps between surface lattice sites which is fairly accurate based on DFT simulations and observations in HRTEM.

3.2 Surface Diffusion

A kinetic Monte Carlo simulation of adatom diffusion considering strain was developed as part of this work, very closely based on one developed by Schulze and Smereka [26, 27], and thoroughly described by Baskaran [28]. This section

describes the basics of the diffusion model, section 3.3 briefly covers how strain energy is calculated and section 3.4 describes in more detail the anisotropic bond model that was developed for simulating the growth of quantum wires.

The atomistic diffusion model consists of a 3-dimensional cubic lattice of atoms which represents the substrate and the deposited film. More specifically, since III-V semiconductor growth is strictly limited by the deposition and diffusion of the group III atoms, only these are considered. Although this approximation could lead to important problems in simulating InAs grown on InP, only growth of III-As materials are of interest in this work[2] and the effect of the group V atoms can be incorporated into the bonding model.

Each atom on the surface occupies a lattice site and is able to move in four possible directions $(+x, -x, +y, -y)$. The probability of each atom to move depends on, to a first approximation, the number of neighboring atoms which can be between 0 and 4. This probability is expressed by a hopping rate R which is given by an Arrhenius equation (3.1) where R_0 is a base rate, n is the number of nearest neighbors, E_N is the bonding energy between surface atoms[3], E_0 is the activation energy, k_B is the Boltzmann constant and T is the substrate temperature in Kelvin.

$$R = R_0 \exp((nE_N - E_0)/k_B T) \tag{3.1}$$

This is the simplest surface diffusion model and is illustrated in figure 3.1 where the number nearest neighbors is indicated by the different color of the surface atoms. Furthermore only atoms on the surface, that is, those not covered by another atom, can move. This has two implications. The first is that atoms cannot swap positions with each other and atoms can only move to where there is a free space. This means that bulk diffusion is ignored which is a good approximation given the growth temperatures investigated. The second is that no overhanging structures can form. Models including overhangs have been developed to study the formation of dislocations [29] but they are ignored here since our experimental

[2]This is not strictly the case since the deposition of InGaAlAs on InP is required for the barrier layer and is simulated, but it is not by any means the focus of this work.

[3]This should normally be a negative value.

results show no dislocations around the quantum wires. Based on this feature, the model presented in this work is referred to as a solid on solid (SOS) model or even a 2+1 dimensional model since atoms can only move on a surface (2D surface) which extends in a third dimension (+1).

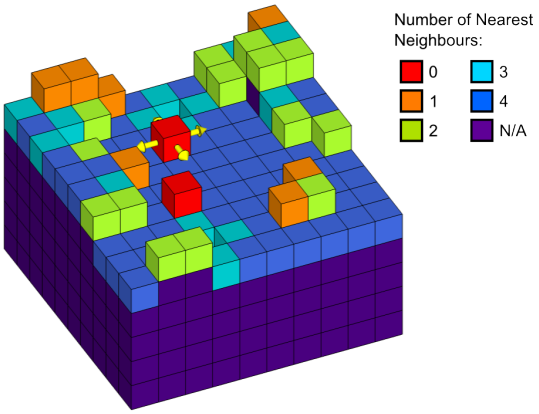

Figure 3.1: Each cube represents a group III atom in the kMC model and its color represents the number of nearest neighbors it has. The atoms in purple are not allowed to move.

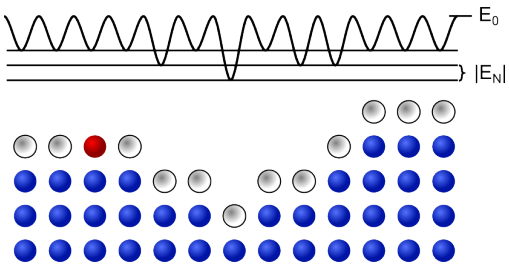

Figure 3.2: Potential energy profile as seen by the red atom.

The variable R_0 physically represents the "attempt frequency" which is how often an atom tries to overcome the activation energy. The exponential term is the likelihood that such an attempt will be successful and this depends on how strongly bonded it is to its current lattice site. This is illustrated by the potential energy profile in figure 3.2. The diagram shows the potential energy of the red atom if it occupied the free white surface states. Here we can clearly see that the potential energy is lower next to atomic steps due to an extra nearest neighbor and even lower in pits since it would then be bonded to two additional atoms in this 1+1D example. Since atoms move more frequently out of higher energy states following equation (3.1), the state occupancy or probability distribution naturally converges towards a Maxwell-Boltzmann distribution. Since the energy of surface atoms decreases when they come next to each other, they tend to agglomerate and this is what leads to the formation of islands, similar to water droplets sticking together.

3.2.1 Selection Algorithm

The way the simulation works is, given the hopping rate of all the surface atoms, a single displacement event (which atom and in which direction) is chosen at random. A rejection-free algorithm is used where the probability of an event being selected is proportional to its hopping rate. An event is selected by first computing a running sum of all the rates $[0, R_1, R_1 + R_2, ..., R_{total}]$, choosing a random value between 0 and R_{total} and determining where it lies among this list as illustrated in figure 3.3. The example shown here is a considerable oversimplification where we assume only three atoms are allowed to move in only one direction. In reality, each surface atom has four separate rates for different directions, although they are generally equal in a model with isotropic diffusion. This algorithm is referred to as rejection-free since every selected event leads to the displacement of an atom. This is different from earlier algorithms where a lattice site was chosen at random and whether the selected atom moved or not depended on its hopping rate. This algorithm was considerably slower than its rejection-free successor.

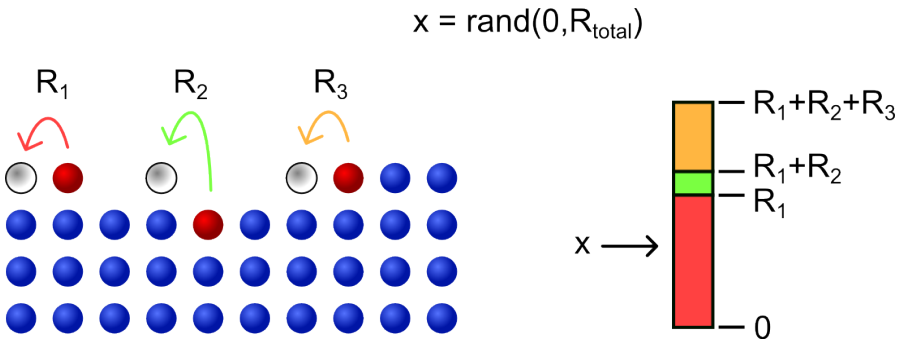

Figure 3.3: An event is selected at random among three possibilities.

Nonetheless, it is important to understand how time consuming this searching process can be if it is not executed efficiently. For a 120 by 120 lattice of atoms, this list contains $120 \cdot 120 \cdot 4 = 57600$ elements and verifying this many inequalities (is $x > R_n$?) would result in an impractically slow kMC simulation. For this reason, a binary tree structure based on the AVL tree named after its inventors Adelson-Velski and Landis[30] was implemented and is described in appendix A. This reduces the search time from $O(N)$ to $O(\log_2(N))$ which is a dramatic improvement. For every simulation step, the simulation clock (total growth cumulative growth time)

should be advanced by an exponentially distributed random number with a mean of $1/R_{total}$ using equation (3.2). However, for simplicity and since only the overall time distribution is of interest, our implementation only uses the mean ($1/R_{total}$) as a time step.

$$\Delta t = \frac{-1}{R_{total}} \ln(x) \tag{3.2}$$

$$x = \text{rand}(0, 1) \tag{3.3}$$

The mean of $1/R_{total}$ can be understood through simple examples. If only one atom could move and had a hopping rate of $R_1 = 1$ Hz, the average time between steps would be 1 second ($\frac{1}{1\text{Hz}}$). If two atoms had this same hopping rate, the average time between steps would be halfed or $\frac{1}{(2 \cdot R_1)} = \frac{1}{2\text{Hz}} = 0.5$ s since the total event rate is now 2 Hz. Finally, if one atom has a hopping rate of $R_1 = 3$ Hz and the other $R_2 = 1$ Hz, the total hopping frequency is 4 Hz and therefore the average time between events is 0.25 s. Then in the general case, all the rates must be added together as indicated in the equation above.

The algorithm therefore consists of first calculating the hopping rate of all the surface atoms and adding them to the tree structure. After this initialization, an event is selected randomly, the appropriate atom is displaced and the rates of the surrounding atoms are updated. The displaced atom may have broken bonds and made new ones which means that the rates of all the adjacent atoms must be updated, including the newly covered and uncovered atom. This process is repeated until the desired time has been reached. Additionally, a deposition rate is added to the running sum. This is the rate at which atoms are deposited on the surface during growth and is expressed by equation (3.4) where R_{ML} is the deposition rate in ML/s and N_x and N_y are the dimensions of the simulated substrate surface in atoms. The deposition of a new atom is naturally also one of the possible events.

$$R_{dep} = N_x N_y R_{\text{ML}} \tag{3.4}$$

3.3 Strain Calculation

Since strain energy is what drives the formation of 3-dimensional islands, its inclusion in the kMC model is crucial. This is done by including an additional strain energy term E_S to equation (3.1). The improved rate model is shown in equation (3.5). One of the earliest implementation of a strain energy term in a 2+1 dimensional model[31] uses a simplification where only atoms at the edge of (2D) islands are affected by strain based on conclusions drawn from finite element strain calculations. Full strain calculations in a 1+1 dimensional model were performed in order to theoretically demonstrate how strain relaxation can occur without dislocations[32] but due to limitations in computing power and perhaps more importantly, computer memory, this was very difficult to do in 2+1 dimensions. With the incredible developments in computer technology over the past couple decades, it is now possible to undertake such problems as demonstrated by Schulze and Smereka. In this work, the value E_S is therefore calculated based on full strain calculations performed over the cubic lattice of simulated atoms.

$$R = R_0 \exp((nE_N + E_S - E_0)/k_bT) \tag{3.5}$$

3.3.1 Strain Equation

Considering strain involves finding the equilibrium position of all the atoms in the simulated lattice by numerically solving the differential equations that arise from stress and strain. Before presenting the ball and spring model that is used in our simulations, the differential equations of interest are derived in this section to justify its validity. It is first worth defining some of the variables as well as the convention that will be used here. Cartesian coordinates are used for obvious reasons and the three orthogonal axes are x, y and z, and their respective unit vectors are $\hat{x}$, $\hat{y}$ and $\hat{z}$. Displacements in these directions are given by the variables U, V and W. The variable used for strain is ϵ and that for stress is σ.

The main governing equation of stress and strain under equilibrium is Cauchy's first law of motion (3.6) [33] (balance of linear momentum) where ρ is mass density,

$\vec{v}$ is velocity, t is time, $\vec{\nabla}$ is the divergence operator, $\boldsymbol{\sigma}$ is the stress tensor and $\vec{F}$ is an external force density [N/m^3]. This is analogous to Newton's second law of motion ($\vec{F} = m\vec{a}$) but in a continuous case. Under equilibrium, the acceleration is zero which means we only need to solve equation (3.7) which is time-independent. The external force density $\vec{F}$ in our case will be related to the lattice mismatch between different materials.

$$\vec{\nabla} \cdot \boldsymbol{\sigma} + \vec{F} = \rho \frac{d\vec{v}}{dt} \tag{3.6}$$

$$\vec{\nabla} \cdot \boldsymbol{\sigma} + \vec{F} = 0 \tag{3.7}$$

The stress tensor is defined in equation (3.8) which is equivalent to equation (3.9)[4] since $\boldsymbol{\sigma} = \boldsymbol{\sigma}^\top$ due to the balance of angular momentum (Cauchy's second law of motion).

$$\boldsymbol{\sigma} = \begin{bmatrix} \sigma_{xx} & \sigma_{xy} & \sigma_{xz} \\ \sigma_{yx} & \sigma_{yy} & \sigma_{yz} \\ \sigma_{zx} & \sigma_{zy} & \sigma_{zz} \end{bmatrix} \tag{3.8}$$

$$\boldsymbol{\sigma} = \begin{bmatrix} \sigma_{xx} & \sigma_{xy} & \sigma_{xz} \\ \sigma_{xy} & \sigma_{yy} & \sigma_{yz} \\ \sigma_{xz} & \sigma_{yz} & \sigma_{zz} \end{bmatrix} \tag{3.9}$$

In turn, its elements are related to strain by the matrix equation (3.10). Due to the fact that the zinc blende crystal structure is cubic and has a F$\bar{4}$3m space group, the x, y and z directions are equivalent and so only three elastic constants, C_{11}, C_{12} and C_{44} are necessary. The stress strain relationship can therefore be simplified to equation (3.11).

[4]The use of xz over zx may not be entirely consistent throughout this section but it is of no importance since they are both equivalent.

$$\boldsymbol{\sigma} = \begin{bmatrix} \sigma_{xx} \\ \sigma_{yy} \\ \sigma_{zz} \\ \sigma_{yz} \\ \sigma_{zx} \\ \sigma_{xy} \end{bmatrix} = \begin{bmatrix} C_{11} & C_{12} & C_{13} & 0 & 0 & 0 \\ C_{21} & C_{22} & C_{23} & 0 & 0 & 0 \\ C_{31} & C_{32} & C_{33} & 0 & 0 & 0 \\ 0 & 0 & 0 & C_{44} & 0 & 0 \\ 0 & 0 & 0 & 0 & C_{55} & 0 \\ 0 & 0 & 0 & 0 & 0 & C_{66} \end{bmatrix} \begin{bmatrix} \epsilon_{xx} \\ \epsilon_{yy} \\ \epsilon_{zz} \\ \epsilon_{yz} \\ \epsilon_{zx} \\ \epsilon_{xy} \end{bmatrix} \tag{3.10}$$

$$\boldsymbol{\sigma} = \begin{bmatrix} \sigma_{xx} \\ \sigma_{yy} \\ \sigma_{zz} \\ \sigma_{yz} \\ \sigma_{zx} \\ \sigma_{xy} \end{bmatrix} = \begin{bmatrix} C_{11} & C_{12} & C_{12} & 0 & 0 & 0 \\ C_{12} & C_{11} & C_{12} & 0 & 0 & 0 \\ C_{12} & C_{12} & C_{11} & 0 & 0 & 0 \\ 0 & 0 & 0 & C_{44} & 0 & 0 \\ 0 & 0 & 0 & 0 & C_{44} & 0 \\ 0 & 0 & 0 & 0 & 0 & C_{44} \end{bmatrix} \begin{bmatrix} \epsilon_{xx} \\ \epsilon_{yy} \\ \epsilon_{zz} \\ \epsilon_{yz} \\ \epsilon_{zx} \\ \epsilon_{xy} \end{bmatrix} \tag{3.11}$$

Next, we define $\vec{\nabla}$ in (3.12) and apply it to the stress tensor. The result is the three partial differential equations in (3.13) through (3.15) where F_x, F_y and F_z are the three components the of external force density $\vec{F}$.

$$\vec{\nabla} = \begin{bmatrix} \frac{\partial}{\partial x} & \frac{\partial}{\partial y} & \frac{\partial}{\partial z} \end{bmatrix} \tag{3.12}$$

$$C_{11}\frac{\partial \epsilon_{xx}}{\partial x} + C_{12}\frac{\partial \epsilon_{yy}}{\partial x} + C_{12}\frac{\partial \epsilon_{zz}}{\partial x} + C_{44}\frac{\partial \epsilon_{xy}}{\partial y} + C_{44}\frac{\partial \epsilon_{zx}}{\partial z} + F_x = 0 \tag{3.13}$$

$$C_{11}\frac{\partial \epsilon_{yy}}{\partial y} + C_{12}\frac{\partial \epsilon_{zz}}{\partial y} + C_{12}\frac{\partial \epsilon_{xx}}{\partial y} + C_{44}\frac{\partial \epsilon_{yz}}{\partial z} + C_{44}\frac{\partial \epsilon_{xy}}{\partial x} + F_y = 0 \tag{3.14}$$

$$C_{11}\frac{\partial \epsilon_{zz}}{\partial z} + C_{12}\frac{\partial \epsilon_{xx}}{\partial z} + C_{12}\frac{\partial \epsilon_{yy}}{\partial z} + C_{44}\frac{\partial \epsilon_{zx}}{\partial x} + C_{44}\frac{\partial \epsilon_{yz}}{\partial y} + F_z = 0 \tag{3.15}$$

This however does not give us an expression in terms of atomic displacements. Equations (3.16) and (3.17) define normal and shear strain with respect to displacement. From here, we can obtain all three differential equations required to solve strain in equilibrium by substituting these expression in the equations above. Equation (3.18) shows the result in the x direction, and the expressions in y and z are similar.

$$\epsilon_{xx} = \frac{\partial U}{\partial x}; \quad \epsilon_{yy} = \frac{\partial V}{\partial y}; \quad \epsilon_{zz} = \frac{\partial W}{\partial z} \tag{3.16}$$

$$\epsilon_{xy} = \frac{1}{2}\left(\frac{\partial U}{\partial y} + \frac{\partial V}{\partial x}\right); \quad \epsilon_{yz} = \frac{1}{2}\left(\frac{\partial V}{\partial z} + \frac{\partial W}{\partial y}\right); \quad \epsilon_{zx} = \frac{1}{2}\left(\frac{\partial W}{\partial x} + \frac{\partial U}{\partial z}\right) \tag{3.17}$$

$$C_{11}\frac{\partial^2 U}{\partial x^2} + C_{12}\frac{\partial^2 V}{\partial x \partial y} + C_{12}\frac{\partial^2 W}{\partial x \partial z} + \frac{C_{44}}{2}\left(\frac{\partial^2 U}{\partial y^2} + \frac{\partial^2 V}{\partial y \partial x}\right) + \frac{C_{44}}{2}\left(\frac{\partial^2 U}{\partial z^2} + \frac{\partial W}{\partial z \partial x}\right) + F_x = 0 \tag{3.18}$$

In order to apply this analytic equation to a discrete lattice of points such as the one in our kMC model, it must be converted into a numerical equation which can then be solved using an algorithm. For this we require a numerical expression for derivatives which can be obtained from the definition of a derivative. Three useful definitions are given in equations (3.19) through (3.21). The third is exactly equal to the slope of a quadratic spline fit to three points[5]. Not only is it a more accurate estimate but it is also symmetric which is a good feature for numerically solving equations. Using these definitions, we can also express two important second derivatives as demonstrated in (3.22) and (3.23).

$$\frac{df}{dx} = \frac{f(x+\Delta x) - f(x)}{\Delta x} \tag{3.19}$$

$$\text{or} \quad = \frac{f(x) - f(x-\Delta x)}{\Delta x} \tag{3.20}$$

$$\text{or} \quad = \frac{f(x+\Delta x) - f(x-\Delta x)}{2\Delta x} \tag{3.21}$$

$$\frac{d^2 f}{dx^2} = \frac{d}{dx}\frac{df}{dx} = \frac{\frac{df}{dx}|_x - \frac{df}{dx}|_{x-\Delta x}}{\Delta x} \tag{3.22}$$

$$= \frac{\dfrac{f(x+\Delta x) - f(x)}{\Delta x} - \dfrac{f(x) - f(x-\Delta x)}{\Delta x}}{\Delta x}$$

$$= \frac{f(x+\Delta x) + f(x-\Delta x) - 2f(x)}{\Delta x^2}$$

[5]The derivative of a second order spline fitted to the three points, $f(x_0 - \Delta x)$, $f(x_0)$ and $f(x_0 + \Delta x)$, evaluated at x_0, $df(x)/dx|_{x_0}$, is equal to this expression

$$\frac{d^2 f}{dxdy} = \frac{d}{dx}\frac{df}{dy} = \frac{\frac{df}{dy}|_{x+\Delta x} - \frac{df}{dy}|_{x-\Delta x}}{2\Delta x} \tag{3.23}$$

$$= \frac{\dfrac{f(x+\Delta x, y+\Delta y) - f(x+\Delta x, y-\Delta y)}{2\Delta y} - \dfrac{f(x-\Delta x, y+\Delta y) - f(x-\Delta x, y-\Delta y)}{2\Delta y}}{2\Delta x}$$

$$= \frac{f(x+\Delta x, y+\Delta y) + f(x-\Delta x, y-\Delta y) - f(x+\Delta x, y-\Delta y) - f(x-\Delta x, y+\Delta y)}{4\Delta x \Delta y}$$

$$= \frac{f(+,+) + f(-,-) - f(+,-) - f(-,+)}{4\Delta x \Delta y} \tag{3.24}$$

$$= \frac{f\binom{+,+}{-,-} - f\binom{+,-}{-,+}}{4\Delta x \Delta y} \tag{3.25}$$

Since all these numerical expression will be applied to a regular grid with even spacing between all points, Δx will always represent the same distance, that is the grid spacing in x, and this applies also for Δy and Δz. Additionally for compactness and readability, equation (3.25) introduces a compact notation that will be used in this section which is equivalent to equations (3.24) and (3.23). As a more general example, the expression in (3.26) is equivalent to that in (3.27). This is nothing but a shorthand notation for convenience.

$$f(x+\Delta x, y, z-\Delta z) + f(x-\Delta x, y+\Delta y, z) \tag{3.26}$$

$$= f\binom{+,0,-}{-,+,0} \tag{3.27}$$

All that is left to do now is to make the appropriate substitutions in equation (3.18) as shown in (3.28).

$$\begin{aligned}
&\frac{C_{11}}{\Delta x^2}\left(U\left(\substack{+,0,0\\-,0,0}\right) - 2U(0,0,0)\right) \\
&+\frac{C_{12}}{4\Delta x\Delta y}\left(V\left(\substack{+,+,0\\-,-,0}\right) - V\left(\substack{+,-,0\\-,+,0}\right)\right) + \frac{C_{12}}{4\Delta x\Delta z}\left(W\left(\substack{+,0,+\\-,0,-}\right) - W\left(\substack{+,0,-\\-,0,+}\right)\right) \\
&+\frac{C_{44}}{2}\left[\frac{1}{\Delta y^2}\left(U\left(\substack{0,+,0\\0,-,0}\right) - 2U(0,0,0)\right) + \frac{1}{4\Delta x\Delta y}\left(V\left(\substack{+,+,0\\-,-,0}\right) - V\left(\substack{+,-,0\\-,+,0}\right)\right)\right] \\
&+\frac{C_{44}}{2}\left[\frac{1}{\Delta z^2}\left(U\left(\substack{0,0,+\\0,0,-}\right) - 2U(0,0,0)\right) + \frac{1}{4\Delta x\Delta y}\left(W\left(\substack{+,0,+\\-,0,-}\right) - W\left(\substack{+,0,-\\-,0,+}\right)\right)\right] \\
&+F_x = 0
\end{aligned} \tag{3.28}$$

This is the numerical differential equation which corresponds to Cauchy's first law of motion (3.7) under equilibrium. Interestingly all these terms can be expanded into displacement differences of the form $U_n(\pm,\pm,\pm) - U_n(0,0,0)$. Note that $+2V(0,0,0) - 2V(0,0,0)$ can be added to the first term of the second line and so on. In this case, the whole equation can be interpreted as a balance of springs between neighboring atoms. Their influence on each other is illustrated in figure 3.4. The middle diagram shows how the center atom moves to the right if its first nearest neighbors move to the right. The rightmost diagram shows how it moves to the right based on the vertical displacement of its second nearest neighbours. Furthermore, the reciprocal case is also true. Since all the atoms affect each other in order to come to equilibrium, a displacement of the center atom to the right will affect its neighboring atoms in the same way illustrated here. Although only the balance in x is considered here and is only illustrated in 2 dimensions, the same applies in all directions.

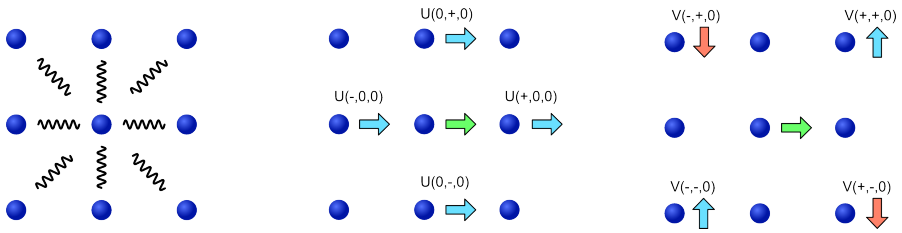

Figure 3.4: A schematic illustration of atoms bound by springs. The two diagrams on the right show how the x-displacement U is affected by the displacement in x and y, U and V, of its neighboring atoms.

Next, we consider how equation (3.28) is used to implement a lattice mismatch.

This is where F_x comes in. Firstly, since displacement is a value relative in translation, the value of every element of the displacement field $U(x, y, z)$ in equilibrium is set to 0 for simplicity as opposed to having $U(i, j, k) = i * \Delta x$ where i, j and k are the indices of the discrete strain field. In our case, this represents the relaxed InP lattice or another lattice-matched material and the equilibrium distance between atoms is then 0 by default.

Lattice mismatch is introduced by setting the equilibrium distance between certain atoms to be a value other than 0 such as $0.032\Delta x$ in the case of InAs since the lattice mismatch between it and InP is 3.2%. This lattice mismatch term is added to the value of every displacement difference (of the form $U(\pm) - U(0)$). At this point, it is also possible to use a normalized system where U is a unitless displacement field which is relative in magnitude. This is achieved by replacing U by $U\Delta x$, V by $V\Delta y$ and W by $W\Delta z$. As an example in one dimension, if an atom on the left $(x - \Delta x)$ was larger as illustrated below, equation (3.28) would become equation (3.29) where mf is the relative mismatch between the middle and left atoms and the extra Δx term comes from the use of a normalized displacement field.

$$\frac{C_{11}}{\Delta x^2}\Delta x\Big(U(x+\Delta x) - U(x) + (U(x-\Delta x) - U(x) - mf)\Big) = 0 \tag{3.29}$$

This leads to a displacement towards the right as indicated by the figure above. The value of F_x here is therefore $\frac{C_{11}}{\Delta x}mf$. Since the reference lattice is InP, InP "atoms" have a misfit or minimum energy separation of 0 and InAs "atoms" have a separation of 0.032. As an approximation, the relaxed distance between InP and InAs "atoms" is the average of these two values. The value used for mf is therefore given by equation (3.30) where A and B are the two neighboring atoms or compounds and a is the respective lattice constant.

$$mf(A, B) = \frac{1}{2}\left(\frac{a_A - a_{InP}}{a_{InP}} + \frac{a_B - a_{InP}}{a_{InP}}\right) \tag{3.30}$$

3.3.2 Spring Model

For reasons of numerical stability, a different spring model from the one developed above was implemented in the strain calculation portion of the kMC simulation. The implementation in this work follows that of Schulze and Smereka. It consists of Hookean springs between nearest neighbors with two spring constants, k_1 and k_2. Similar to the above model, it is illustrated in figure 3.5 and defined in equation (3.31).

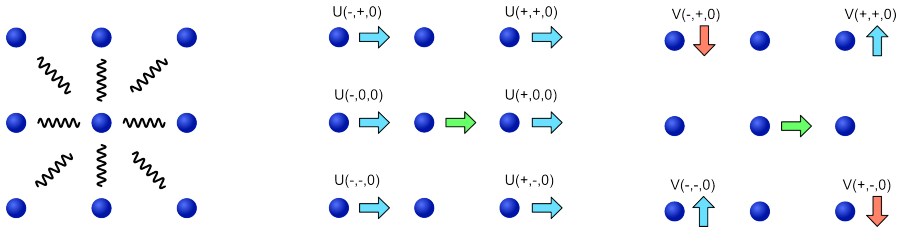

Figure 3.5: A schematic illustration similar to 3.4 but of the implemented spring model. The only different is how the displacement of the center atom is affected by its second nearest neighbors in the middle diagram.

$$
\begin{aligned}
& k_1\left(U\left(\begin{smallmatrix}+,0,0\\-,0,0\end{smallmatrix}\right)-2U(0,0,0)\right) \\
+k_2\left(V\left(\begin{smallmatrix}+,+,0\\-,-,0\end{smallmatrix}\right)-V\left(\begin{smallmatrix}+,-,0\\-,+,0\end{smallmatrix}\right)\right)&+k_2\left(W\left(\begin{smallmatrix}+,0,+\\-,0,-\end{smallmatrix}\right)-W\left(\begin{smallmatrix}+,0,-\\-,0,+\end{smallmatrix}\right)\right) \\
& +k_2'\left[U\left(\begin{smallmatrix}+,+,0\\+,-,0\end{smallmatrix}\right)+U\left(\begin{smallmatrix}-,+,0\\-,-,0\end{smallmatrix}\right)-4U(0,0,0)\right] \\
& +k_2'\left[U\left(\begin{smallmatrix}+,0,+\\+,0,-\end{smallmatrix}\right)+U\left(\begin{smallmatrix}-,0,+\\-,0,-\end{smallmatrix}\right)-4U(0,0,0)\right] \\
& +F_x=0
\end{aligned}
\tag{3.31}
$$

Under particular conditions, this simplified model is equivalent to the previous one. The first condition is that the spacing in all dimensions is equal, that is, $\Delta x = \Delta y = \Delta z$. This is the case for a cubic lattice. By applying the substitutions in (3.32), (3.33) and (3.34), both equations (3.28) and (3.31) work out to be equivalent. These approximations basically redistribute the influence of strain among the nearest and second nearest neighbors. The first approximation simply assumes that the displacement in x of the atom above the center one $(y + \Delta y)$ is the average displacement in x of the two top corner atoms and the same is done for the bottom corners. The approximation in (3.33) is similar but in the z direction. The third is more of a fine adjustment where the displacement in x of the neighbor

to the right $(x + \Delta x)$ is replaced by a weighted average of the displacement of this neighbor and the four second nearest neighbors to the right. The same is done for the left neighbor, hence the $U(-, 0, 0)$ term.

$$U\binom{0,+,0}{0,-,0} \approx \frac{1}{2}\left[U\binom{+,+,0}{+,-,0} + U\binom{-,+,0}{-,-,0}\right] \tag{3.32}$$

$$U\binom{0,0,+}{0,0,-} \approx \frac{1}{2}\left[U\binom{+,0,+}{+,0,-} + U\binom{-,0,+}{-,0,-}\right] \tag{3.33}$$

$$U\binom{+,0,0}{-,0,0} \approx \frac{3}{4}U\binom{+,0,0}{-,0,0} + \frac{1}{8}\left[\frac{U\binom{+,+,0}{-,+,0} + U\binom{+,-,0}{-,-,0}}{2}\right] + \frac{1}{8}\left[\frac{U\binom{+,0,+}{-,0,+} + U\binom{+,0,-}{-,0,-}}{2}\right] \tag{3.34}$$

Under the second condition that $C_{12} = C_{44}$, k_2 and k_2' are the same given the substitutions made above. This is a reasonable condition since $C_{12} = 0.350$ eV/Å^3; $C_{44} = 0.285$ eV/Å^3 for InP and $C_{12} = 0.283$ eV/Å^3; $C_{44} = 0.247$ eV/Å^3 for InAs. Additionally, using the approximation $C_{11} \approx 2C_{12}$ ($C_{11} = 0.631$ eV/Å^3 for InP and $C_{11} = 0.521$ eV/Å^3 for InAs), the two spring constants in our model are related by $k_2 = k_1/4$, making the straight springs 4 times as rigid as the diagonal ones.

The strain fields are then solved using the successive over-relaxation method which can be demonstrated with a simple example. If we consider the 1-dimensional case of the strain equation with no lattice mismatch, equation (3.31) is essentially Laplace's equation (3.35). The numerical solution can be determined by iteratively solving this equation which is of the form in (3.37) where R is the residue, A is the coefficient and x is the variable of interest. The value of x is therefore updated to a newer value x^+ using equation (3.38) and this is repeated multiple times over the different elements of the strain field.

$$\frac{\partial^2 U}{\partial x^2} = 0 \tag{3.35}$$

$$U\binom{+}{-} - 2U(0) = 0 \tag{3.36}$$

$$R + Ax = 0 \tag{3.37}$$

$$x^+ = x - wR/A \tag{3.38}$$

The variable w is a weighting factor called the over-relaxation factor. This value must be greater than 1 in order for the solution to converge faster but must be less

than 2 otherwise it diverges. The optimal value depends strongly on the problem it is applied to and the size of the array being relaxed. In our implementation a value of 1.75 was found to be optimal when solving over the whole lattice and 1.5 when applied to a 3x3x3 subset. Figure 3.6 illustrates the successive over-relaxation method with $w = 1.5$ and how it converges more quickly than the regular successive relaxation method where $w = 1$. The boundary conditions are the fixed red points and the blue points are the value of the quantity x at different indices i. The diagonal line is the exact solution.

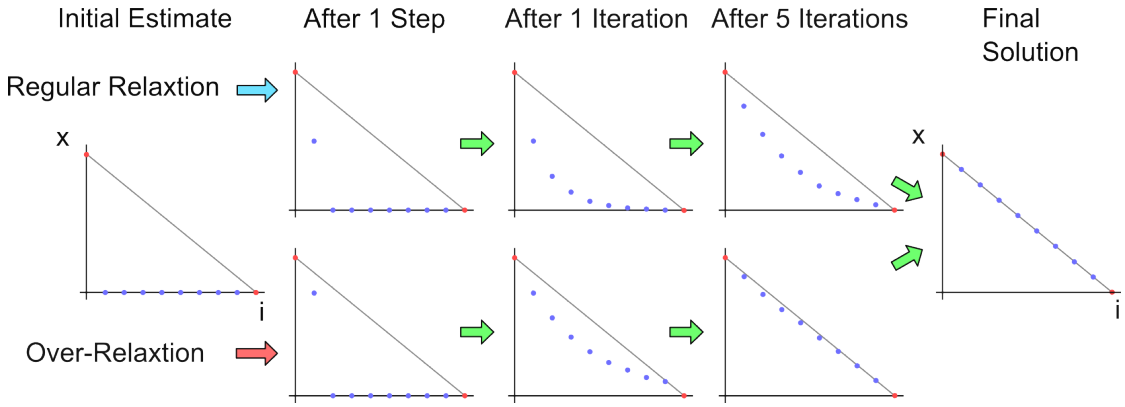

Figure 3.6: Comparison between the regular successive relaxation method and the successive over-relaxation method which converges to the final solution more quickly.

The case of strain in 3 dimensions is obviously more complicated than the 1D case in that it involves more terms, but the algorithm remains just as simple. Whereas the residual for the displacement in x (U) is made up of only two terms in equation (3.29), the 3-dimensional case requires 18 terms as indicated by equation (3.31), that is, the displacement in x of an atom is influenced by the displacement in x of 2 first nearest neighbors, 8 second nearest neighbors and the displacements in y and z of these same 8 second nearest neighbors. Solving the strain fields U, V and W in a 3D lattice therefore requires up to 54 calculations for each lattice point depending on the free lattice sites at the surface. If a vacancy is present next to an atom, the difference term ($k_2U(+,+,0) - k_2U(0,0,0)$ for example) for this vacancy is not added to the residual R nor is $-k_2$ added to the coefficient A. Additionally, it should be noted that for the solution to properly converge, the coefficient A is incremented by twice the spring constant ($-2k_2$) for second nearest neighbors. Without this factor of 2 which effectively acts as an under-relaxation constant, the solution would not converge at corers of the strain field.

Once the equilibrium positions have been determined (within a defined residual error), the elastic strain energy is calculated using the square of all the difference terms based on Hooke's law. From the 1-dimensional example (3.29), we get the strain energy E_S in equation (3.39). Since this energy is the result of the integral of the force in x as seen in Hooke's law (3.42), the Δx in the denominator of (3.29) cancels out and the factor of 1/2 appears. Since all the above equations deal with force densities, an additional factor of v is required to compute the energy rather than the energy density where v is the volume of the simulated "cell". In this case, v is given by equation (3.40) where a is the lattice constant of InP and the factor of 1/4 comes from the fact that there are 4 group III atoms per unit cell. Finally, the spring constants k_1 and k_2 for the different materials are given by equation 3.43 where C_{11} is the stiffness constant of the material of interest and v remains a quarter of the InP unit cell since the strain fields are normalized to InP. Based on the values of C_{11} found in [18], the values of k_1 for InP, InAs, GaAs and AlAs are 23.9, 19.7, 28.1 and 28.4 eV.

$$E_S = \frac{C_{11}v}{2}\Big[\Big(U(x+\Delta) - U(x)\Big)^2 + \Big(U(x-\Delta x) - mf\Big)^2\Big] \tag{3.39}$$

$$v = \frac{a_{\text{InP}}^3}{4} \tag{3.40}$$

$$F_{\text{Hooke}} = kx \tag{3.41}$$

$$E_{\text{Hooke}} = \frac{k}{2}x^2 \tag{3.42}$$

$$k_1 = 4k_2 = \frac{3vC_{11}}{4} = \frac{3a_{\text{InP}}^3 C_{11}}{16} \tag{3.43}$$

This completes the kinetic Monte Carlo algorithm that is used to simulate epitaxial deposition, surface diffusion and ultimately the formation of quantum structures through strain relief. The step by step algorithm is as follows.

Initialization:

- Initalize constants such as bond strengths and elastic constants.
- Create an initial unstrained substrate which is usually either flat or made of surface steps. This is a 3-dimensional lattice of integers representing group III atomic species or vacuum.

- Initialize the hopping rates of all atoms to 0 (by creating the tree structure described in appendix A).
- Create displacement fields U, V and W, and set them to 0.
- Relax the substrate by solving the strain equations described in this chapter.
- Update the hopping rate for all surface atoms based on the number of nearest neighbors and their local strain energy.

For every simulation step:

- Select an event randomly, based on hopping rates using the efficient binary tree structure. This includes the deposition of a new atom.
- Increase the simulation time by $1/R_{total}$.
- Move the selected atom or add a new atom to a random position on the surface.
- Locally update strain around the atom.
- Every $\sim$1000 events, update strain globally using the expanding box method (see section 3.5.3).
- Update the rates of atoms near the event.

This is repeated until either the thin film deposition is complete or the desired annealing time has passed.

3.4 Bond Model

Although the algorithm above has been developed and used by other researchers, what distinguishes our model is its application to the problem of understanding InAs quantum wire growth as opposed to other heteoepitaxial systems such as Ge on Si.

The most important difference lies in the fact that we are investigating the growth of III-V semiconductors rather than Si or Ge which has two major implications. The first is that since only the group III atoms are considered when modeling diffusion, we represent a unit cell using 4 atoms instead of 8 in the case of elemental semiconductors. The second relates to anisotropy. As illustrated in chapter 2, surface steps on compound semiconductors are diatomic instead of monatomic in the case of elemental semiconductors. Because of this, the dangling bonds of the group V atoms are in the same direction on every terrace whereas the dangling bonds of group IV atoms alternate direction between each atomic terrace. This arrangement is illustrated in figure 3.7 where the black lines indicated the direction of dangling bonds.

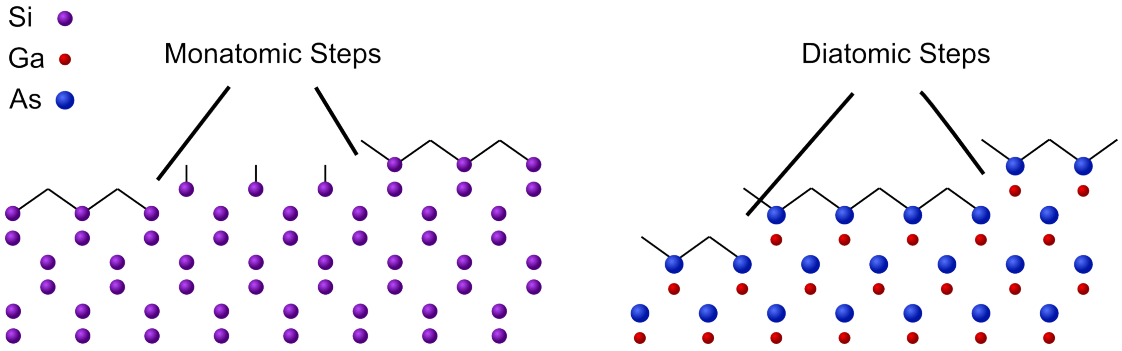

Figure 3.7: Schematic illustration of how the presence of diatomic steps leads to a global bonding anisotropy on the surface of III-V semiconductors.

This leads to a global anisotropy on the (001) surface of III-V semiconductors not present in the case of elemental semiconductors where the anisotropy alternates from terrace to terrace. The effect of this can be clearly observed using scanning tunneling microscopy on vicinal Si(100) substrates where step edges alternate between smooth and rough [34]. On the other hand in the case of III-V semiconductors, it is well known that the anisotropic surface reconstruction produces faster diffusion in the $(\bar{1}10)$ direction than the (110) direction [35] although as discussed in section 3.6.1, this does not explain the preference of wire formation along the $(\bar{1}10)$ direction. However the surface reconstruction must somehow be responsible for this alignment.

Knowing that anisotropy plays a key role in the formation of quantum wires, we cannot settle on an isotropic bonding model where all neighboring atoms affect the energy of a lattice site equally. For this reason, an anisotropic bonding model was developed based on the equilibrium crystal shape of GaAs and InAs found in

[8, 9]. First we approximate the crystal structure of the group III atoms to be cubic instead of face centered cubic (FCC). This is illustrated in figure 3.8 where the four Ga atoms in red are reconfigured to the four green atoms or simulated units. Furthermore, because of their alignment along the $(\bar{1}10)$ and (110) directions, these are chosen as the x and y axes in the simulation[6]. It is important to note that the new unit cell (one atom per cell) is tetragonal with dimensions $(L/\sqrt{2}, L/\sqrt{2}, L/2)$ where L the lattice constant of the material such as 5.8687 Å for InP.

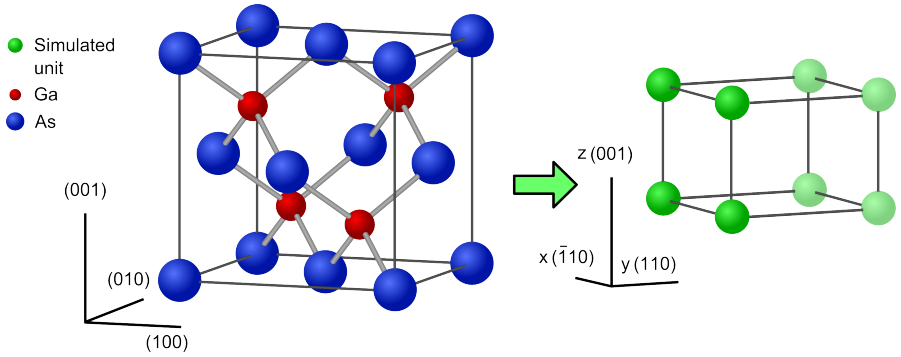

Figure 3.8: Rearrangement of the face-centered cubic distributed Ga atoms into a tetragonal lattice.

Appendix B explains how particular surface energies can be emulated by varying the strength of atomic bonds in different directions. The bonds that are used to represent III-V semiconductors in this work are illustrated in figure 3.9 along with their crystallographic directions. Only first and second nearest neighbor bonds are considered as this still allows for bonds in the (111) and $(\bar{1}11)$ directions which is important for faceting in these directions.

Because the purpose of this bonding model is to properly simulate the anisotropy between the (110) and $(\bar{1}10)$ directions, the model includes 6 different bond energies labeled a_1, a_2, a_3, b_1, b_2, and c. a_1 and a_2 are distinct since they are the bonds in these two directions. b_1 and b_2 are distinct since they are also preferentially oriented toward either the $(\bar{1}10)$ or the (110) direction and the surface energies of the (111) and $(\bar{1}11)$ facets are different from each other. a_3 is distinct from a_1 and a_2 since it is along the (001) direction. Finally, there is no distinction between the four bonds labeled c since there is no preferential alignment along either of the anisotropic directions.

[6]The y axis can be chosen to be the $(\overline{1}\overline{1}0)$ or the x axis can be chosen to be $(1\bar{1}0)$ to maintain a right-handed system ($\hat{z} = \hat{x} \times \hat{y}$) since opposite directions are equivalent.

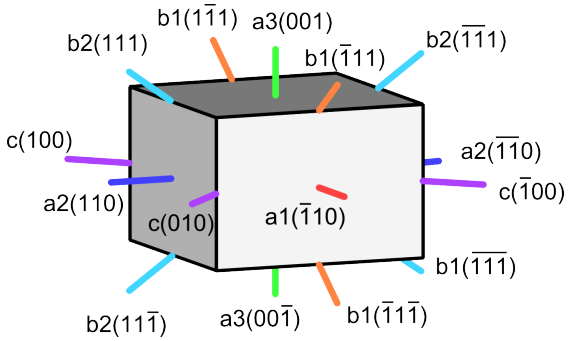

Figure 3.9: Bond strength and crystallographic direction of first and second nearest neighbor bonds.

Based on the equations derived in appendix B we can express various surface energies in terms of these identified bonds. Equations (3.44) through (3.49) show these relationships. Technically, all these equations should have a negative sign in front of them since bond strengths are negative and surface energies are positive, but for the sake of simplicity, the equations are left positive here even though the values in tables 3.2 and 3.3 in sections 3.6.2 and 3.6.5 are negative. The expressions for γ_{001}, $\gamma_{\bar{1}10}$ and γ_{110} are based on the broken bonds of a flat surface since they corresponds to the z, x and y directions in our model, respectively and surface energies γ_{100}, $\gamma_{\bar{1}11}$ and γ_{111} are based on equation (B.40) for a surface with steps along one direction. l_x, l_y and l_z are the dimensions of our tetragonal unit cell.

$$\gamma_{001} = \frac{a_3 + 2b_1 + 2b_2}{2l_x l_y} \tag{3.44}$$

$$\gamma_{100} = \frac{a_1 + a_2 + 2b_1 + 2b_2 + 2c}{2l_z\sqrt{l_x^2 + l_y^2}} \tag{3.45}$$

$$\gamma_{\bar{1}11} = \frac{a_3 + a_1 + 2b_1 + 2b_2 + 2c}{2l_y\sqrt{l_x^2 + l_z^2}} \tag{3.46}$$

$$\gamma_{111} = \frac{a_3 + a_2 + 2b_1 + 2b_2 + 2c}{2l_x\sqrt{l_y^2 + l_z^2}} \tag{3.47}$$

$$\gamma_{\bar{1}10} = \frac{a_1 + 2b_1 + 2c}{2l_y l_z} \tag{3.48}$$

$$\gamma_{110} = \frac{a_2 + 2b_2 + 2c}{2l_x l_z} \tag{3.49}$$

These equations can be rewritten in terms of Γ_{hkl} which is the surface energy per surface atom and the lattice constant L as shown in equations (3.50) through

(3.55).

$$\Gamma_{001} = 2l_x l_y \gamma_{001} = L^2 \gamma_{001} = a_3 + 2b_1 + 2b_2 \tag{3.50}$$

$$\Gamma_{100} = 2l_z \sqrt{l_x^2 + l_y^2} \gamma_{100} = L^2 \gamma_{100} = a_1 + a_2 + 2b_1 + 2b_2 + 2c \tag{3.51}$$

$$\Gamma_{\bar{1}11} = 2l_y \sqrt{l_x^2 + l_z^2} \gamma_{\bar{1}11} = \sqrt{3/2} L^2 \gamma_{\bar{1}11} = a_3 + a_1 + 2b_1 + 2b_2 + 2c \tag{3.52}$$

$$\Gamma_{111} = 2l_x \sqrt{l_y^2 + l_z^2} \gamma_{111} = \sqrt{3/2} L^2 \gamma_{111} = a_3 + a_2 + 2b_1 + 2b_2 + 2c \tag{3.53}$$

$$\Gamma_{\bar{1}10} = 2l_y l_z \gamma_{\bar{1}10} = L^2/\sqrt{2} \gamma_{\bar{1}10} = a_1 + 2b_1 + 2c \tag{3.54}$$

$$\Gamma_{110} = 2l_x l_z \gamma_{110} = L^2/\sqrt{2} \gamma_{110} = a_2 + 2b_2 + 2c \tag{3.55}$$

From these equations we can come to a few conclusions even without numerical values. Since $\gamma_{001} = \gamma_{100}$ due to the symmetry of the crystal, $\Gamma_{001} = \Gamma_{100}$ based on our choice of axes. From equations (3.50) and (3.51), we can see that $a_3 = a_1 + a_2 + 2c$ which implies that a_3 bonds are significantly stronger than other bonds. From equations (3.52) and (3.53) we can see that $a_1 - a_2 = \Gamma_{\bar{1}11} - \Gamma_{111}$. This is what reveals the anisotropy of the crystal since the $(\bar{1}11)$ and (111) surfaces have a different atomic configuration and consequently have different surface energies $\gamma_{\bar{1}11}$ and γ_{111}. Because $\gamma_{\bar{1}11}$ is greater than γ_{111}, a_1 is a significantly stronger bond than a_2 and this is what leads to the formation of wires as opposed to dots. Moreover, since $\gamma_{\bar{1}10} = \gamma_{110}$, $\Gamma_{\bar{1}10} = \Gamma_{110}$ and therefore $a_1 + 2b_1 = a_2 + 2b_2$. This reveals that the bonds along the surface in the $(\bar{1}10)$ direction (a_1) are stronger but the diagonal bonds along that same direction are actually weaker. This promotes strong (111) faceting as demonstrated in section 3.6.

Although our model employs anisotropic bond strengths in order to simulate the formation of wires, this does *not* infer that bonds between group III atoms are physically stronger along some directions rather than others. The anisotropic bond model described here is used to simulate the effect that the surface reconstruction has on the energetically favorable configuration of adatoms.

Another limitation to keep in mind is that without somehow explicitly considering the presence of the group V element, it is actually not possible to produce a bond model which properly accounts for the full equilibrium crystal shape of

III-V semiconductors. There are two ways to understand that. The first way is to consider the (111) and the $(\overline{111})$ facets. These are opposing facets yet they have different surface energies. In order to obtain different surface energies using a bonding model similar to ours, the bonds in the (111) direction and in the $(\overline{111})$ direction would need to be different. That means that if atom A is connected to atom B via a (111) bond, it would have to be attracted to B with a different energy than the B atom is attracted to it. This type of uneven attraction is not physically possible. Another way of looking at it is to simply consider that based on the geometry of the zinc blende structure, if quantum wires were to be grown on both opposing sides of the substrate, the wires on the top would be perpendicular to those on the bottom. This implies that on top, say if bond a_1 is greater than a_2, then on the bottom the scenario is the opposite. However, since our model does not allow for overhangs, it is not possible to have such problematic opposing faces and so this does not need to be considered[7]

3.5 Other Details

3.5.1 Boundary Conditions

In order to simulate physical phenomena in a large (N-dimensional) space without the interference of edge effects due to unrealistic boundary conditions, periodic boundary conditions (PBC) are often applied to such problems. Some problems actually involve periodic geometries (such as perfect crystalline lattices) and applying such boundary conditions is natural but in our case we simply cannot simulate a very large substrate for computational reasons and periodic boundary conditions are a convenient workaround.

Figure 3.10 illustrates simple periodic boundary conditions in two dimensions where shapes overlap vertically and horizontally. We can clearly see how the green square overlaps vertically and how the red triangle overlaps horizontally. These conditions can be expressed mathematically by $f(x + L_x, y) = f(x, y)$ and

[7]Note that the opposing (110) and $(\overline{1}10)$ facets do not have this problem.

$f(x, y + L_y) = f(x, y)$ where L_x is the periodicity in x, L_y is the periodicity in y and f can be any function such as lattice site energy, displacement (strain) or atom occupancy. Figure (3.11) illustrates a slightly more complicated case where the vertical periodicity is accompanied by a horizontal shift, analogous to an oblique lattice. These boundary conditions can be expressed by $f(x + L_x, y) = f(x, y)$ and $f(x, y + L_y) = f(x + \Delta x, y)$ were Δx is the horizontal shift.

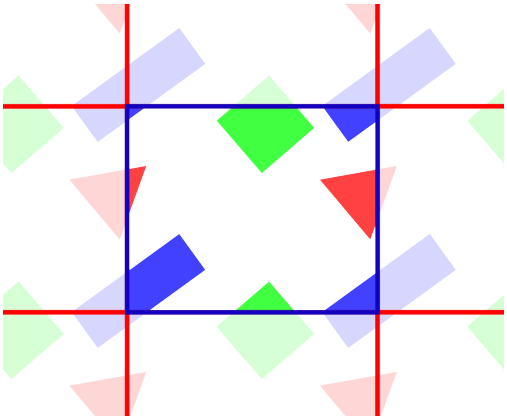

Figure 3.10: Simple 2D periodic boundary conditions.

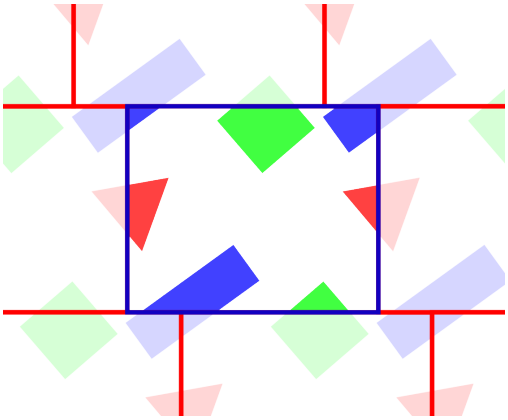

Figure 3.11: 2D periodic boundary conditions with a horizontal translation.

To simulate a flat substrate, only the first type of PBC in x and y is necessary to connect all four sides[8]. In order to study the effect of surface steps on epitaxial growth however, there are two possible approaches. The first is to produce a stepped substrate during the initialization of the simulation and apply the regular periodic boundary conditions. The resulting geometry will effectively have a sawtooth shape as illustrated in figure (3.12a) which will erode from surface diffusion. It is possible to then simply ignore the results near the problematic edges as was done in [36].

However, this is problematic when simulating the deposition of many monolayers of material as the effect of this edge will spread over a large portion of the simulated substrate. For this reason, the boundary conditions illustrated in figure 3.12b were implemented. They are expressed mathematically in 3 dimensions for an $n_x \times n_y$ grid in equations (3.56) and (3.57) where N_{steps} is the number of steps in the y direction. This allows to simulate steps in the (110) and in the $(\bar{1}10)$ direction by swapping the bond strengths $a_1 \leftrightarrow a_2$ and $b_1 \leftrightarrow b_2$ but not in the (100) direction or

[8]If you pay close attention to figure (3.1), the number of nearest neighbors was calculated assuming periodic boundary conditions.

(a) Regular periodic boundary conditions.

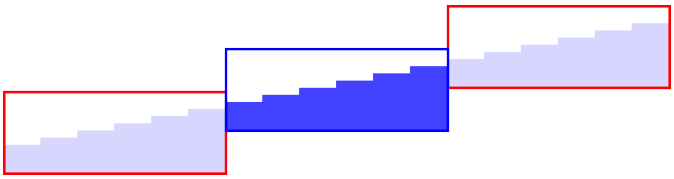

(b) Shifted periodic boundary conditions.

Figure 3.12: Two different types of periodic boundary conditions applied to an off-cut substrate.

any intermediate directions (such as (210)). Finally, Dirichlet boundary conditions are used on the bottom surface of the simulated substrate where the displacement fields U, V and W are held at 0. This surface is around 20 monolayers below the top surface in most simulations.

$$f(x + n_x, y, z) = f(x, y, z) \tag{3.56}$$

$$f(x, y + n_y, z) = f(x, y, z - N_{steps}) \tag{3.57}$$

3.5.2 Hopping Rate

Finding the bonding strength of surface atoms to the substrate and between each other is obviously very important but two other important variables are the base rate R_0 and the activation energy E_0 from equation (3.1). One of two models is generally used in the literature for the value of R_0. The first is equation (3.58) where h is Planck's constant. It is used in many kMC diffusion models [37--39] and is based on the equipartition theorem [40]. Others use a constant that is independent of temperature which either relies on simulation results[27], experimental findings [41] or based on the transverse optical phonon frequency [42]. The importance of this constant with respect to the model is to properly measure the amount of time being simulated, that is, the amount of time Δt that passes between each simulation step. It is basically a direct constant of proportionality between adatom displacements and the deposition rate to know how many adatoms to deposit after 1000 simulations steps for example.

$$R_0 = \frac{2k_B T}{h} \tag{3.58}$$

As for the activation energy, it is typically a positive value in the case where the bonding energy to the surface is not already considered and would encapsulate this bonding term. It would basically compensate for the fact that such a model assumes that an adatom has the same energy level as vacuum which is of course not physical. In our case, since we do consider the bonding energy to the substrate, E_0 is actually a negative term that represents the difference in energy between vacuum and the threshold level illustrated by the peaks in figure 3.2. The bonding energy of an adatom on the flat substrate in our model is given by $(a_3 + 2b_1 + 2b_2)$ since it is bonded to the atom directly beneath it (a_3), two second nearest neighbors in the $(\bar{1}1\bar{1})$ and $(1\overline{11})$ directions (b_1) and two second nearest neighbors in the $(11\bar{1})$ and $(\overline{111})$ directions (b_2). As it turns out in our model, E_0 is (realistically) lower than the vacuum level. What is really important about this value however is how it affects the hopping rate in relation to temperature. Although R_0 and E_0 can be set somewhat arbitrarily to provide a proper time scale at a single temperature, they must both be chosen carefully to properly simulate the time scale at a variety of temperatures.

The values of R_0 and E_0 were determined based on reflection high energy electron diffraction (RHEED) oscillations which indicate whether or not step flow growth occurs[41] during homoepitaxial or unstrained growth. Step flow growth occurs when the deposition rate is slow enough for a given material, substrate off-cut and temperature so that all deposited adatoms migrate to a surface step without forming 2-dimensional islands on the terraces. When islands do form, the substrate surface becomes rough and the intensity of certain RHEED reflections becomes dim. As the deposition of a monolayer is completed, the gaps between islands are filled and the surface becomes fairly smooth again. This process is repeated as another monolayer is deposited and so the intensity of the RHEED pattern oscillates. Under conditions of step flow growth however, this oscillation never occurs since no islands form and the substrate surface remains smooth throughout the deposition process. Since the transition to step flow growth depends on surface diffusion which in turn

depends on R_0 and E_0, RHEED oscillations can be simulated in order to effectively calibrate our model based on experimental RHEED patterns from the literature.

RHEED oscillations can be simulated by using equations (3.59) and (3.60) adapted from work by Grosse *et al.* [42]. I_x is the intensity of the RHEED reflection along the x direction, n_x and n_y are the dimensions of the simulated substrate, $\delta_{a,b}$ is the Kroneker delta[9] and $h(i,j)$ is the height of the substrate at the location (i,j). This means that flat regions of the substrate result in a high intensity whereas uneven regions result in a low intensity, similar to actual RHEED pattern intensities. In their work, they determine the value of E_0 for GaAs and AlAs by simulating RHEED patterns and comparing them to experimental patterns from homoeptiaxial growths at different temperatures. There is a critical temperature past which oscillations no longer occur and this can be matched. The same is done in this work to assure that reasonable values are used in our model.

$$I_x = \frac{1}{n_x n_y} \sum_{i,j}^{n_x,n_y} \delta_{h(i,j),h(i+1,j)} \tag{3.59}$$

$$I_y = \frac{1}{n_x n_y} \sum_{i,j}^{n_x,n_y} \delta_{h(i,j),h(i,j+1)} \tag{3.60}$$

The threshold energy determined in [42] for GaAs is $E_0 = 1.64$ eV which, applied to our model, gives us $1.64 = a_3 + 2b_1 + 2b_2 + E_0$. Using this value and $R_0 = \frac{2k_BT}{h}$, RHEED oscillation curves were obtained from homoepitaxial simulations to match Grosse's work and calibrate our model. Figure 3.13 shows the results of these simulations at temperatures between 520°C and 590°C for a deposition rate of 0.2 ML/s on a 2° off-cut substrate (20 atom step length). In each simulation, 4 ML of material (GaAs) were deposited over a period of 20 s followed by a 20 s annealing period. We can clearly see here that the oscillations are less prominent and disappear at higher temperatures. The so called "critical temperature" at which the oscillations are no longer present seems to be between 580°C and 590°C which matches Grosse's findings, although the precise cutoff is ambiguous.

It is important to note that the simulated oscillations are generally quite noisy

[9]The Kroneker delta is equal to 1 if both indices are equal and 0 otherwise.

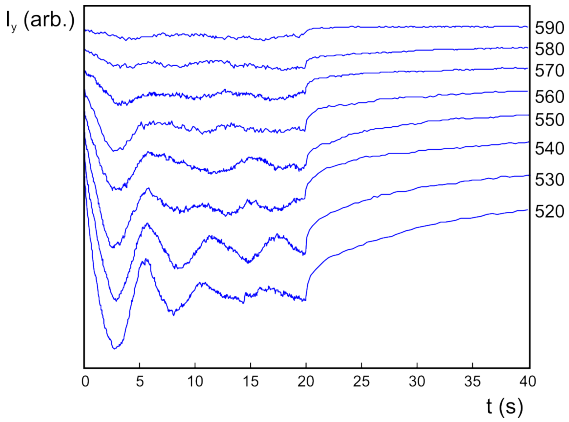

Figure 3.13: Simulated RHEED oscillations at various temperatures for a deposition rate of 0.2 ML/s on a 2° off-cut substrate followed by a 20 s annealing period at the 20 s mark. Plots at different temperatures are artificially shifted vertically but the scale is the same for each.

and variable compared to experimental measurements because of the small area that is being simulated. The plots found here were generated using a 200×200 grid ($n_x = n_y = 200$) which represents an 80 nm by 80 nm area. Furthermore, unlike in other types of measurements, the amount of high frequency noise in these plots is an underestimate of the actual variability of the data due to the stochastic nature of this roughening process. We see the result of this if we compare the 520°C plot to the 530°C plot. The large oscillations are significantly clearer in the latter than the former which is not the case in experiments and if the simulation was performed again, this would likely be different. The sharpness of the first trough and peak however changes quite consistently with increasing temperature which can greatly help in determining the critical temperature. Finally, since the experiments referred to in [42] were performed on substrates with a 2° off-cut toward the (100) direction to avoid any anisotropic effects, our simulations were performed using isotropic bonds such that $a = (a_1 + a_2)/2$ and $b = (b_1 + b_2)/2$ with steps in the (110) direction (along the $(\bar{1}10)$ direction).

Figures 3.14 and 3.15 show the topography at different stages of growth of the simulated substrates used to produce the RHEED plots at 520°C and 590°C. Each of the subfigures are 200 by 200 pixel images where each pixel represents an atom and lighter atoms are higher than darker ones. Figures 3.14a and 3.15a show substrates after 0.5 ML of material has been deposited. At this stage for the 520°C case, the density of 2D islands is maximal and we can see that after

1 ML (figure 3.14b), most of the gaps between these islands have been filled. This explains why the substrate becomes smooth again and the RHEED intensity increases. This is not the case for the growth at 590°C where islands are sparse since adatoms have enough time to reach step edges without coalescing. The presence of very few islands also explains why the RHEED plots are more variable at higher temperatures since the relative difference in roughness between 3 and 5 islands is much greater than that between 130 and 150 islands of more variable size. Figure 3.14c shows how the distinction between stages of island formation and filling becomes less apparent during growth and this explains why RHEED oscillations level off. Finally, we can see the smoothing effect of annealing by comparing figures 3.14c and 3.14d as well as 3.15c and 3.15d. In the former case (520°C) we can clearly see that the steps and the islands have become smoother and some islands have even dissolved into the steps. After a long enough period of time, all the islands would dissolve and this is a good indicator that molecular beam epitaxy is indeed not in thermodynamic equilibrium since the surface atoms have not yet reached their equilibrium energy state. The smoothing at 590°C is less obvious since it is already fairly smooth in figure 3.15c. We can see however that the few islands present have disappeared after annealing.

For comparison with these results, figures 3.16 and 3.17 show simulated RHEED oscillations under similar conditions (temperature range, annealing time, off-cut angle, etc.) as above but for deposition rates of 0.1 ML/s and 0.4 ML/s. We can see that the lower deposition rate leads to a lower critical temperature between 550°C and 560°C and the faster rate increases it above 590°C.

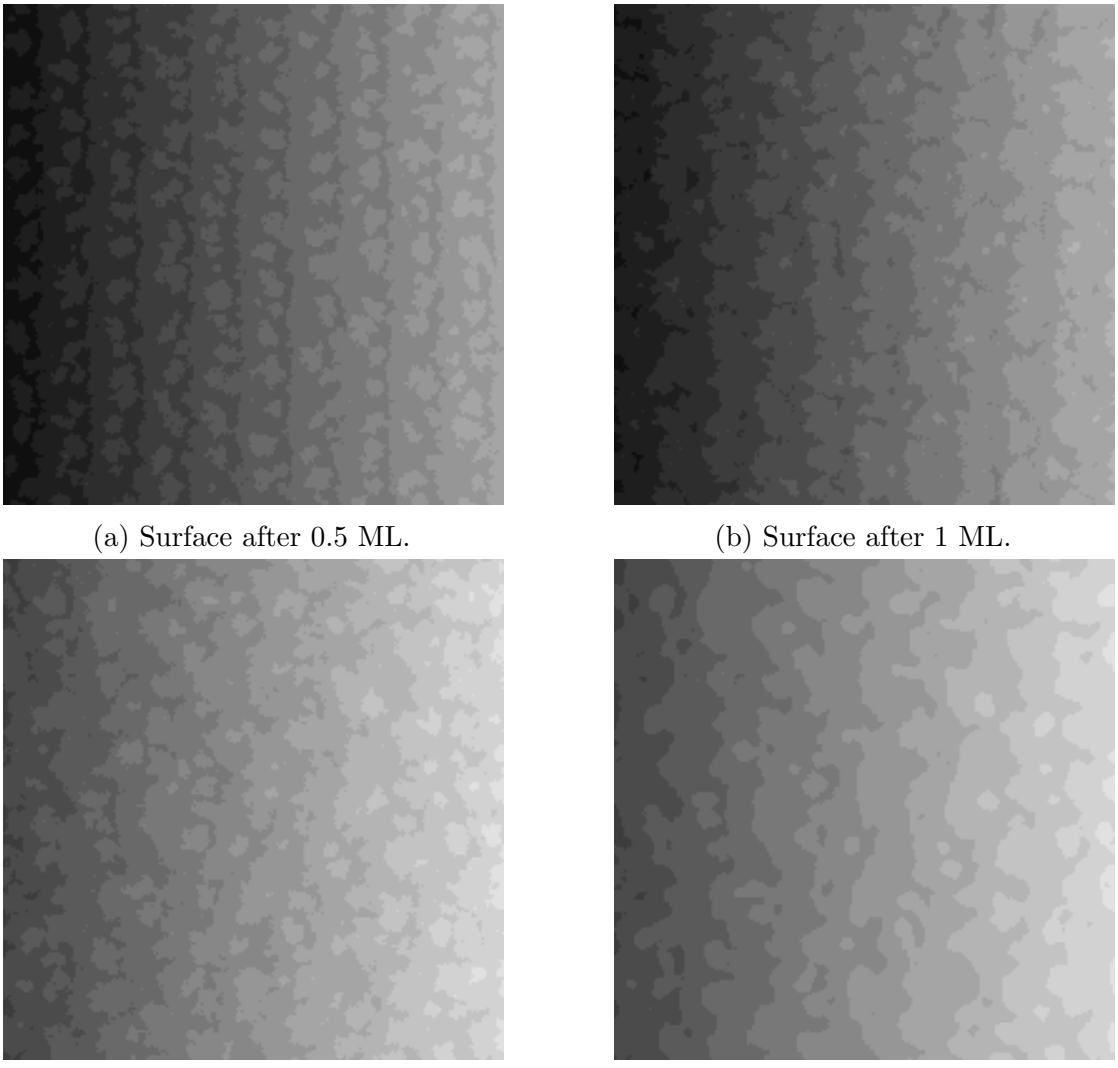

(a) Surface after 0.5 ML.

(b) Surface after 1 ML.

(c) Surface after 4 ML

(d) Surface after annealing.

Figure 3.14: Topography of GaAs homoepitaxy at different stages of growth at 520°C. The same gray scale has been applied to all four images.

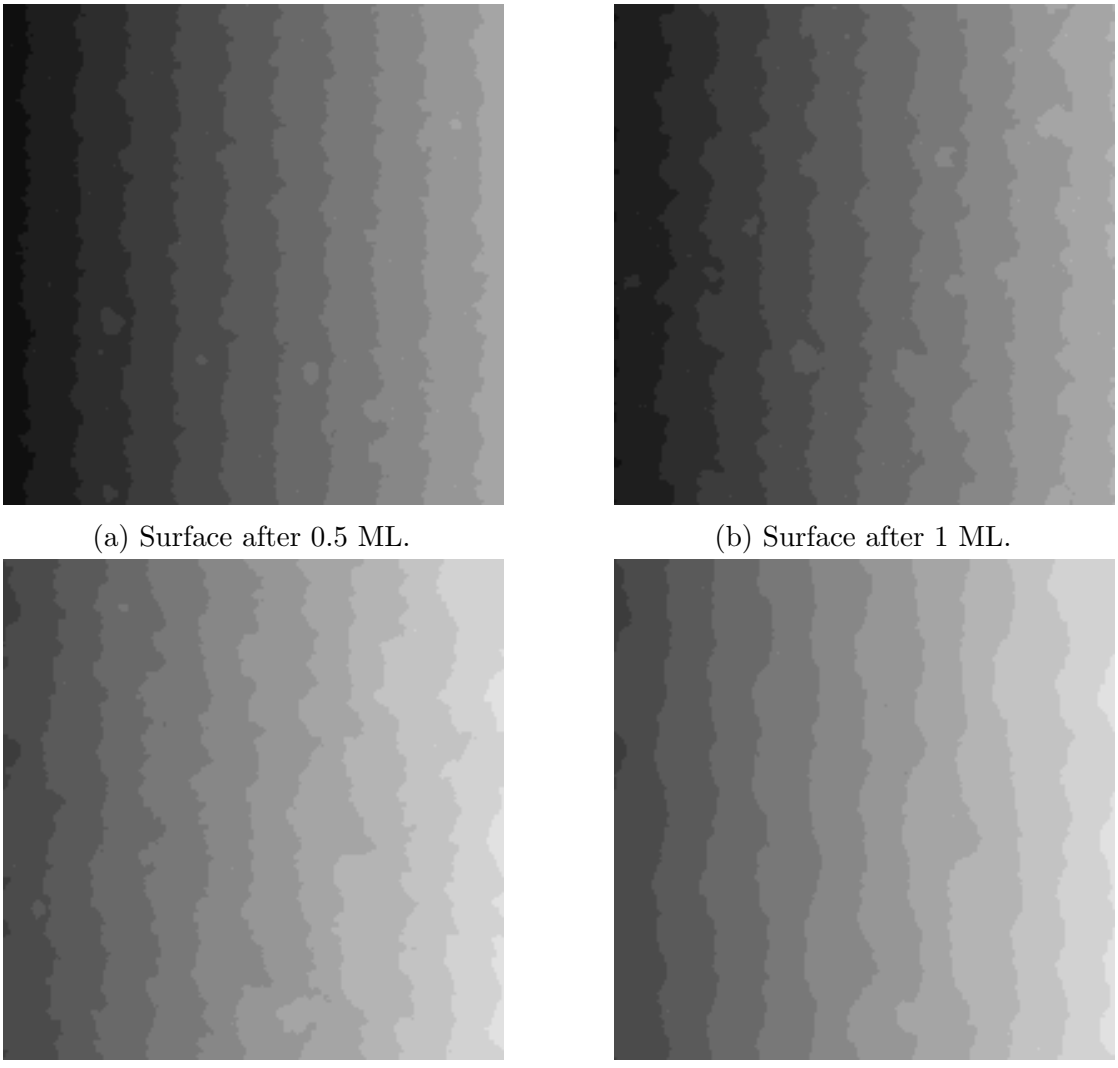

(a) Surface after 0.5 ML.

(b) Surface after 1 ML.

(c) Surface after 4 ML

(d) Surface after annealing.

Figure 3.15: Topography of GaAs homoepitaxy at different stages of growth at 590°C. The same gray scale has been applied to all four images.

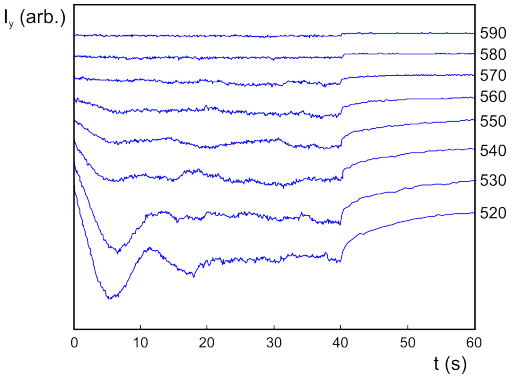

Figure 3.16: Simulated RHEED oscillations for a deposition rate of 0.1 ML/s.

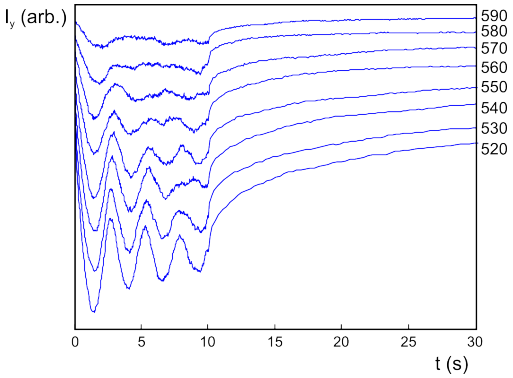

Figure 3.17: Simulated RHEED oscillations for a deposition rate of 0.4 ML/s.

3.5.3 Optimizations

Solving the strain equations presented above over a large 3-dimensional lattice is very computationally intensive and is by far the most important bottleneck in this type of simulation. In order to be able to simulate surface diffusion including strain over a reasonable time scale, it is necessary to apply certain approximations to optimize the strain calculations. Three important approximations were applied in the implementation of our model.

The first applies to "free" adatoms with which are adatoms with no first nearest neighbors. Surface atoms which are not bonded to other atoms in the $(\bar{1}10)$ or (110) direction, that is, have no a_1 or a_2 bonds, are ignored in the solution of the strain equation. This is implemented by keeping track of two separate surfaces, one of which has no free adatoms and is used to calculate strain and strain energy, and of course the surface which includes all atoms. This speeds up the simulation considerably since these free adatoms make up a large portion of the simulation events or steps and when such a diffusion event occurs, no strain calculations are required. A similar approximation is used by Schulze *et al.* [27] and their work has shown that this optimization has little or no noticeable impact on their results.

The second approximation affects the frequency at which the strain field is updated. Given that a single atom displacement has a proportionally very small impact on the strain field of the simulated substrate and considering that the effect of strain energy is a cumulative effect over a long range, it would be wasteful to update the entire field for every hopping event. For these reasons, the strain field is only updated locally between the vast majority of the simulation steps. After the displacement of each atom, this local update consists of solving the strain equation in a $3 \times 3 \times 3$ grid around both the old position of the atom in question, that is, where it is moving from, and around its new position. This sort of method has been used since the development of one of the earliest kMC models including full strain calculations to improve the algorithm's efficiency [32]. Every 1000 or so events however, the strain field is relaxed over a larger volume in order to maintain the correct long range solution to the strain equation. This is not done by globally updating the field but rather by using the expanding box method described in

[28, 43]. This method consists of first solving the strain equation over a $5 \times 5 \times 5$ grid or box for example, then expanding this domain to a $6 \times 6 \times 6$ grid. If during the first iteration of the over-relaxation algorithm over this larger domain, the largest obtained residual is greater than a chosen threshold, the strain field over the large grid is relaxed and the expansion process is repeated. This is done until either a small enough residual is found after expanding the solution domain or the box encompasses the entire strain field at which point the entire strain field is relaxed.

The third approximation that is made concerns the calculation of the strain energy. When an atom arrives at a bonding site and displaces its neighboring atoms, the strain energy it brings to the thin film is stored among many other atoms in its vicinity, not only its nearest neighbors. In order to properly account for the total energy E_S it brings to the system and how it affects the probability with which it is expected to leave this site (rate R), we need to consider the total strain energy of the substrate with this atom's presence and without it. As one would expect, this would require a large number of calculations. However, it is possible to account for this total strain energy by simply calculating the local strain energy of the atom, that is, the energy in the "springs" between it and its nearest neighbors[10], and multiplying it by a constant of proportionality referred to as the strain factor in our work. Figure 3.18 shows the difference in the total energy of a $120 \times 120 \times 25$ substrate with and without one of the surfaces atoms plotted against the local strain energy of the same atom. To clarify, a full simulation was first run in order to produce a substrate with quantum wires. Next the total strain energy of all the atoms which make up the substrate was calculated. Then for each of the $120 \cdot 120$ surface sites, the topmost atom was removed, the strain field of the substrate was solved (relaxed) and the total strain energy of the substrate was calculated again. The difference between these two values are then compared to the local strain energy around each surface atom individually on the plot in figure 3.18.

The resulting plot is quite linear and has a slope of about 1.27. This basically tells us that on average, the total strain energy contributed by an atom is 1.27

[10]This includes up to 6 first nearest neighbors and 12 second nearest neighbors depending on nearby vacancies.

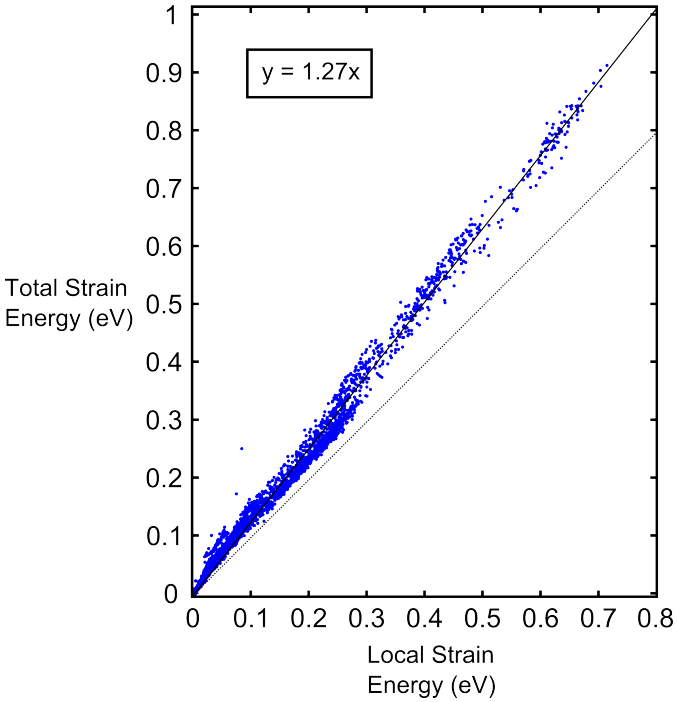

Figure 3.18: The total strain energy contribution of surface atoms plotted against their local strain energy. The full line is a linear fit to the data and the dotted is the function $y = x$.

times the strain stored between it and its nearest neighbors. The slope obtained from an earlier calibrations performed during the development of the kMC model was closer to 1.3 and for this reason, a strain factor of 1.3 is used throughout this work. To be explicit, this means that the effective spring constant used to calculate strain energy in InAs is $k_1 = 25.6$ eV instead of $k_1 = 19.7$ eV.

3.6 Simulation Results

3.6.1 Equilibrium Island Shape

In order to demonstrate the influence that anisotropic bonds have on the equilibrium crystal shape, or more precisely the equilibrium island shape, a simplified kinetic Monte Carlo model was used to simulate annealing a 2-dimensional island with various bonding configurations while ignoring strain. Similar to the simple model

presented in figure B.2 from appendix B, the model used here consists of adatoms which have horizontal and vertical bonding energies a and b between their first nearest neighbors. Moreover, the substrate in these simulations was fixed and unable to mix with the adatoms placed on its surface. Each simulation began with a square island of atoms which were allowed to diffuse and over the simulation period, the dimensions of this island were measured. Figure 3.19a shows the initial square island used for all the simulations in this section. The size of the island is initially 30 by 30 atoms and the size of the (periodic) substrate is 120 by 120. Figure 3.19b shows a typical island shape during the simulation with a bond ratio of 2:1. Finally, figure 3.19c shows the average shape of the island measured between $2 \cdot 10^8$ and $10 \cdot 10^8$ simulation steps.

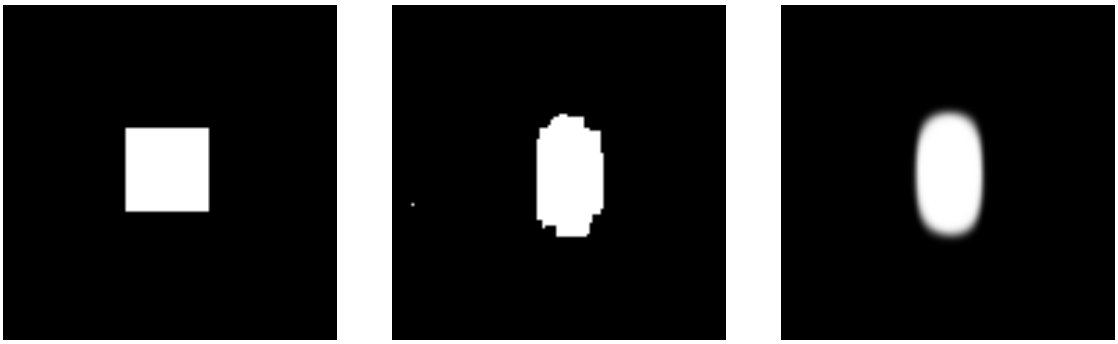

(a) Initial shape of the simulated 2D island.

(b) Shape of the island after $6 \cdot 10^8$ simulation steps.

(c) Average island shape between $2 \cdot 10^8$ and $10 \cdot 10^8$ simulation steps.

Figure 3.19: Simulated 2D island with a bond ratio of 2:1.

The height and width of the island were calculated using the vertical and horizontal standard deviation of the position of each atom connected to it. The ratio of these length measurements (aspect ratio) was recorded over the progress of the simulation and the results of simulations performed with $b : a$ ratios of 1:1, 2:1 and 3:1 are plotted in figure 3.20. The horizontal axis is the number of simulation steps (adatom hops). Such numerous simulation steps were required to make sure that the trends were stable and not just a random fluctuation and as can be seen in this figure, the variability of the aspect ratio is rather large. We can observe a clear trend where all three plots begin with an aspect ratio of 1 and converge near the same ratio as that of their bond strengths. The average value of the curves for bond ratios of 1, 2 and 3 after $2 \cdot 10^8$ simulation steps is 0.98 ± 0.11, 1.83 ± 0.17 and 2.68 ± 0.28, respectively. The second and third values are smaller than expected

but this is likely due to the rounding of the island corners observed in figure 3.19c. Nonetheless, these observations strongly support the theory developed in appendix B.

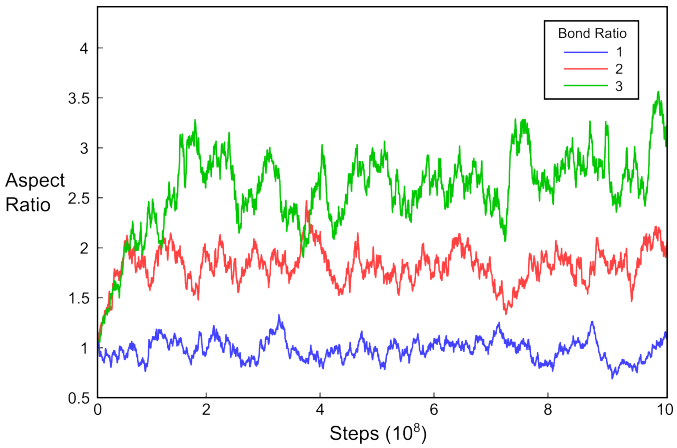

Figure 3.20: Evolution of the size ratio of a 2D island for anisotropic bond ratios of 1:1, 2:1 and 3:1.

A similar set of experiments were run to measure the effect of anisotropic diffusion. In figure 3.21, the evolution of the aspect ratio of a 2D island was recorded under three different conditions. The curve denoted by A was produced by a simulation where the first nearest neighbor bonds were isotropic but the diffusion constant R_0 was 4 times greater in the vertical direction than in the horizontal direction. Similarly to the isotropic bond case above, the average aspect ratio was 1.01 ± 0.09. Furthermore, plots B and C in figure 3.21 were both recorded from a simulation with a bond ratio of 2:1 but with surface diffusion ratios of 4:1 and 1:4 respectively. The average aspect ratio was 1.83 ± 0.19 and 1.86 ± 0.17 for the two cases. These results clearly show that the anisotropic shape of epitaxial islands under conditions which are not kinetically limited depends on the anisotropy of the energy configuration of adatom and not anisotropic diffusion. It is therefore incorrect to state that InAs are aligned along the $(\bar{1}10)$ because of anisotropic surface diffusion. However, under kinetically limited conditions, surface diffusion can play a role in the shape of epitaxial islands.

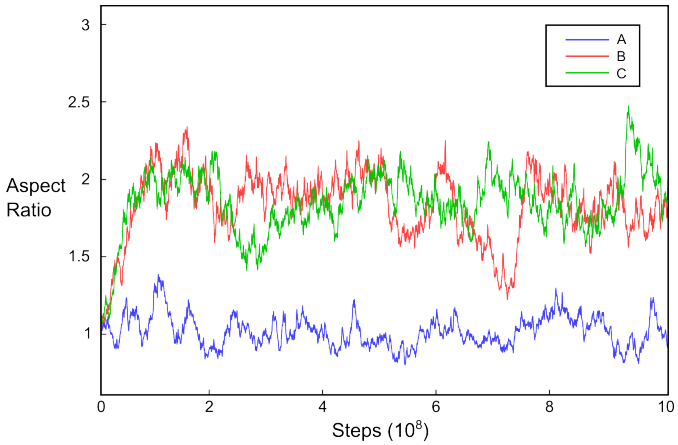

Figure 3.21: Evolution of size ratio of a 2D island. Simulation A had isotropic bonds and a 4:1 diffusion ratio. Simulations B and C had anisotropic bonds (2:1) and diffusion ratios of 4:1 and 1:4, respectively.

3.6.2 Bond Energies

Based on the surface energies given for the different facets of GaAs in [8], the anisotropic bonding model was developed using the expressions for Γ_{001}, Γ_{100}, $\Gamma_{\bar{1}11}$, Γ_{111}, $\Gamma_{\bar{1}10}$ and Γ_{110} given in equations (3.50) through (3.55) of section 3.4. Since we have 6 equations and 6 unknowns (a_1, a_2, a_3, b_1, b_2 and c), the system should have an exact solution. The problem however is that the solution of this system of equations results in positive bond strengths for a_1 and a_2 which is nonphysical as it causes surface atoms to repel each other. In order to resolve this problem, we are required to add a supplementary constraint. Because based on our tetragonal model, the furthest neighbor is actually along the c bond in the (100) direction, after much experimentation a reasonable constraint was determined to be $(a_1 + a_2)/2 = 4c$. This means that the diagonal c bond is 1/4 of the average strength of the a_1 and a_2 bonds. This restriction is fairly arbitrary and many other restrictions could have been applied but this one has produced reasonable results and allows for the surface energies to correspond well with the ones in [8].

Table 3.1 shows the surface energy per surface atom Γ for the various crystal facets based on the values given in Moll's work as well as the surface energies which result from our choice of bond strengths in table 3.2. Table 3.2 shows the bond strengths obtained by solving the equations mentioned above exactly (ECS column)

and those obtained after applying the additional constraint to c. Again based on experimentation with a range of values, the surface energies extracted from the plots in Moll's work correspond to those predicted using a chemical potential of $\mu_{\text{As}} - \mu_{\text{As(bulk)}} = -0.23$ eV. The choice of this value is solely based on simulations run using a range of bonding energies, not on any relationship between the chemical potential and the V/III ratio.

Γ (eV)	ECS	This Work
Γ_{001}	1.89	1.85
Γ_{100}	1.89	2.00
$\Gamma_{\bar{1}11}$	2.35	2.37
Γ_{001}	2.12	2.13
Γ_{001}	1.18	1.07
Γ_{001}	1.18	1.07

Table 3.1: The surface energy per surface atom for various facets based on the equilibrium crystal shape of GaAs in [8] and based on the bond strengths in our model shown in table 3.2.

Bond (eV)	ECS	This Work
a_1	+0.002	-0.385
a_2	+0.237	-0.150
a_3	-0.227	-0.521
b_1	-0.357	-0.274
b_2	-0.474	-0.391
c	-0.233	-0.067

Table 3.2: First and second nearest neighbor bond strengths of GaAs based on the equilibrium crystal shape in [8] and with the additional constraint $(a_1 + a_2)/2 = 4c$.

These tabulated values however are not only the bond strengths for GaAs but are directly related to the other compounds as well. The bond strengths for InAs and AlAs were determined by comparing the (110) surface energies of these three compounds, GaAs, InAs and AlAs. The values for these surface energies are found in [24] and were obtained using density functional theory (DFT) calculations. The two ratios used with respect to GaAs are 0.827 for InAs and 1.134 for AlAs. This means that the a_1 bond for InAs is equal to 0.827 times that of GaAs, and so on. Finally, similar to the case for the inter-species mismatch, the bonds between GaAs and InAs for example, have an energy of $(1 + 0.827)/2$ times that of GaAs.

3.6.3 The Effect of Strain

The size of 3-dimensional islands which form as a result of strain relaxation depends mostly on the stiffness of the material being deposited, the mismatch between it and the substrate, and the bonding strength between the atoms it is made of.

This is intuitive since 3-dimensional islands form by sacrificing bonds between neighboring atom. A rough surface has a larger surface area and therefore more dangling bonds which is energetically unfavorable. It is also intuitive that for a given bonding strength, a greater stiffness constant or spring constant (C_{11} or k) will lead to the formation of smaller 3D structures and this is what is demonstrated in this section.

The color map that is used to illustrate the kMC results here and in the next sections is illustrated in figure 3.22 where the color indicates the species of the atom or compound (red for InAs and blue for GaAs) and the lightness indicates the relative elevation of different locations of the surface. The elevation is normalized in each image unless specified otherwise which means that the lightness cannot be directly compared across different images.

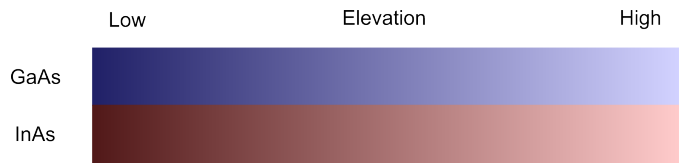

Figure 3.22: Color map used to indicate both the elevation and the nature of the surface atoms in this and the following sections. The color indicates the species of the compound and the lightness indicates its elevation.

Figure 3.23 shows the height profile of simulated isotropic 3D islands which were all produced using the same bonding strengths but with different spring constants. These simulations were performed on a 120 × 120 substrate of InGaAs. For simplicity, the lattice mismatch of InAs with respect the substrate has been set to 0.032 and that of GaAs has been set to -0.032 so that $In_{0.5}Ga_{0.5}As$ is deposited and lattice-matched to the substrate. The substrate on which the InAs was deposited consists therefore of 50% InAs (red) and 50% GaAs (blue). It is worth pointing out that the red and blue substrate is exposed in these images between the islands. The spring constants k_1 that were used[11] are 29.6, 39.4 and 59.1 eV. We can clearly see that intuitively, the stiffer material leads to the formation of smaller islands.

There are a few more interesting features that are worth pointing out. Some of these islands, especially in figure 3.23a, have an irregular shape and are oriented

[11]Recall that these are used with normalized displacements (strain field).

along either the vertical or horizontal direction although on average there is no systematic preference (given a large enough sample size). Although the majority of the island edges in all three maps are faceted, it is particularly noticeable in the third image with the smallest islands. Here we can observe facets along the horizontal and vertical axes which are (111) facets[12] and diagonally oriented facets which correspond to (101) planes. The third image also contains islands with (110) facets which are perpendicular to the substrate and parallel to the "viewing direction". They seem to form mostly between islands which are next to each other.

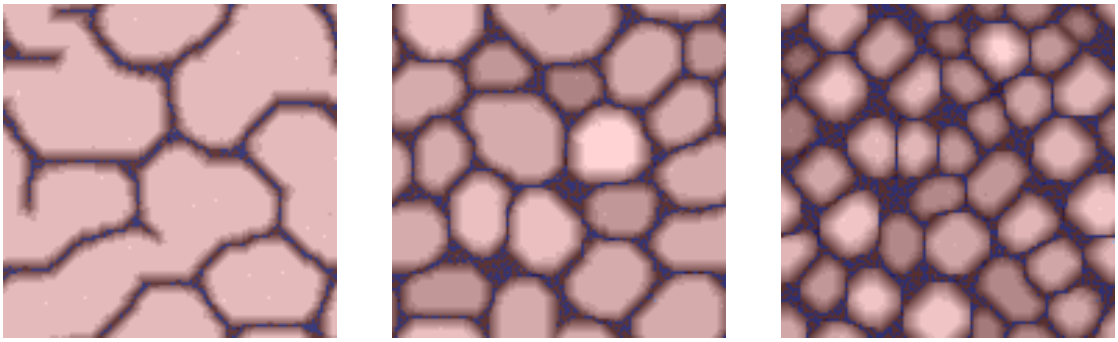

(a) Islands formed using a weak spring constant.

(b) Islands formed using a moderate spring constant.

(c) Islands formed using a strong spring constant.

Figure 3.23: Simulated 3D islands grown using different spring constants.

3.6.4 The Effect of Bond Anisotropy

Section 3.6.1 shows that the aspect ratio of a 2-dimensional island under equilibrium is directly determined by the ratio of the bond strengths in the two directions of interest. However, this is not the case for a strained system and where new island material is being deposited. In fact much greater aspect ratios than those predicted by the ratio of bond strengths can occur. Anisotropic bonds promote the formation of long islands which can coalesce and once they grow large enough, they are "locked into place" due to strain. That is, it would take a large amount of energy and time for them to move or for their shape to change.

Figures 3.24a through 3.24e show the formation of islands given bond strengths

[12]Recall that the coordinate system we use is the (110) and ($\bar{1}$10) crystallographic directions.

with a varying degree of anisotropy. It should be noted that the spring constant used here is $k_1 = 28.2$ eV, including a strain factor of about 1.4. The bond ratio was modified by applying the parametrization in equations 3.61 through 3.64. The primed bonds (d') are the bonds used for this demonstration and the non primed bonds are the values from table 3.2 in section 3.6.2. The first two equations simply change the ratio r between a_1 and a_2 while maintaining their average value. The two other equations insure that the condition $a_1 + 2b_1 = a_2 + 2b_2$ from section 3.4 is satisfied.

$$a_1' = \frac{a_1 + a_2}{2} \cdot \frac{2r}{1+r} \tag{3.61}$$

$$a_2' = \frac{a_1 + a_2}{2} \cdot \frac{2}{1+r} \tag{3.62}$$

$$b_1' = \frac{b_1 + b_2}{2} - \frac{a_1' - a_2'}{4} \tag{3.63}$$

$$b_2 = \frac{b_1 + b_2}{2} + \frac{a_1' - a_2'}{4} \tag{3.64}$$

Figure 3.24a shows the isotropic case where irregularly shaped islands appear with no systematic orientation. Already with a bond ratio of 1.25, we can see an overall elongation in the vertical direction although there is a fair number of horizontal branches and some islands are "bulky". From a bond ratio of 1.5 and up, the islands are clearly elongated and this shows how the formation of long wires does not required bonds that are substantially stronger in one direction than the other. The three last images also have many features in common with the SEM images in chapter 2. The main feature is of course that there are wires all aligned towards the same direction. In these images and those in the following sections, the vertical axis is the $(\bar{1}10)$ direction and the horizontal axis is the (110) direction. An important observation is that the wires are very dense and there is very little bare substrate remaining unlike during the growth of other strained systems such as Ge on Si. Furthermore, just like in our experiments, the shape and size of the wires is fairly variable and contains Y-shaped bifurcations and intersections. There are no signs of regions with larger dot-like structures however like those observed experimentally.

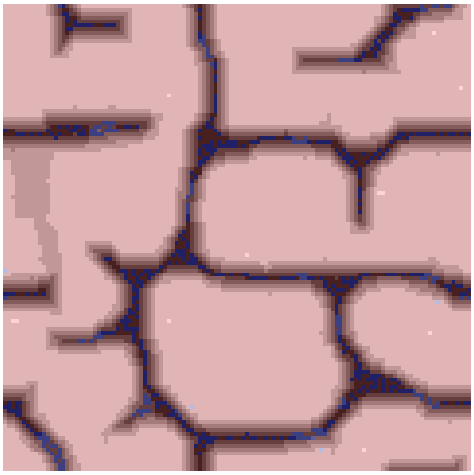

(a) Bond ratio of 1.

(b) Bond ratio of 1.25.

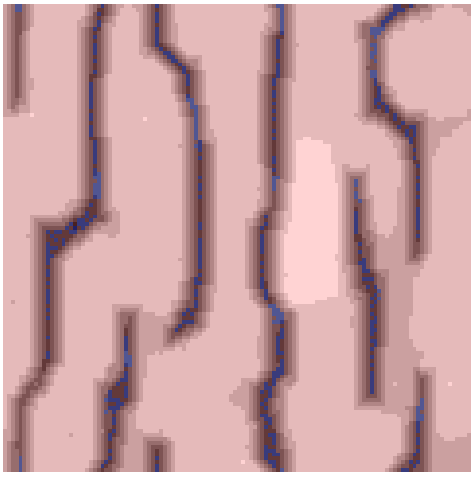

(c) Bond ratio of 1.5.

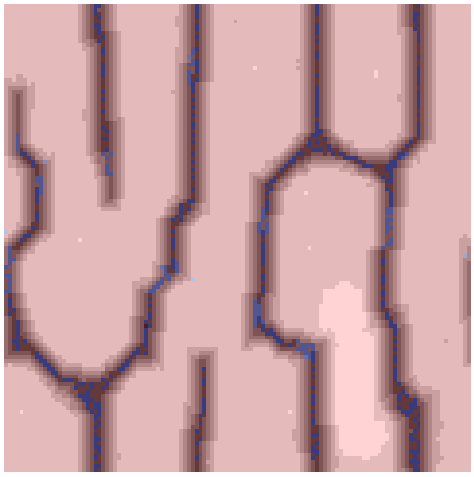

(d) Bond ratio of 1.75.

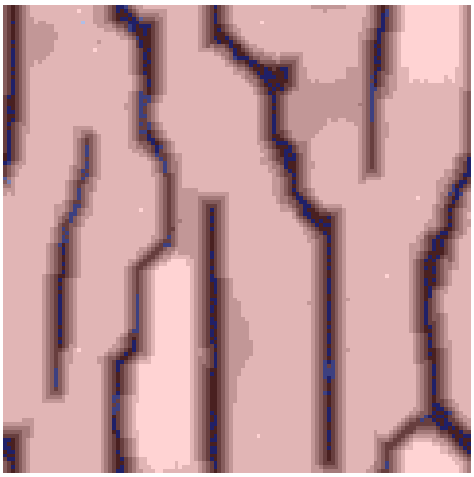

(e) Bond ratio of 2.

Figure 3.24: Topogrpahy of 3D InAs structures formed using various ratios between the a_1 and a_2 bond strenghts.

3.6.5 Stranski-Krastanow Growth

Although the final results of growth simulations performed under various conditions have been shown in the sections above, it is also important to understand the process through which quantum wires form in the first place. The bonding model used for the growth in this section is the one described in section 3.6.2, the growth rate was set to 0.4 ML/s to match our experiments and the growth temperature was 520°C. The substrate once again is InGaAs as described earlier.

Figures 3.25 and 3.26 show the early stages of heteroepitaxial growth on a 120 by 120 atom substrate. The left image shows the surface after the deposition of half a monolayer. We can clearly see the formation of long vertical islands due to the strong bond anisotropy in our model. These 2D islands however do not lead to the formation of 3D islands as they are part of the first wetting layer. The image on the right shows the surface topography after the deposition of just over 1 ML. At this point, the substrate surface is covered by a flat layer of the deposited material and there is no formation of 3D islands. For this system (InAs on InGaAs) it is natural to expect a wetting layer of at least one monolayer since the bonding strength between the deposited material and the substrate is greater than that to itself. Notice here that the same color scale is used among images 3.25 through 3.31 which allows for direct comparison.

After the deposition of about 1.7 ML as illustrated in figure 3.27, the presence of elongated islands is quite obvious but even at this stage it is uncertain whether these will lead to the formation of 3-dimensional islands. As we can see in the next figure, after 2 ML the top region of these "wires" in the middle have coalesced but "cracks" have formed in the first wetting layer at various locations. This is due to an accumulation of strain between wide 2D islands which essentially eject some of the atoms that lie between them.

By the time 2.5 ML have been deposited, it is safe to say that the formation of 3D islands has begun as we can see in figure 3.29. Here we can see several vertical cracks which are misaligned. These cracks cause a large amount of strain to be applied to the regions between them which can ultimately lead to them connecting

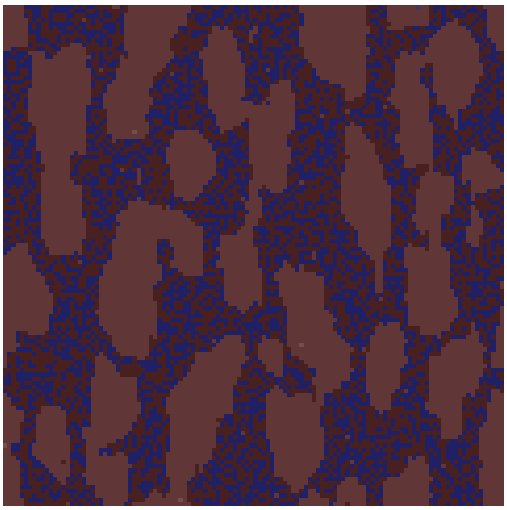

Figure 3.25: 0.5 ML of InAs grown on InGaAs after at a rate of 0.4 ML/s. Elongated 2D islands form but do not persist.

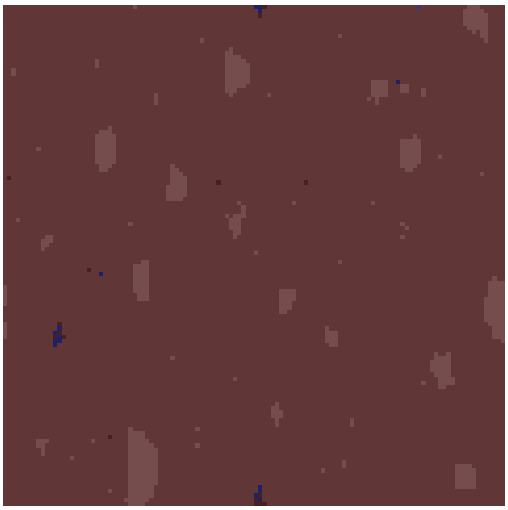

Figure 3.26: Just over 1 ML of InAs grown on InGaAs after at a rate of 0.4 ML/s. A full wetting layer has covered the substrate

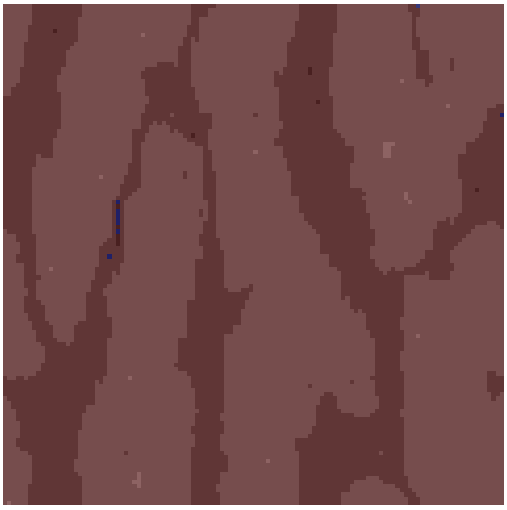

Figure 3.27: 1.7 ML of InAs grown on InGaAs after at a rate of 0.4 ML/s. Long islands have formed above the wetting layer due to the anisotropic bonding model.

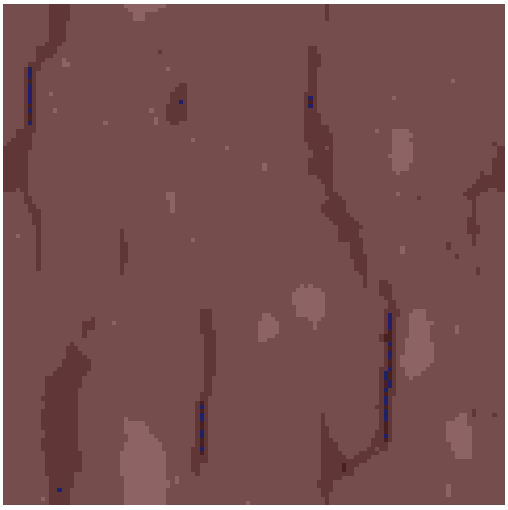

Figure 3.28: 2 ML of InAs grown on InGaAs after at a rate of 0.4 ML/s. A second wetting layer has almost fully formed but fractures have appeared in the first layer due to an accumulation of strain.

as the growth continues. As we can see in 3.30, not all of them but many of the cracks have connected in order to more properly define the borders of what appear to be quantum wires. This illustrates well the Stranski-Krastanow growth mode since during the initial growth, at least one full wetting layer is deposited before

the formation of any 3-dimensional structures occurs. The next examples illustrate a larger critical thickness.

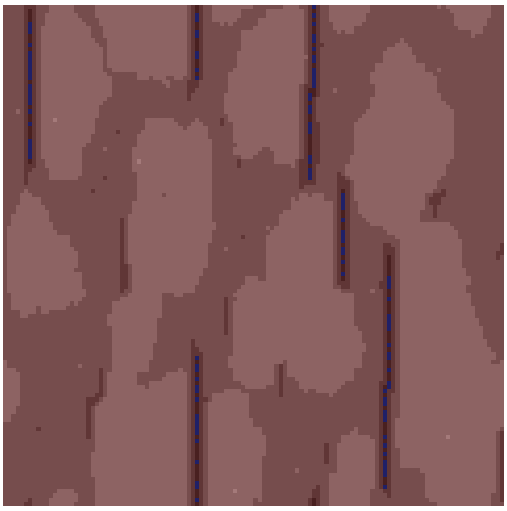

Figure 3.29: 2.5 ML of InAs grown on InGaAs after at a rate of 0.4 ML/s. Many cracks have formed in the InAs and are beginning to propagate.

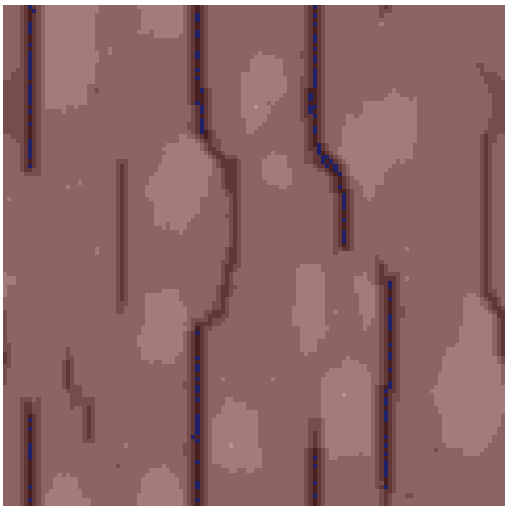

Figure 3.30: 3 ML of InAs grown on InGaAs after at a rate of 0.4 ML/s. Some cracks in the deposited material have connected to each other to form wires.

The growth was continued up to a film thickness of 5 ML, followed by a 10 s annealing period. For this simulated annealing process, we assume that the bond strengths remain unchanged. In reality however, this is likely not the case due to a change in the equilibrium crystal shape under no group III deposition, whether or not the surface reconstruction changes. The final 2-dimensional height profile is shown in 3.31 where we can see wires with some of the features mentioned in the last section such as the splitting of wires and an uneven size distribution. Here we can see that two of the "fractures" on the right side of figure 3.30 have merged and that certain regions of the underlying substrate have been exposed.

To illustrate the effect that bonding strengths have on the critical thickness and the size of the wires, three additional simulations labeled S2 through S4 were run using the energies shown in table 3.3 along with their corresponding surface energies in table 3.4.

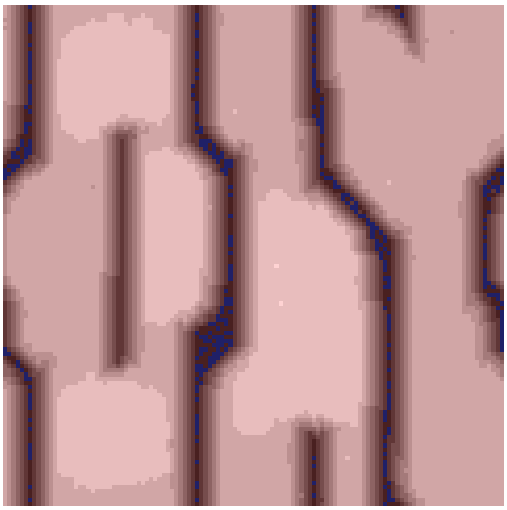

Figure 3.31: Topography of the wires obtained after the deposition of 5 ML of InAs on InGaAs followed by a 10 s annealing period.

E_{bond} (eV)	ECS	S1	S2	S3	S4
a_1	+0.002	-0.385	-0.382	-0.382	-0.382
a_2	+0.237	-0.150	-0.183	-0.203	-0.153
a_3	-0.227	-0.521	-0.417	-0.337	-0.337
b_1	-0.357	-0.274	-0.312	-0.337	-0.325
b_2	-0.474	-0.391	-0.412	-0.427	-0.439
c	-0.233	-0.067	-0.071	-0.073	-0.067

Table 3.3: First and second nearest neighbor bond strengths based on the equilibrium crystal shape in [8] and the ones used for the simulations in this section.

Γ (eV)	ECS	S1	S2	S3	S4
Γ_{001}	1.89	1.85	1.87	1.87	1.87
Γ_{100}	1.89	2.00	2.15	2.26	2.20
$\Gamma_{\bar{1}11}$	2.35	2.37	2.39	2.39	2.38
Γ_{001}	2.12	2.13	2.19	2.21	2.15
Γ_{001}	1.18	1.07	1.15	1.20	1.17
Γ_{001}	1.18	1.07	1.15	1.20	1.17

Table 3.4: The surface energy per surface atom for various facets based on the equilibrium crystal shape in [8] and based on the bond strengths used for the simulations in this section.

Simulation S2 has stronger bonds in both the a_2 and b_1 direction[13] and as a result in figure 3.33, the wires are wider as we would expect. Figure 3.32 shows that fractures in the wetting layer begin to appear after 2.5 ML which is later than the previous case and in the next case, this occurs after the deposition of 5 ML for the third simulation S3 as we can see in figure 3.34, indicating that the critical thickness has increased. As the substrate is annealed for 10 seconds, we can see in figure 3.35 that the fractures have propagated. Presumably, these would lead to the formation of full wires if a thicker film had been grown.

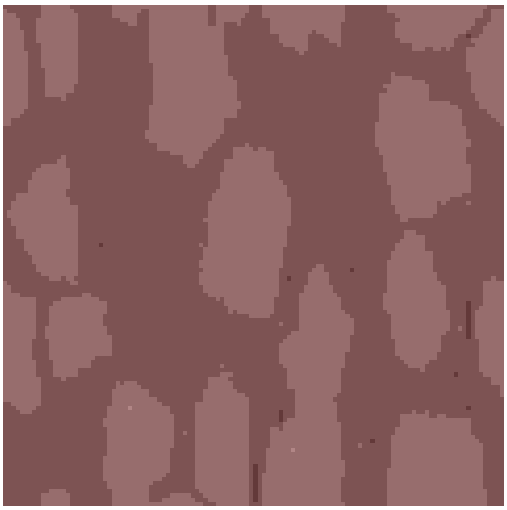

Figure 3.32: Results of simulation S2 after the deposition of 2.5 ML.

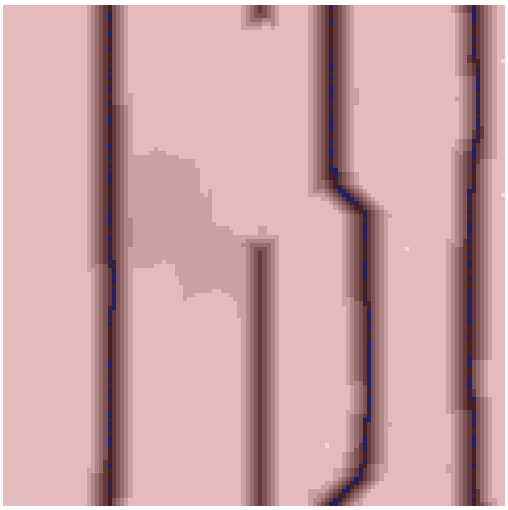

Figure 3.33: Results of simulation S2 after the deposition of 5 ML and a 10 s annealing period.

Finally, figure 3.36 shows the results of the fourth simulation, S4, where only the strength of the bonds in the b_1 and b_2 directions has been increased. Although this has little effect on the width of the wires, the area of the exposed substrate is significantly greater and gives the wires an appearance more similar to those in the SEM results in chapter 2.2. This may indicate that these bonding strengths more accurately model the growth of InAs quantum wires. This section nicely shows that although deriving bond strengths from the surface energies in the literature has lead to formation of wires that are significantly smaller than those observed experimentally, that is, about 25-30 atoms wide as opposed to 45-55, this discrepancy can be attributed to a fairly small discrepancy in the bond strengths and it is in fact possible to simulate the formation of wide quantum wires.

[13]The bonds in the c direction are also stronger as we continue to apply the restriction $c = (a_1 + a_2)/8$.

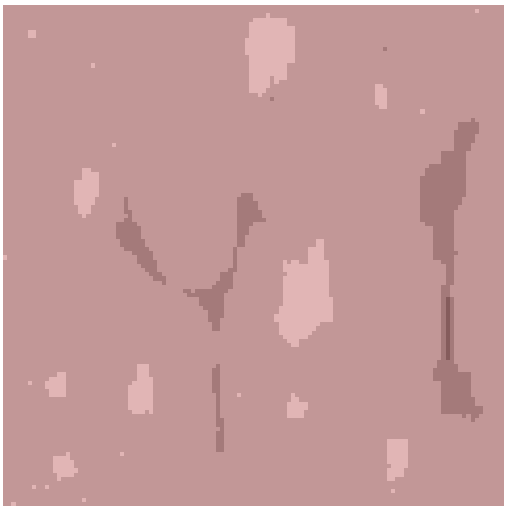

Figure 3.34: Results of simulation S3 after the deposition of 5 ML before the annealing period.

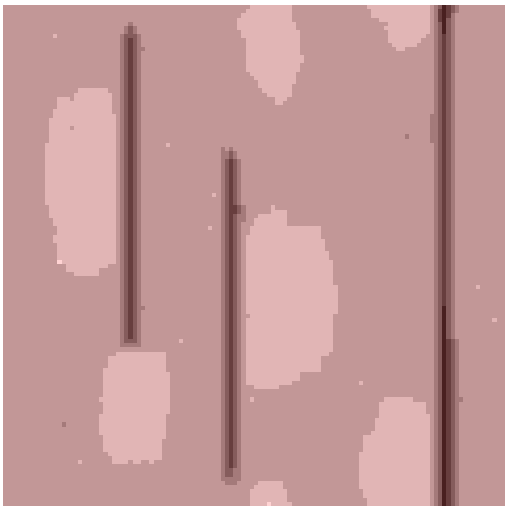

Figure 3.35: Results of simulation S3 after the deposition of 5 ML and the 10 s annealing period.

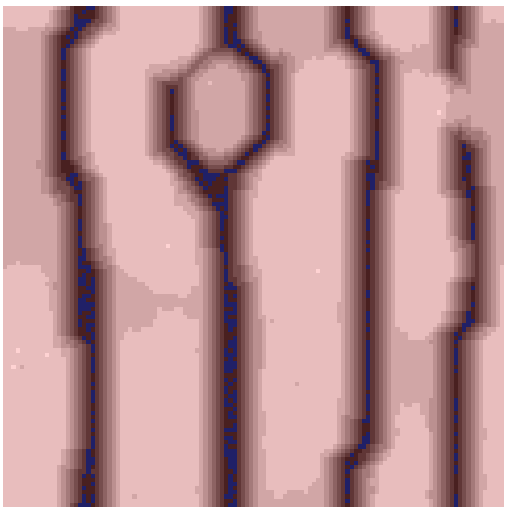

Figure 3.36: Results of simulation S4 after the deposition of 5 ML and the 10 s annealing period.

3.6.6 The Effect of Atomic Steps

Using the shifted periodic boundary conditions described earlier, growth can be simulated on vicinal substrates with the desired number of steps. Given a deposition rate that is slow enough, step flow can occur and all the deposited atoms would migrate to step edges without forming 2-dimensional islands on the terraces. Under ideal conditions, during heteroepitaxial deposition this should force the new material

to first accumulate along the step and help the nucleation of the wires. Figure 3.37 shows an InGaAs substrate with perfectly straight steps with a length of 24 atoms. This value was chosen as the lower end of the width of the wires grown with the bonding strengths described in section 3.6.2. The resulting wires from the growth on this substrate are illustrated in figure 3.38. Somewhat surprisingly, the wires actually grew perfectly aligned with the steps and this result has been observed several times. This demonstrates clearly that the theory of improving the size distribution of quantum wires using an off-cut substrate is at least plausible, depending on the accuracy of our model. Figures 3.39 and 3.40 show the same growth profile except on steps that are 30 atoms long, the upper end of the width of the wires. Here we see that the wire distribution is fairly uniform except for one defect. This may be due to a deposition rate which is a bit too slow to prevent the formation of 2D islands on the terraces which can lead to the formation of 3D islands away from the step edge. Naturally, improving the wire size distribution relies a fair bit on achieving step flow growth. However, under normal circumstances as demonstrated in section 3.5.2 the surface steps do not remain perfectly straight and of even length through the deposition of lattice-matched material nor is it likely for the substrate to arrive as such from the manufacturer. For this reason, other wire growths were simulated after an initial deposition of 10 ML of InGaAs.

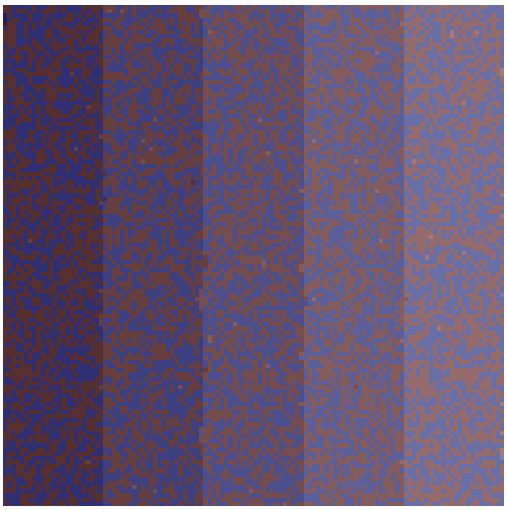

Figure 3.37: Topography of perfectly straight 24-atom wide steps of InGaAs.

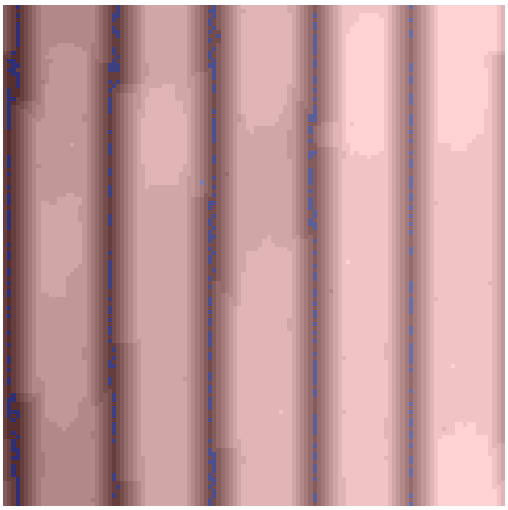

Figure 3.38: InAs quantum wires grown on perfectly straight 24-atom wide steps after the deposition of 5 ML.

Figures 3.41 through 3.44 show the results of such simulations. Each pair of

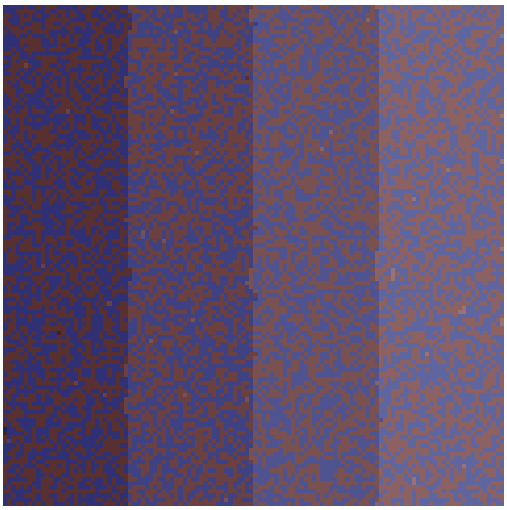

Figure 3.39: Topography of perfectly straight 30-atom wide steps of InGaAs.

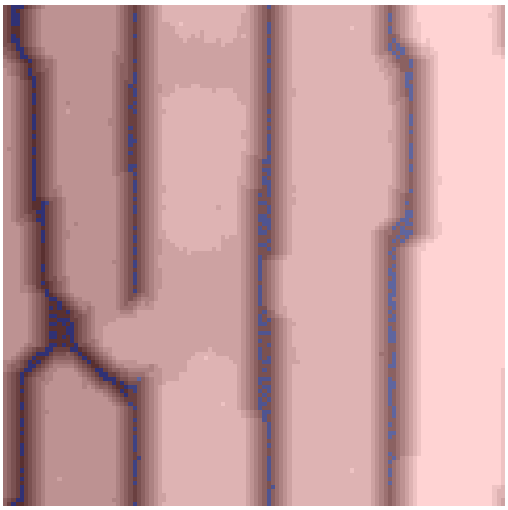

Figure 3.40: InAs quantum wires grown on perfectly straight 30-atom wide steps after the deposition of 5 ML.

images is the result of the growth of 10 ML of InGaAs at 1 ML/s onto an off-cut substrate with a step length of 24 atoms and 30 atoms, followed by a 10 second annealing period. Then the deposition of 5 ML of InAs is performed at a rate of 0.4 ML/s followed by a final 10 s annealing period. The thickness of the deposited ternary alloy was hopefully chosen large enough to achieve an equilibrium step roughness in order to simulate the effect of depositing the relatively thick barrier layer of InGaAlAs required for the confinement of the quantum wires. Although step flow growth was not achieved in either of these simulations, the steps are fairly smooth and mostly because of the annealing period as is shown below. The wires in figure 3.42 are not very uniform whereas those in figure 3.44 are quite uniform. This is an indication that it should be possible to improve the size distribution of quantum wires by growing on off-cut substrates given that the step length and therefore the off-cut angle is chosen correctly. It is important however not to jump to conclusion too quickly given the small sample size here.

However, the right conditions must be met to have proper nucleation along the step edges. The conditions described here (growth rates, temperature, etc.) are based on our physical experimental conditions but are applied to 30-atom wide steps which correspond to a 1.35° off-cut angle rather than a 0.9° angle. This does not indicate that a greater off-cut angle should be used but that the experimental

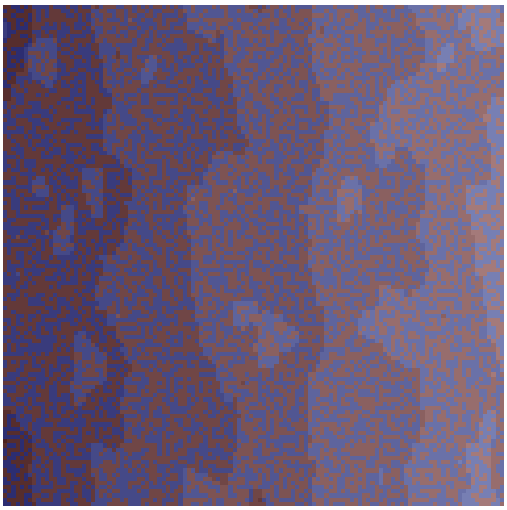

Figure 3.41: Topography of the 24-atom wide stepped surface after the deposition of 10 ML of InGaAs at 1 ML/s followed by a 10 s annealing period.

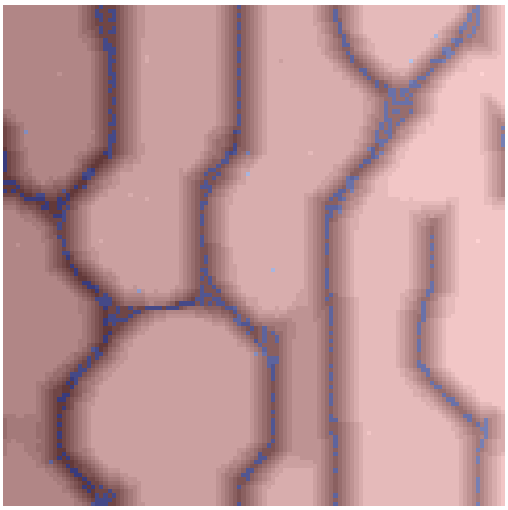

Figure 3.42: InAs quantum wires grown on 24-atom wide steps after the deposition of 10 ML of InGaAs at 1 ML/s.

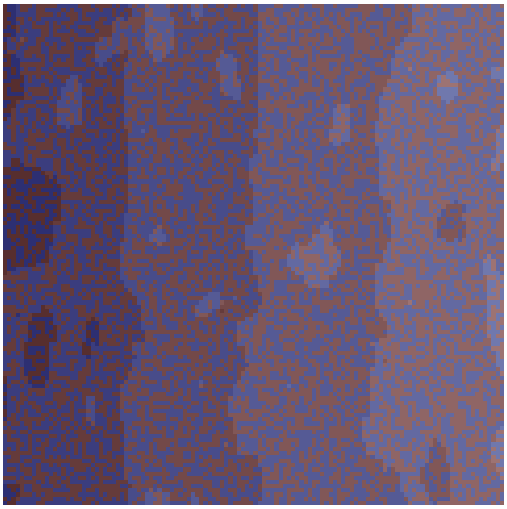

Figure 3.43: Topography of the 30-atom wide stepped surface after the deposition of 10 ML of InGaAs at 1 ML/s followed by a 10 s annealing period.

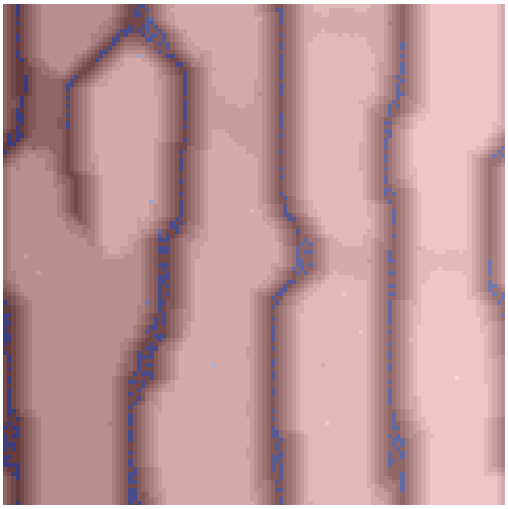

Figure 3.44: InAs quantum wires grown on 30-atom wide steps after the deposition of 10 ML of InGaAs at 1 ML/s.

conditions may not be optimal for proper step-flow growth as they (almost) are in these simulations. Perhaps more importantly, our model still requires refining, considering that it only predicts the formation of (111) and (001) facets around the cross-section of the quantum wires whereas the wires observed experimentally have

significantly shallower facets as can be see in the micrographs of section 2.6. One interesting observation to be made here however is that the steps become fairly smooth after the annealing process. Figures 3.45 and 3.46 show the topography of the substrate before the annealing process and we can see a remarkable difference. This phenomenon is also demonstrated by the rapid rise in RHEED intensity observed at the 20 s mark in figure 3.13 of section 3.5.2. This means that perhaps a combination of annealing conditions and slow deposition could be applied after the deposition of the relatively thick (around 170 ML for 50 nm) barrier layer without having to reduce the overall deposition rate. It should be mentioned at this point that the simulated RHEED intensities rise more quickly after the deposition is halted than observed experimentally (see [42] or [41]), possibly indicating an important discrepancy.

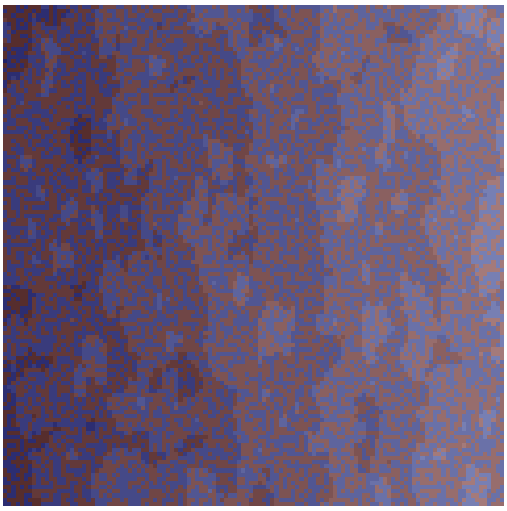

Figure 3.45: Rough surface immediately after the deposition of InGaAs on 24-atom wide steps at 1 ML/s.

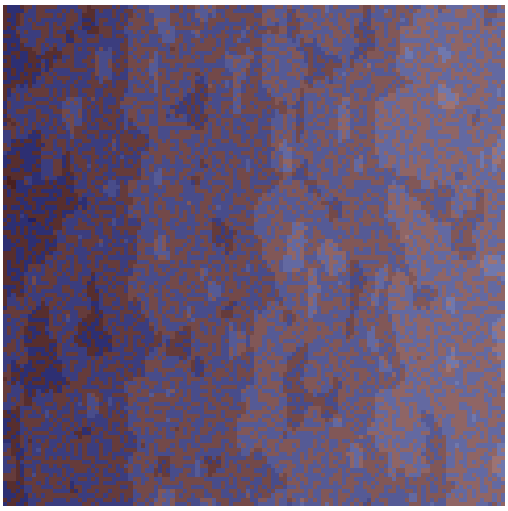

Figure 3.46: Rough surface immediately after the deposition of InGaAs on 30-atom wide steps at 1 ML/s.

Nonetheless, these result are useful as they strongly indicate that the steps grown under out experimental conditions were very unlikely to be straight. The undulations in the steps would explain quite clearly why it is not possible to resolve them using HRSTEM, the reason being that there are no discrete steps along the entire thickness of the TEM sample, making it impossible to resolve a change in intensity from one atomic column to the next.

3.6.7 Buried Quantum Wires

With the intention of reproducing the fluctuations in In concentration above the wires as seen in figure 2.16 from section 2.5, simulations were run where InGaAs was deposited onto the InAs wires. Figure 3.47 shows an artificial (002) dark field image generated from the results. This was done by summing the number of In atoms n_{In} and the number of Ga atoms n_{Ga} in a 40 atom thick cross section and using equation (3.65) where 49, 31 and 33 are the atomic numbers of In, Ga and As, and N is the total number of atoms in the cross section (40), in order to obtain the image intensity for each pixel. This is basically the average atomic number of the group III atoms subtracted by the atomic number of the group V atoms (As), squared, and is based on the contrast mechanism for the (002) spot described in section 1.4 ($I \propto F^2(002) \propto (f_{III}(\theta) - f_V(\theta))^2$). We again assume that the atomic form factor is equal to the atomic number of the atom which is a common approximation [10].

$$I = \left(\frac{49 n_{In}}{N} + \frac{31 n_{Ga}}{N} - 33 \right)^2 \tag{3.65}$$

The image does not reveal a particularly strong increase in In content above the wire[14] but does however show a strong depletion of In content between the wires. This is due to the large amount of compressive strain between the wires where it is very energetically unfavorable for the In atoms to stay, which is of course the reason the wires formed in the first place. The GaAs however, with its smaller lattice constant, compensates for this compressive strain and is much more likely to remain in these crevices if it happens to migrate there. This leads to clear dark bands between the wires where the concentration of In is low. Finally, figure 3.48 is the same image but blurred using a Gaussian filter with a standard deviation of 1 pixel. This simply helps discern the intensity fluctuations. It is important to mention that in order for enough diffusion to occur to allow this concentration segregation, the ternary alloy was deposited onto the wires at a deposition rate of 0.04 ML/s which is much lower than the experimental rate. This likely reveals a discrepancy in our model.

[14]Remember that brighter regions indicate a larger concentration of In.

Figure 3.47: Artificial (002) dark field image obtained from the simulated deposition of InGaAs on top of InAs wires.

Figure 3.48: Blurred version of figure 3.47 using a Gaussian filter with a standard deviation of 1 pixel.

Chapter 4

Conclusion

4.1 Conclusion

InAs quantum wires were successfully grown on InGaAlAs lattice-matched to InP using molecular beam epitaxy following the ideal growth parameters determined by my predecessor and former Ph.D. student, Dr. Kai Cui. The morphology of the resulting nanoscale structures grown at the lower experimental temperature of 520°C was a dense array of flat elongated islands referred to as wires, based on observations using secondary electron scanning electron microscopy (SEM). Although dense, their shape and size were considerably variable. Many wires contained bifurcations and some presented larger dot-like features adding to their irregularity. With the intention of improving their size distribution, that is, narrowing their size distribution in order to hopefully enhance their photoluminescent capabilities for use in near infrared lasers required by the telecommunications industry, thin films were grown on vicinal substrates. An angle of 0.9° towards the (110) direction was selected for the off-cut of these substrates in order to favor uniform nucleation on atomic steps with a length matching the average separation of wires grown on nominally flat substrates which we refer to as the natural separation of the wires. Based on the analysis of images obtained by SEM, a statistically significant improvement or narrowing of the size distribution of the wires grown on off-cut

substrates was observed relative to those grown on nominal InP(001) substrates, although the improvement was modest next to the anticipated results based on work done by other researchers. The measured improvement in the first case was from 7.0 ± 0.1 nm to 5.9 ± 0.1 nm and in the second case the narrowing was from 5.5 ± 0.1 nm to 4.9 ± 0.1 nm.

Other parameters such as the aluminum content of the quaternary boundary layer on which the InAs quantum wires were grown and the temperature of the growth were also varied to measured their effect. The SEM results revealed a decrease in the average wire spacing from about 24.4 ± 0.1 nm to 21.3 ± 0.1 nm with an increase of the aluminum content from 10% to 20% in the two compounds, $In_{0.53}Ga_{0.37}Al_{0.10}As$ and $In_{0.53}Ga_{0.27}Al_{0.20}As$. Although this result is interesting, it is not the primary interest of this investigation. Experimental growths were also conducted at a temperature of 535°C to explore its effect. At this temperature, some of the samples displayed unexpected behavior whereby the deposited material began to coalesce and form larger dot structures while seemingly depleting the InAs from the nearby wires. This effect was strong on two of the four samples grown at this temperature and weakly pronounced on another, irrespective on off-cut angle. This phenomenon was attributed to a possible undesired change in the annealing conditions at the end of the growth since little attention was paid to cooling down the sample quickly. This idea is supported by the fact that the surface reconstruction is expected to change once the deposition of the group III element (In) is halted which is likely to affect the energetically favorable structure and the fact that this only occurred on the samples grown at the hotter experiment temperature at which surface diffusion occurs more readily. Our theory that this is caused by annealing is further supported by the observation of a significant difference between the surface wires, grown for the sole purpose of SEM characterization, and the buried wires , more relevant to the production of devices, based on transmission electron microscopy (TEM) investigations. No significant conclusions can be made based on the measured size distribution of the wires grown at this temperature. An attempt was also made to identify the location of atomic steps relative to the quantum wires grown of off-cut substrates using HRSTEM but without success for reasons determined by simulations.

In order to further understand the nucleation and assembly process of these quantum wires, a kinetic Monte Carlo model was fully developed as part of this work based on models from other research groups. The model consists of a 2+1-dimensional[1] solid-on-solid[2] kinetic Monte Carlo simulation defined by a 3-dimensional cubic lattice of atoms. It makes use of the cubic lattice to represent the group III atoms of a III-V compound semiconductor under the assumption that epitaxial growth of such systems is strictly limited by the deposition of group III atoms and that the effect of group V atoms can be incorporated into the bond structure of these atoms. The algorithm features the simulation of four distinct compounds, InAs, GaAs, InP and AlAs (although only the first two are presented in this work), and incorporates full 3D strain calculations into the atomic bonding model in order to properly simulate the formation of lattice-mismatched 3D heterostructures which form through the Stranski-Krastanow strain relief mechanism. Other features of the model include shifted periodic boundary conditions for the proper emulation of the effect of surface steps on the growth of thin films and an anisotropic bonding model calibrated using the equilibrium crystal structure of GaAs to simulate the formation of quantum wires.

Using this model, we have demonstrated the principle of predicting the equilibrium shape of a structure based on a simple bond model whereby contradicting the longstanding idea that InAs quantum wires form due to diffusion anisotropy. We have to some extent demonstrated how our model is able to successfully simulate the formation of InAs quantum wires as well as the effect of various parameters on the outcome of our model. Such effects include that of the stiffness constant on the average size of 3D heterostructures, the effect that bond anisotropy has on the type of structure that is formed and the effect of bond strengths on the dimensions of quantum wires. We've also observed how bond strengths affect the critical thickness of the onset of 3D structure formation and to some extent the effect of an off-cut substrate on the growth and control of quantum wires. Finally, a preliminary demonstration of the concentration fluctuations of indium above InAs wires is also presented in this work.

[1] This refers to the fact that the model considers the surface (2D) of a undulated (+1) substrate.

[2] A solid-on-solid model only considers the diffusion of the top-most atoms and does not allow the formation of overhangs.

4.2 Future Work

On the experimental side, there is still much work to do in order to greatly improve the size distribution of self-assembled quantum wires as well as, consequently, their photoluminescent properties. Although no photoluminescence measurements were made as part of this work, we do intend on comparing the spectral output of our various samples to see if the slight improvement in the spacing distribution of our wires has resulted in an improvement in their light producing qualities.

As far as growth experiments are concerned, it would definitely be worthwhile to perform the growth of quantum wires on vicinal substrates while observing RHEED intensity fluctuations. This would allow one to ensure proper step flow growth which could very well lead to an important improvement in the size distribution of the wires. Other deposition schemes in the aim of producing straight and uniform atomic steps should be investigated as well.

In order to get a better idea of what is happening on the surface of the substrate, various different experiments could be performed. Scanning tunneling microscopy (STM) seems like the most promising method to observe the distribution of the group III atoms on the surface at different stages of growth. By measuring the distribution of adatoms, it may be possible to improve the bonding model based on the assumption that their energy distribution should follow a Boltzmann distribution.

Grosse *et al.* have done some interesting work developing a kinetic Monte Carlo (kMC) model of surface diffusion that actually uses a face centered cubic (FCC) lattice which better matches the configuration of group III atoms in the zinc blende crystal structure. Based on our readings, they have yet to apply strain calculations to this model and this could potentially make much more realistic predictions concerning the growth of InAs quantum wires along with other quantum structures. They have also done work on combining kMC simulations with density functional theory (DFT) calculations in order to produce a more accurate diffusion model. In fact, they show that In atoms are often found in pairs on the substrate due to the surface reconstruction and how it is easier for those pairs to stick to islands along

the $(\bar{1}10)$ direction than the (110) direction because of how As atoms interact with them and seem to "lock" them into place. This observation could potentially be incorporated into an anisotropic bonding model such as the one presented here.

Concerning improvements to our own model, the bonding strengths still required a fair bit of testing in order to find ideal values which form quantum wires more similar to those observed experimentally. The efficiency of the strain calculations could certainly benefit from the implementation of a multigrid algorithm such as the one described in [43]. The Fourier component of this algorithm may however not be compatible with our simulations since we make use of shifted periodic conditions whereas Fourier algorithms are typically only applied to systems with a regular periodicity. Finally, the spring model developed here should be modified to take into account the tetragonal shape of the unit cell we used in our model. This could have a significant impact on the shape and size of the simulated InAs quantum wires, and should be fairly simple to implement.

Appendix A

Tree Structure

In order to efficiently select an event among the tens of thousands of possibilities in the kinetic Monte Carlo simulation in this work, it is necessary to store the list of all possible events, more specifically their rates, in a data structure such as a binary tree. As mentioned in section 3.2.1, a binary tree reduces the search time from $O(N)$ to $O(\log_2(N))$ which means that searching among a list of $120 \cdot 120 \cdot 4 = 57600$ possible hopping events for a 120 by 120 simulated surface should require approximately 16 comparison operations as opposed to 28800 on average using a simple list or array. For this reason, a custom binary tree data structure was developed based on the AVL tree [30]. This particular tree algorithm was chosen among others mainly for its simplicity.

The binary tree is illustrated in figures A.1 through A.3. It consists of nodes which are each connected to two other child nodes and a parent node. All the nodes (except for the root node) are treated identically so that the entire algorithm operates recursively. Although most of the operations described here apply to binary trees in general, details such as keeping track of the sum of hopping rates $ksum$ are specific to this implementation. It is important to note that the variable k is used for the rate instead of R to match the algorithm's implementation.

When a binary tree is initialized, a first node called the root node is produced. Like every node, it contains an identification number n which refers to a specific

hopping direction of a particular atom (an event), a hopping rate k which relates to that specific event and $ksum$ which contains the recursive sum of all the rates of the child nodes below it including its own value k. It also contains two "pointers"[1] which basically keep track of the identification numbers of the so called child nodes to its left and to its right. If there are no nodes below a particular node, its left and right pointers are simply -1. Figure A.1 illustrates the process of adding a new node to the tree. For simplicity, in this work's implementation of the binary tree, new nodes are always added to the rightmost node of a tree. The addition of a new node is indicated by the color blue in the following diagrams and changes made to other nodes are highlighted in red. In this case, adding node number 2 ($n = 2$) changes the right pointer of node 1 and requires the running sum $ksum$ to be updated.

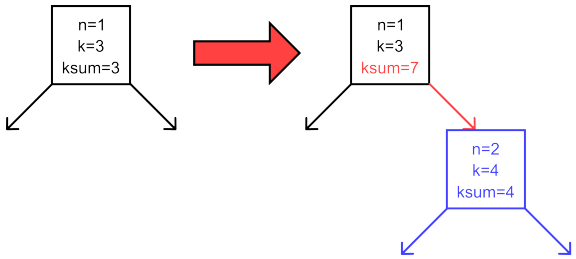

Figure A.1: The process of adding a new node to a binary tree.

In order for a binary tree to remain efficient, it must be balanced, otherwise it will be nothing more than a list of nodes with right child nodes. A balanced tree is a three that for each node, the height of the left branch is different than the height of the right branch by no more than one. Figure A.2 shows the process of balancing a binary tree after an additional node has caused it to become unbalanced. After the addition of node 3, which affects the value of $ksum$ of nodes 1 and 2 as well as the right pointer of node 2, the height of the right branch of node 1 is 2 whereas that of the left branch is 0. This difference of 2 indicates that the tree is unbalanced. It can be balanced by shuffling pointers around as indicated in the figure. The left pointer of node 2 becomes the root node and the root node's right pointer is cleared. After this rotation, the value of $ksum$ for both nodes 1 and 2 must be updated to remain accurate. This balancing process is applied whenever a new node is added. Although there exist more sophisticated and efficient balancing

[1]Since the algorithm was implemented in Java, these pointers are actually the indices of elements in an `ArrayList`.

algorithms, that of the AVL tree is fairly easy to implement and since our binary tree is used to look up values much more often than to add (and remove) nodes, such an improvement in efficiency was deemed unnecessary.

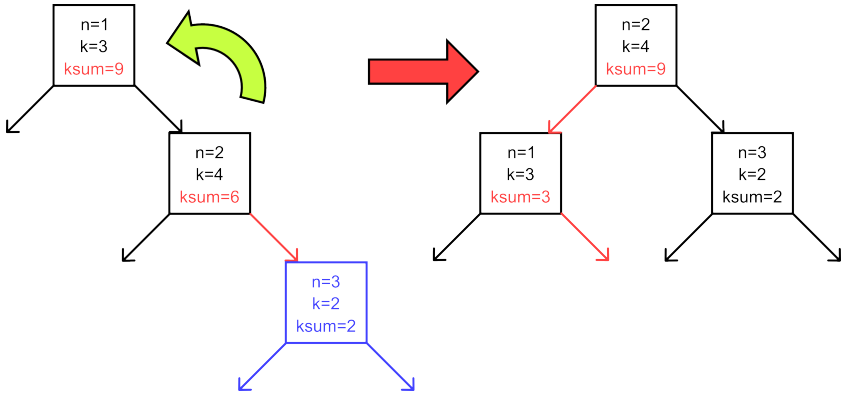

Figure A.2: The process of balancing a small binary tree following the addition of a new node.

Figure A.3 shows a similar balancing operation but performed on a larger tree in order to demonstrate some of the extra shuffling that may be involved as well as other implications of binary trees. Here we see that the addition of node 6 affects the right pointer of node 5 as well as the value of *ksum* for all its parent nodes up to the root node, that is, nodes 5, 4 and 2. Here we can see that once again, the root node is unbalanced since the length of the right branch is 3 and that of the left branch is 1. This operation is a bit more complex than the previous one because when node 4 is rotated and gains node 2 as a left pointer, node 3 is left parentless. For this reason, node 3 is assigned as the right pointer of node 2. Once again, the running sums of node 2 and 4 must be adjusted after this rearrangement. It is worth pointing out here that through these balancing operations, the order of the nodes from left to right always remains the same and this is in fact the purpose of most binary tree structures.

Lastly, it is important to understand not only how the tree is balanced but how to search through it since this is its primary purpose. Just like in the case of the running sum in figure 3.3, after choosing a random number x between 0 and R_{total} or *ksum* of the root node in this case, we need to find the value nearest to x but greater than x. Using as an example the tree on the right side of figure A.3, we know that if we pick a random value less than 3, the chosen event should correspond to that of node 1 since 3 is the value of *ksum* of the leftmost node,

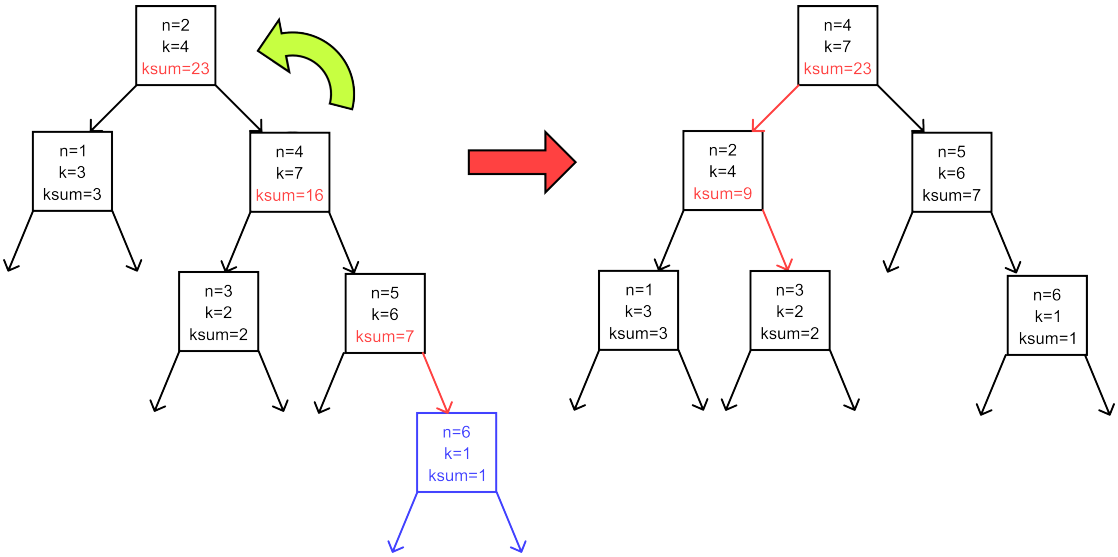

Figure A.3: The process of balancing a larger binary tree following the addition of a new node.

similar to the case of $x < R_1$ in figure 3.3. If x is greater than 3 but less than 7, event 2 should be chosen. If it is greater than 7 but less than 9, event 3 should be chosen. If x is greater than 9 but smaller than 16, event 4 should be selected, and so on. Although this problem could likely be solved in a number of different way, our implementation is as follows.

Starting from the root node, if x is greater than $ksum$ of the left node (which is 0 if there is no left node) yet smaller than the sum of this value and the rate k of the current node (root node), the current node is selected. If x is smaller than $ksum$ of the left node, the above logic is applied to the left node as if it were the root node. The third case is if x is greater than the sum of $ksum$ of the left node and k of the current node, x is decrement by this sum ($x' = x - ksum_{\text{Left}} - k$) and above logic is applied to the right node using the value x' as if it were the root node. It can be quite tricky to wrap one's head around this logic but it works. Keep in mind however that this algorithm will fail if the value of x is ever greater than $ksum$ of the root node.

These two algorithms, that of balancing and of searching, provide a very efficient way of selecting where a random number lies within a list of running sums. One missing process however is the one of removing events (nodes) from

the tree structure. For reasons of simplicity of implementation as well as avoiding the risk of producing immobile atoms, the removal of nodes was not implemented but rather buried atoms simply have a hopping rate of 0. In terms of efficiency, the repercussions of this omission are fairly small since the number of searches for $120 \cdot 120 \cdot 4 \cdot 50 = 2880000$ possible events[2] rather than 57600 only increases the number of searches from $\log_2(57600) = 16$ to $\log_2(2880000) = 21$. The important increase in memory requirements however is not negligible and has in fact caused some issues which should be resolved at some point in the future.

[2]Assuming a substrate thickness of 50 atoms.

Appendix B

Bonding and Surface Energy

In order to use the surface energy values given in [8, 9], it is important to understand how bond strength or bond energy relates to surface energy. This section derives the equation defining the surface energy with respect to the bond energies by using simple 2-dimensional models and the Wulff construction.

First of all, the Wulff construction [44] is used to predict the size of different crystal facets, that is, the equilibrium crystal shape (ECS), based on their surface energy. The diagrams in figure B.1 illustrate how the construction works. The solid black curve is a polar plot of the 1-dimensional surface energy γ and it contains sharp dips at particular angles which lead to the formation of facets. The surface energy of certain particular facet directions are indicated by γ_{01}, γ_{10} and γ_{11}. The construction of the crystal shape is achieved in a similar way to a Wigner-Seitz cell. For each point of the polar plot, a line is drawn perpendicular to the direction from the center of the plot to this point as indicated by the construction lines in the diagrams below. The minimum area (volume in 3D) within these boundaries forms the equilibrium crystal shape.

The diagram on the left indicates the simplest case where the only two important facets are the (10) and (01) facets. In this case we can observe that the length of the top face (01) is proportional to γ_{10} and that of the right face (10) is proportional to γ_{01}, indicating that a lower surface energy leads to a larger face (relative to others).

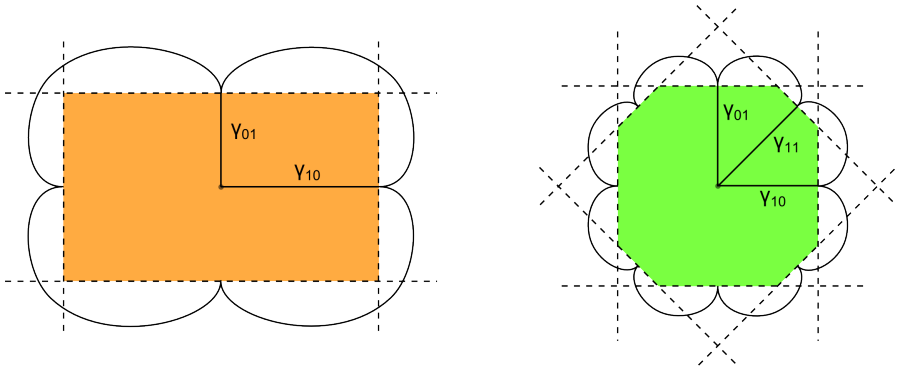

Figure B.1: 2D Wulff construction for two different materials.

If we build a simple bonding model consisting of a square lattice with bonds only between first nearest neighbors as illustrated in figure B.2, we can calculate the total bonding energy of a crystal of given dimensions.

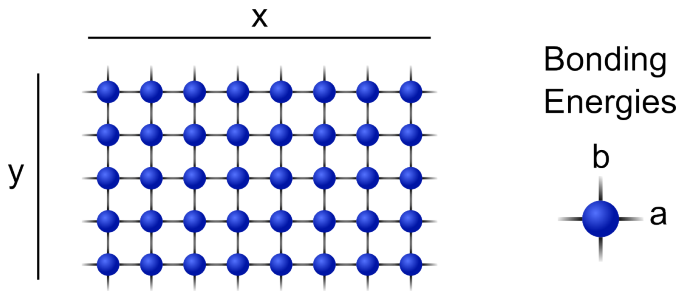

Figure B.2: A square lattice with first nearest neighbor bonds of strength a and b. Only horizontal and crystal facets are of importance.

Let a and b be the bonding energies in the x and y directions, respectively, and the dimensions of a crystal to be x by y in atomic units as indicated in figure B.2. The total number of horizontal bonds (not dangling) is then given by $(x-1)y$ and the number of vertical bonds is given by $(y-1)x$ or 35 and 32 in the illustration. The total bonding energy E is therefore given by equation (B.1) which can be broken down into a bulk bonding energy term[1] and a surface term.

$$E = (x-1)ya + (y-1)xb \tag{B.1}$$

$$= xy(a+b) - xb - ya \tag{B.2}$$

$$= E_{\text{bulk}} - xb - ya \tag{B.3}$$

[1]The bulk term represents the bonding energy of the solid in the case where $x \gg 1$ and $y \gg 1$.

To find the minimum energy configuration of x and y for a given area $V = xy$, we express the total bonding energy E in terms of x (variable) and V (constant), and find a minimum as shown in equations (B.5) through (B.8). At this point it is worth noting that bond energies must be negative in order for the extremum below to be a minimum and not a maximum, and this is physically accurate. It is also worth mentioning that the following derivations could equally be done by keeping the number of atoms N constant instead of the area V.

$$V = xy \tag{B.4}$$

$$E = V(a+b) - xb - \frac{V}{x}a \tag{B.5}$$

$$\left.\frac{dE}{dx}\right|_V = -b + \frac{Va}{x^2} = 0 \tag{B.6}$$

$$x = \sqrt{\frac{Va}{b}}; \quad y = \sqrt{\frac{Vb}{a}} \tag{B.7}$$

$$\frac{x}{y} = \frac{a}{b} \tag{B.8}$$

The ratio above is between the number of atoms on the top face and the side face but not necessarily the ratio of the facet lengths L_x and L_y unless the lattice is cubic. The general case is shown in (B.10) where l_x is the width of each atom and l_y is their height. This is directly related to the ratio of surface energies γ_{10} and γ_{01} as we can see from figure B.1. Knowing this ratio and the definition[2] of the surface energy in (B.11) where $E_{(10)\text{facet}}$ is the total surface energy of the (10) facet, we can infer that $E_{(10)bonds}$, the energy of the broken bonds per surface atom, is equal to a. The broken bonds per surface atom on the other facet is then b. The factor of two is related to the fact that a solid has two opposing faces, (10) and $(\bar{1}0)$ for example.

[2]Keep in mind that the definition should actually have an additional negative sign since bonds are negative and surface energies are positive but they are excluded to avoid confusion.

$$L_x = l_x x; \quad L_y = l_y y \tag{B.9}$$

$$\frac{L_x}{L_y} = \frac{l_x x}{l_y y} = \frac{l_x a}{l_y b} = \frac{\gamma_{10}}{\gamma_{01}} \tag{B.10}$$

$$\gamma_{10} \equiv \frac{E_{(10)\text{facet}}}{L_{(10)\text{facet}}} = \frac{y E_{(10)bonds}/2}{l_y y} = \frac{E_{(10)bonds}}{2l_y} \tag{B.11}$$

$$\gamma_{01} \equiv \frac{E_{(01)\text{facet}}}{L_{(01)\text{facet}}} = \frac{x E_{(01)bonds}/2}{l_x x} = \frac{E_{(01)bonds}}{2l_x} \tag{B.12}$$

$$\frac{\gamma_{10}}{\gamma_{01}} = \frac{E_{(10)bonds} 2l_x}{E_{(01)bonds} 2l_y} = \frac{l_x a}{l_y b} \tag{B.13}$$

$$E_{(10)bonds} = a; \quad E_{(01)bonds} = b \tag{B.14}$$

$$\gamma_{10} = \frac{a}{2l_y}; \quad \gamma_{01} = \frac{b}{2l_x} \tag{B.15}$$

This teaches us two things. The first is how the surface energy can be directly related to bond strengths which allows them to be determined using values of γ from the literature as indicated by equation (B.15). The second is how to properly count broken bonds on a facet. It may seem trivial in this simple case but it is important not to consider the bonds parallel to the surface of interest even though they would be broken if we were to remove an atomic layer atom by atom. Figure B.3 highlights in blue the exposed bond on the (01) surface and in red the exposed bond on the (10) surface. How to properly count surface broken bonds is less obvious in the second case which follows.

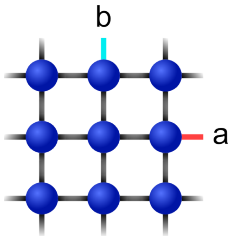

Figure B.3: Broken bonds required for proper bond counting.

Figure B.4 shows a more complicated bonding model where horizontal and vertical bonds both have an energy of a and diagonal bonds with an energy of c. Because of this new bond, it is energetically favorable to have (11) facets in addition to the (10) and (01) facets in the previous case. It should be noted that

the vertical and horizontal bond strengths were chosen to be equal in order to greatly simplify the problem which implies that $\gamma_{10} = \gamma_{01}$.

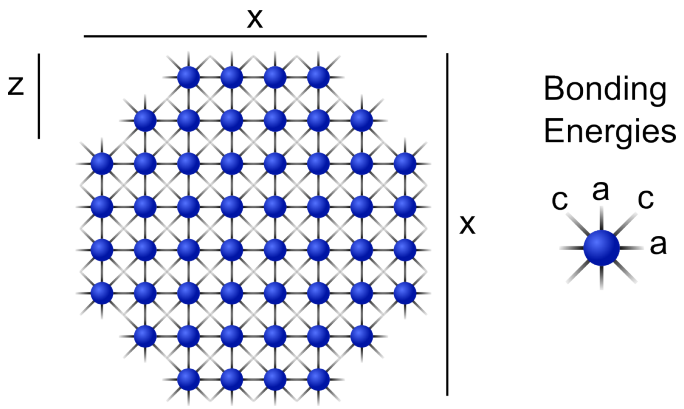

Figure B.4: A square lattice with first and second nearest neighbor bonds of strength a and c. Vertical, horizontal and diagonal facets must be considered.

Based on the problem above, it is fairly obvious how to properly count on the (01) surface as indicated by the blue bonds in figure B.5. However, the case of the (11) facet is less obvious. The red bonds should fairly obviously be considered but the diagonal bond in green is ambiguous. Here we will demonstrate that all four bonds should indeed be counted as broken on the (11) surface.

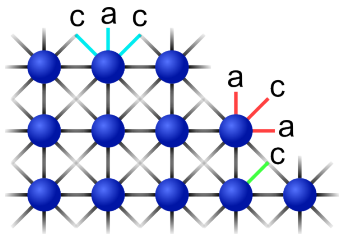

Figure B.5: Broken bonds that may be required for proper bond counting.

By symmetry[3], the height and width of the ECS in units of atoms is the same and denoted by x. The height of the missing corner is given by z which means that the length of the (11) facet is $z\sqrt{2}$ for a cubic crystal($l_x = l_y$). The bond energy ignoring the missing corners is given by (B.16) and if we consider them the expression becomes equation (B.18).

[3]Since the horizontal and vertical bonds are of equal strength, there is no distinction between the two directions.

$$E_{\text{square}} = ax(x-1) + a(x-1)x + 2c(x-1)(x-1) \tag{B.16}$$

$$= 2ax(x-1) + 2c(x-1)^2 \tag{B.17}$$

$$E = 2ax(x-1) + 2c(x-1)^2 - 4\big(az(z+1) + cz^2\big) \tag{B.18}$$

$$= 2(a+c)(x^2 - 2z(z+1)) - 2ax - 4cx + 2c + 4cz \tag{B.19}$$

As before, we need to find the expression for the minimum energy for a fixed volume and extract a relationship between x and z. This is solved in equations (B.20) through (B.27).

$$V = x^2 - 2z(z+1) \tag{B.20}$$

$$E = 2(a+c)V - 2ax - 4cx + 2c + 4cz \tag{B.21}$$

$$x = \sqrt{V + 2z(z+1)} \tag{B.22}$$

$$E = 2(a+c)V - (2a+4c)\sqrt{V + 2z(z+1)} + 2c + 4cz \tag{B.23}$$

$$\frac{dE}{dz}\Big|_V = \frac{-(2a+4c)}{2}\frac{4z+2}{\sqrt{V+2z(z+1)}} + 4c = 0 \tag{B.24}$$

$$4c = (a+2c)\cdot\frac{4z+2}{\sqrt{V+2z(z+1)}} \tag{B.25}$$

$$\frac{2c}{a+2c} = \frac{2z+1}{x} \approx \frac{2z}{x} \quad \text{for} \quad 2z \gg 1 \tag{B.26}$$

$$\frac{z}{x} = \frac{c}{a+2c} \tag{B.27}$$

Relating x and z to the surface energies γ_{01} and γ_{11} is a bit trickier but still approachable and demonstrated in the next equations. Assuming that the lattice is cubic $l_x = l_y$, we can first determine the length of the top and diagonal faces, L_x and L_z, relative to the surface energies $\gamma_{10} = \gamma_{01}$ and γ_{11} by using the geometry in figure B.1. The resulting expressions are in (B.28) and (B.29). Their ratio is then expressed in (B.30)[4]. This ratio can also be expressed in terms of x and z in equation (B.31).

[4]It is important to note that L_x and L_z here have the same constant of proportionality which is why it is possible to express their ratio as it is done here.

$$L_x \propto 2(\sqrt{2}\gamma_{11} - \gamma_{01}) \tag{B.28}$$

$$L_z \propto 2(\sqrt{2}\gamma_{01} - \gamma_{11}) \tag{B.29}$$

$$\frac{L_z}{L_x} = \frac{2(\sqrt{2}\gamma_{01} - \gamma_{11})}{2(\sqrt{2}\gamma_{11} - \gamma_{01})} \tag{B.30}$$

$$\frac{L_z}{L_x} = \frac{\sqrt{2}z}{x - 2z} = \frac{\sqrt{2}z/x}{1 - 2z/x} \tag{B.31}$$

$$= \frac{\sqrt{2}\frac{c}{a+2c}}{1 - 2\frac{c}{a+2c}} = \frac{\sqrt{2}c}{a + 2c - 2c} = \frac{\sqrt{2}c}{a} \tag{B.32}$$

The ratios in (B.30) and (B.32) then allow us to relate bond strengths to surface energies in (B.33). Using the definitions in (B.34) and (B.35) and knowing the dangling surface bonds on the (01) facet from figure B.5, we can solve for $E_{(11)bonds}$ and conclude that two a and two c bonds must be considered on the (11) facet as indicated by equation (B.39).

$$\frac{L_z}{L_x} = \frac{\sqrt{2}\gamma_{01} - \gamma_{11}}{\sqrt{2}\gamma_{11} - \gamma_{01}} = \frac{\sqrt{2}c}{a} \tag{B.33}$$

$$\gamma_{01} \equiv \frac{E_{(01)bonds}}{2l_x} = \frac{a + 2c}{2l_x} \tag{B.34}$$

$$\gamma_{11} \equiv \frac{E_{(11)bonds}}{2\sqrt{2}l_x} \tag{B.35}$$

$$\frac{\sqrt{2}c}{a} = \frac{\sqrt{2}E_{(01)bonds}/2l_x - E_{(11)bonds}/2\sqrt{2}l_x}{\sqrt{2}E_{(11)bonds}/2\sqrt{2}l_x - E_{(01)bonds}/2l_x} \tag{B.36}$$

$$= \frac{\sqrt{2}(E_{(01)bonds} - E_{(11)bonds}/2)}{E_{(11)bonds} - E_{(01)bonds}} \tag{B.37}$$

$$= \frac{\sqrt{2}(a + 2c - E_{(11)bonds}/2)}{E_{(11)bonds} - (a + 2c)} \tag{B.38}$$

$$\gamma_{11} = \frac{2a + 2c}{2l_z} = \frac{2a + 2c}{2\sqrt{l_x^2 + l_y^2}} \tag{B.39}$$

This means that to properly count broken bonds on a surface, all dangling bonds including those not attached to the most obvious surface atoms must be considered and bonds between surface atoms should be ignored. Although this

derivation was all done in 2 dimensions, the 3-dimensional case is very similar except that the average area per surface atom of a facet is used instead of the length for calculating the 2D surface energy instead of a 1D surface energy. Figure B.6 shows the bond counting for a (011) facet of an orthorhombic crystal where first, second and third nearest neighbors are considered and colored in red, green and blue, respectively. The right side of the figure shows the two atoms of importance[5], one of which is hidden in the left diagram because it is buried. Both clearly have a distinct broken bond configuration. Equation (B.40) defines the surface energy of the (011) facet where the energies of first, second and third nearest neighbor bonds are represented by the variables a, b and c, assuming that the bonds in all three dimensions are equivalent in energy or strength.

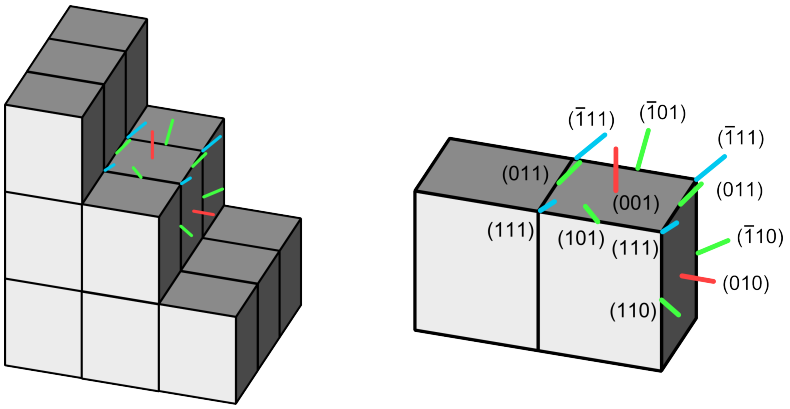

Figure B.6: Crystallographic direction of all unique broken bonds on a (011) surface. The two units on the right are those with unique broken bond configurations.

Figure B.7 shows the case for a (111) facet and the expression for the surface energy is given in equation (B.41). It is worth pointing out that this expression is in disagreement with the one found in [27] as we count an extra c bond, that is, $6c$ rather than $5c$. In this case there are three atom with distinct broken bond configurations as indicated on the right side of the diagram. Note that the bottom (110) bond could be placed just to the left of the (100) bond but that would required a duplicate of the bottom atom from another "unit cell".

$$\gamma_{011} = \frac{2a + 6b + 4c}{2l_x\sqrt{l_y^2 + l_z^2}} \tag{B.40}$$

$$\gamma_{111} = \frac{3a + 6b + 6c}{2\sqrt{l_x^2 l_y^2 + l_x^2 l_z^2 + l_y^2 l_z^2}} \tag{B.41}$$

[5]These two atoms are the only atoms with distinct broken bonds on the periodic facet.

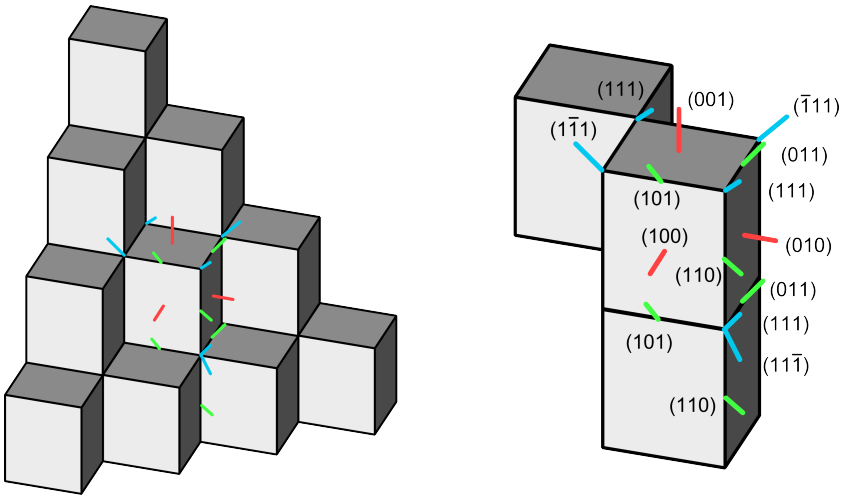

Figure B.7: Crystallographic direction of all unique broken bonds on a (111) surface. The three units on the right are those with unique broken bond configurations.

Bibliography

[1] Miya, T., Terunuma, Y., Hosaka, T. and Miyashita, T. *Ultimate low-loss single-mode fibre at 1.55 μm.* Electronics Letters, **15**(4):106--108, 1979

[2] Griffiths, D. *Introduction to quantum mechanics.* Pearson Prentice Hall, second edition, 2005. ISBN 0-13-111892-7

[3] Noetzel, R. *Self-organized growth of quantum-dot structures.* Semiconductor science and technology, **11**(Semicond. Sci. Technol.):1365--1379, 1996

[4] Salem, B., Olivares, J., Guillot, G., Bremond, G., Brault, J., Monat, C., Gendry, M., Hollinger, G., Hassen, F. and Maaref, H. *Optical properties of self-assembled InAs quantum islands grown on InP(001) vicinal substrates.* Applied Physics Letters, **79**(26):4435, 2001. ISSN 00036951. doi:10.1063/1.1427742

[5] Wohlert, D., Chou, S. and Cheng, K. *Temperature-insensitive photoluminescence above 300 K in strained Ga x In 1-x As multiple quantum wire heterostructures.* Journal of crystal growth, **176**:1162--1166, 1997

[6] Tsao, J. S. *Materials Fundamentals of Molecular Beam epitaxy.* Academic Press, 1993

[7] Däweritz, L. and Hey, R. *Reconstruction and defect structure of vicinal GaAs (001) and Al x Ga 1-x As (001) surfaces during MBE growth.* Surface Science, **236**:15--22, 1990

[8] Moll, N., Kley, a., Pehlke, E. and Scheffler, M. *GaAs equilibrium crystal shape from first principles.* Physical review. B, Condensed matter, **54**(12):8844--8855, 1996. ISSN 0163-1829

[9] Moll, N., Scheffler, M. and Pehlke, E. *Influence of surface stress on the equilibrium shape of strained quantum dots.* Physical Review B, **58**(8):4566--4571, 1998. ISSN 0163-1829. doi:10.1103/PhysRevB.58.4566

[10] Williams, D. B. and Carter, C. B. *Transmission Electron Microscopy.* 2009. ISBN 9780387765006

[11] Tu, Y. and Tersoff, J. *Origin of Apparent Critical Thickness for Island Formation in Heteroepitaxy.* Physical Review Letters, **93**(21):19--22, 2004. ISSN 0031-9007. doi:10.1103/PhysRevLett.93.216101

[12] Grosse, F. and Gyure, M. *Island and Step Morphology in InAs(001) Homoepitaxy.* Physica Status Solidi (B), **234**(1):338--345, 2002. ISSN 0370-1972. doi:10.1002/1521-3951(200211)234:1⟨338::AID-PSSB338⟩3.0.CO;2-F

[13] Gutiérrez, H. R., Cotta, M. a. and de Carvalho, M. M. G. *Faceting evolution during self-assembling of InAs/InP quantum wires.* Applied Physics Letters, **79**(23):3854, 2001. ISSN 00036951. doi:10.1063/1.1424476

[14] Cui, K. *Growth and Characterizations of Semiconductor Quantum Wires.* Ph.D. thesis, 2009

[15] Föll, H. *III-V Semiconductors*, 2013. `http://www.tf.uni-kiel.de/matwis/amat/semitech_en/kap_2/backbone/r2_3_1.html`

[16] Vurgaftman, I., Meyer, J. R. and Ram-Mohan, L. R. *Band parameters for III–V compound semiconductors and their alloys.* Journal of Applied Physics, **89**(11):5815, 2001. ISSN 00218979. doi:10.1063/1.1368156

[17] Molina, S. I., Varela, M., Sales, D. L., Ben, T., Pizarro, J., Galindo, P. L., Fuster, D., Gonzalez, Y., Gonzalez, L. and Pennycook, S. J. *Direct imaging of quantum wires nucleated at diatomic steps.* Applied Physics Letters, **91**(14):143112, 2007. ISSN 00036951. doi:10.1063/1.2790483

[18] *NSM Archive - Physical Properties of Semiconductors*, 2013. `http://www.ioffe.ru/SVA/NSM/Semicond/index.html`

[19] Parry, H., Ashwin, M., Neave, J. and Jones, T. *Growth of InAs/InP(001) nanostructures: The transition from quantum wires to quantum dots.* Journal of Crystal Growth, **278**(1-4):131--135, 2005. ISSN 00220248. doi:10.1016/j.jcrysgro.2005.01.100

[20] Brandt, S. *Data Analysis.* Springer, 3rd edition, 1998. ISBN 0387984984

[21] Cui, K., Robinson, B. J., Thompson, D. a. and Botton, G. a. *InAs quantum wire induced composition modulation in an In[sub 0.53]Ga[sub 0.37]Al[sub 0.10]As barrier layer grown on an InP substrate.* Journal of Applied Physics, **108**(3):034321, 2010. ISSN 00218979. doi:10.1063/1.3460643

[22] Molina, S. I., Ben, T., Sales, D. L., Pizarro, J., Galindo, P. L., Varela, M., Pennycook, S. J., Fuster, D., González, Y. and González, L. *Determination of the strain generated in InAs/InP quantum wires: prediction of nucleation sites.* Nanotechnology, **17**(22):5652--8, 2006. ISSN 0957-4484. doi:10.1088/0957-4484/17/22/020

[23] Tsukamoto, S., Bell, G. and Arakawa, Y. *Heteroepitaxial growth of InAs on GaAs(001) by in situ STM located inside MBE growth chamber.* Microelectronics Journal, **37**(12):1498--1504, 2006. ISSN 00262692. doi: 10.1016/j.mejo.2006.05.011

[24] Liu, W., Zheng, W. and Jiang, Q. *First-principles study of the surface energy and work function of III-V semiconductor compounds.* Physical Review B, **75**(23):235322, 2007. ISSN 1098-0121. doi:10.1103/PhysRevB.75.235322

[25] Eckhardt, R. *Stan Ulam, John von Neumann, and the Monte Carlo Method.* Los Alamos Science, (Special Issue):131--143, 1987

[26] Schulze, T. P. and Smereka, P. *An energy localization principle and its application to fast kinetic Monte Carlo simulation of heteroepitaxial growth.* Journal of the Mechanics and Physics of Solids, **57**(3):521--538, 2009. ISSN 00225096. doi:10.1016/j.jmps.2008.11.007

[27] Schulze, T. P. and Smereka, P. *Kinetic Monte Carlo simulation of heteroepitaxial growth: Wetting layers, quantum dots, capping, and nanorings.* Physical Review B, **86**(23):235313, 2012. ISSN 1098-0121. doi: 10.1103/PhysRevB.86.235313

[28] Baskaran, A. *Modeling and Simulation of Heteroepitaxial Growth.* 2009

[29] Dalla Torre, J., Rouhani, M. D., Malek, R., Estève, D. and Landa, G. *Beyond the solid on solid model: An atomic dislocation formation mechanism.* Journal of Applied Physics, **84**(10):5487, 1998. ISSN 00218979. doi:10.1063/1.368312

[30] AdelsonVelskii, M. and Landis, E. *An algorithm for the organization of information.* 1963

[31] Grandjean, N. *Epitaxial growth of highly strained InxGa1-xAs on GaAs (001): the role of surface diffusion length.* Journal of crystal growth, **134**(May), 1993

[32] Orr, B. and Kessler, D. *A model for strain-induced roughening and coherent island growth.* EPL (Europhysics . . . , **19**(1), 1992

[33] Slawinski, M. *Waves and rays in elastic continua.* Second edition, 2007

[34] Mo, Y. and Lagally, M. *Anisotropy in surface migration of Si and Ge on Si (001).* Surface science, **248**(1991):313--320, 1991

[35] Ohta, K., Kojima, T. and Nakagawa, T. *ANISOTROPIC SURFACE MIGRATION OF Ga ATOMS ON GaAs (001).* **95**:71--74, 1989

[36] Itoh, M. *Kinetic Monte Carlo study of step asymmetry and stable step orientations on GaAs(001).* Physical Review B, **64**(4):1--5, 2001. ISSN 0163-1829. doi:10.1103/PhysRevB.64.045301

[37] Apostolopoulos, G., Boukos, N., Herfort, J., Travlos, a. and Ploog, K. *Surface morphology of low temperature grown GaAs on singular and vicinal substrates.* Materials Science and Engineering: B, **88**(2-3):205--208, 2002. ISSN 09215107. doi:10.1016/S0921-5107(01)00905-9

[38] Smilauer, P. and Vvedensky, D. *Erratum: Coarsening and slope evolution during unstable epitaxial growth.* Physical review. B, Condensed matter, **53**(19):13194, 1996. ISSN 0163-1829

[39] Clarke, S. and Vvedensky, D. *Origin of reflection high-energy electron-diffraction intensity oscillations during molecular-beam epitaxy: A computational modeling approach.* Physical review letters, **58**(21):2235--2238, 1987

[40] Shitara, T., Vvedensky, D. D., Wilby, M. R., Zhang, J., Neave, J. H. and Joyce, B. A. *Step-density variation and reflection high-energy electorn-diffraction intensity oscillations during epitaxial growth on vicinal GaAs(001).* Phyical Review B, **46**(11):6815--6824, 1992

[41] Neave, J. and Dobson, P. *Reflection high-energy electron diffraction oscillations from vicinal surfaces—a new approach to surface diffusion measurements.* Applied Physics ..., **100**(1985):1--4, 1985. doi:10.1063/1.96281

[42] Grosse, F. and Zimmermann, R. *Monte Carlo growth simulation for Al Ga As heteroepitaxy.* **212**:128--137, 2000

[43] Russo, G. and Smereka, P. *A multigrid-Fourier method for the computation of elastic fields with application to heteroepitaxy.* Multiscale Modeling & Simulation, **5**(1):130--148, 2006

[44] Wulff, G. *Zur Frage der Geschwindigkeit des Wachstums und der Auflösung der Krystallflächen.* Zeitschrift für Krystallographie und Mineralogie, **34**(5/6):449--530, 1901